

OKINAWA INSTITUTE OF SCIENCE AND TECHNOLOGY
GRADUATE UNIVERSITY

Thesis submitted for the degree

Doctor of Philosophy

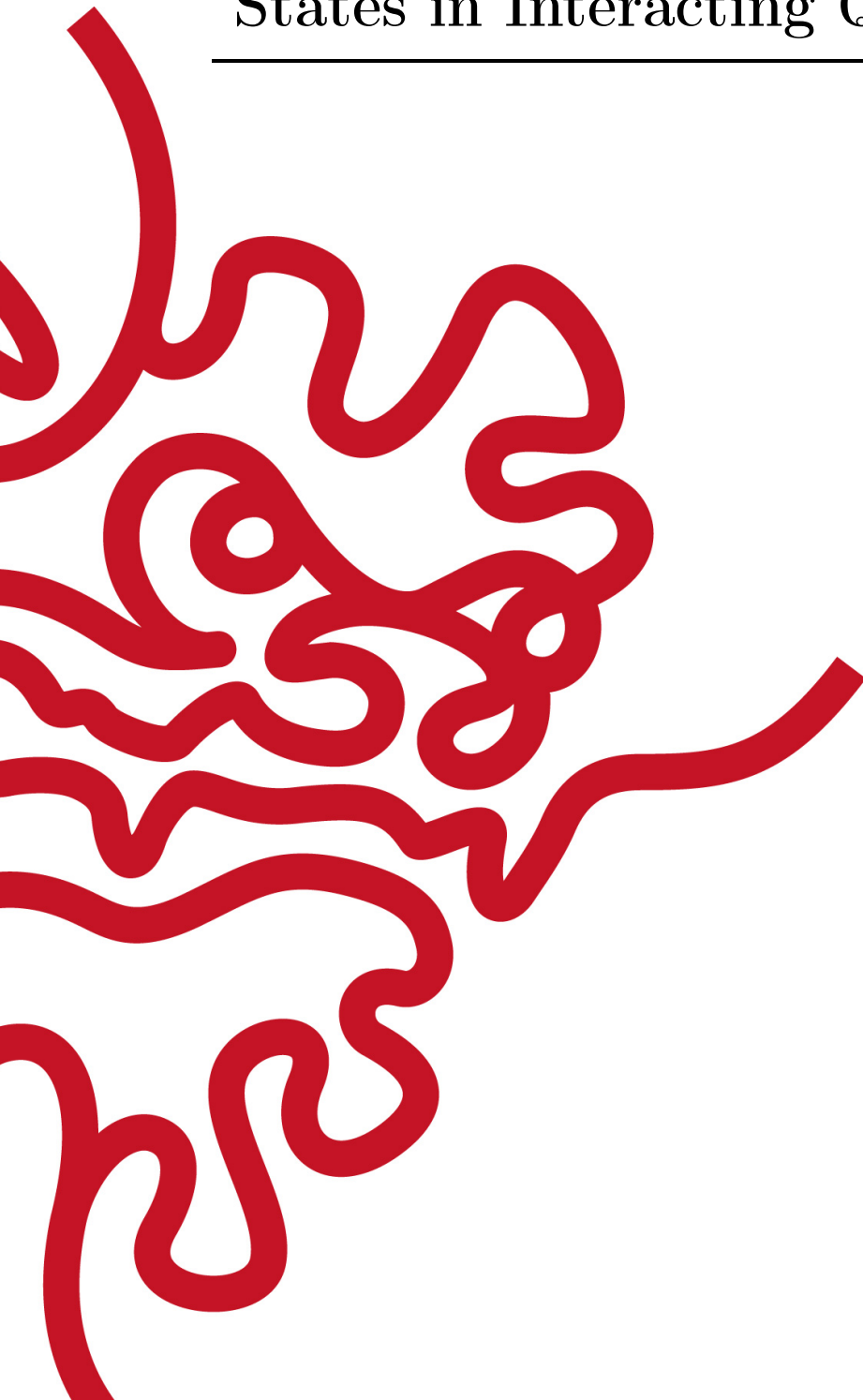
Controlling Superfluid and Insulating States in Interacting Quantum Gases

by

Tim Keller

Supervisor: **Thomas Busch**

August 2022



Declaration of Original and Sole Authorship

I, Tim Keller, declare that this thesis entitled *Controlling Superfluid and Insulating States in Interacting Quantum Gases* and the data presented in it are original and my own work.

I confirm that:

- No part of this work has previously been submitted for a degree at this or any other university.
- References to the work of others have been clearly acknowledged. Quotations from the work of others have been clearly indicated, and attributed to them.
- In cases where others have contributed to part of this work, such contribution has been clearly acknowledged and distinguished from my own work.
- None of this work has been previously published elsewhere, with the exception of the following:

- the results of Chapter 4 are published as:

Tim Keller, Thomás Fogarty, Jing Li, and Thomas Busch
Feshbach engine in the Thomas-Fermi regime
Phys. Rev. Research **2**, 033335 (2020).

I have derived all of the analytical results, performed all of the numerical simulations and wrote a first draft of the manuscript. All authors contributed to the discussion and interpretation of the results and to the writing of the final version.

- the results of Chapter 5 are published as:

Karol Gietka, Friederike Metz, **Tim Keller**, and Jing Li
Adiabatic critical quantum metrology cannot reach the Heisenberg limit even when shortcuts to adiabaticity are applied
Quantum **5**, 489 (2021).

The project idea as well as the central analytical and numerical results stem from Karol Gietka. I have mainly contributed the novel shortcut to adiabaticity for the case study with the quantum Rabi model under the Schrieffer-Wolff transformation and to the interpretation of the results in terms of Fig. 5 in the publication. All authors contributed to the discussion and interpretation of the results and to editing the final version of the paper.

– the results of Chapter 7 are published as:

Tim Keller, Thomás Fogarty, and Thomas Busch
*Self-Pinning Transition of a Tonks-Girardeau Gas
in a Bose-Einstein Condensate*
Phys. Rev. Lett. **128**, 053401 (2022).

I have derived all of the analytical results and performed all of the numerical simulations presented in the publication as well as in the supplemental material and wrote a first draft of the manuscript. All authors contributed to the interpretation of the results and to the writing of the final version.

- All of the above articles have been published in an open access format under the ‘Creative Commons Attribution 4.0 International’ license and I have permission to reprint them for the purpose of the thesis.

Date: August 18, 2022

Signature:

Tim Keller

Abstract

Controlling Superfluid and Insulating States in Interacting Quantum Gases

In this thesis, I present two studies on controlling the state and properties of both single-species and composite quantum gases by tuning the various interaction strengths. In the first work, I derive a shortcut to adiabaticity (STA) for tuning a Feshbach resonance in repulsively interacting Bose-Einstein condensates (BECs) in the Thomas-Fermi regime. This shortcut mimics an adiabatic evolution and allows one to compress and expand a BEC without friction within an almost arbitrarily short time interval. I then use this technique to show how it can boost the performance of the so-called Feshbach quantum engine and also determine its limits and the instabilities it can lead to. The first part is complemented by a study demonstrating the general ineffectiveness of STAs as a tool to increase the attainable precision in critical quantum metrology at the example of two critical toy models. In the second part, I show that a strongly correlated one-dimensional quantum gas in the Tonks-Girardeau (TG) limit that is immersed into a BEC can undergo a transition to a crystal-like insulator state without any externally imposed lattice potential. I develop a model that accurately describes the system in the pinned insulator state, even if the TG gas has a finite temperature. Additionally, I study the superfluid state that can persist in the gas for finite interactions away from the TG limit and uncover the full phase diagram of the system.

Acknowledgment

As scientists, we famously work standing on the shoulders of giants. Luckily, getting up there becomes a lot easier if you have a supervisor like Thomas Busch, who is not only physically tall, but also as supportive and caring as him. His kindness and his commitment to the well-being of each and every group member and providing them with opportunities for their professional growth cannot be stressed enough. Your advice and guidance, both scientific and personal, and your sixth sense for knowing where to dig for interesting physics were truly invaluable and made these five years an incredibly rewarding experience.

Words cannot express how grateful and indebted I am to Thomás Fogarty, a.k.a. Mossy. You introduced me to the world of ultracold atoms and started this whole journey. From telling me you ‘know this nice place in Japan’ one day in May 2014 to now, exactly eight years later, sitting here and writing this, it still feels unreal how much that simple moment has shaped my life over the past years. Thank you for teaching me the tools of the trade! Your humor, your enthusiasm for physics (and movies!) and our shared passion for Saarland cuisine made all those meetings, lunches and coffee breaks something to look forward to. They made the good times more enjoyable and the tough times bearable.

The same goes for all the past and present members of the Quantum Systems Unit that have truly made it a home away from home. Sawako, for all the administrative support and making sure that even during a pandemic travel goes smoothly. Chris, for being such a caring human being and an incredible friend all around (all the unsolicited compliments were also nice). Rike, for sharing an office with me for nearly five years (and letting me have the large desk!), for letting me take care of Moko and for countless Saturday mornings walking the dogs at Animal Garden with Sara, Sasha and Gear. Houshu, JC, Seyyare and Sarika for joining the self-pinning ‘cult’ and our Friday afternoon meetings. Angela and Jing, for all the amazing birthday cakes. And of course Albert, Ayaka, Hasan, Irina, James, Juan, Karol, Keerthy, Kritika, Leilee, Lewis, Mathias, Momo, Sahar and Tai for all the discussions, the fun trips, the advice and sharing your food.

I am also very grateful for the generous support from a Research Fellowship for Young Scientists by the Japan Society for the Promotion of Science under JSPS KAKENHI Grant No. 21J10521 and for the computing resources provided by the Scientific Computing and Data Analysis section at OIST, which made many of the results presented here possible in the first place. I would also like to thank Dr. Konrad Viebahn and the Lattice and Cavity Teams at ETH Zurich for the inspiring discussions and the kind hospitality during a visit to the group of Prof. Tilman Esslinger, and Prof.

Giovanna Morigi for numerous invitations over the years. It was always a pleasure to be back at Saarland university and what you and Simon Jäger taught me built the foundations that made life a lot easier during the PhD.

Furthermore, I am indebted to Prof. Joachim Brand for his helpful comments on my thesis proposal and the participants and organizers of ANZSUP 2019 for a wonderful summer school at the University of Otago in Dunedin, New Zealand. Similarly, to the organizers and participants of FINESS 2022 for a truly stimulating conference in St. Martin, Germany, particularly Elmar Haller, Romain Dubessy and Russel Bisset for their helpful comments and interest in my work.

Finally and most importantly, all the people helping me to stay connected to the ‘real world’. Especially Anni and Lars, for years of friendship back home and across borders and time zones. All your messages, care packages and visits meant a lot to me!

And above all, my family. My parents, Doris and Rolf, and my brother Mischa. For your love and support that paved the way to where I am today and for enduring my absence in times of need. From your example I have learned what can be achieved with true perseverance and diligence. And of course my partner ひかり, for her patience and understanding during busy times and for her love and encouragement that carried me through these past years. Thank you for living up to your name. Your shine brightens even the gloomiest of Okinawa’s rainy seasons.

Abbreviations

BEC	Bose-Einstein Condensate
BCS	Bardeen-Cooper-Schrieffer
BKT	Berezinskii-Kosterlitz-Thouless
CD	Counterdiabatic Driving
EOM	Equation Of Motion
FFLO	Fulde-Ferrell-Larkin-Ovchinnikov
FFT	Fast Fourier Transform
GPE	Gross-Pitaevskii Equation
GPU	Graphics Processing Unit
LCD	Local Counterdiabatic Driving
ODLRO	Off-Diagonal Long-Range Order
QFI	Quantum Fisher Information
QSL	Quantum Speed Limit
RSPDM	Reduced Single-Particle Density Matrix
SF	SuperFluid
SPGPE	Stochastic Projected Gross-Pitaevskii Equation
SQL	Standard Quantum Limit
STA	Shortcut To Adiabaticity
TF	Thomas-Fermi
TG	Tonks-Girardeau
TRA	Time-Rescaled Adiabatic reference
ZNG	Zaremba-Nikuni-Griffin

Nomenclature

\hbar	reduced Planck constant ($1.054\,571\,817 \times 10^{-34}$ Js)
k_{B}	Boltzmann constant ($1.380\,649 \times 10^{-23}$ JK $^{-1}$)
a_0	Bohr radius ($5.291\,772\,109 \times 10^{-11}$ m)
m_u	unified atomic mass unit ($1.660\,539\,066 \times 10^{-27}$ kg)

夜走らす舟や
子ぬ方星見当てい
我ん生ちえる親や
我んどう見当てい
—ていんさぐぬ花

Für meine Familie

Contents

Declaration of Original and Sole Authorship	iii
Abstract	v
Acknowledgment	vii
Abbreviations	ix
Nomenclature	xi
Contents	xv
List of Figures	xix
List of Tables	xxi
Introduction	1
I Fundamentals	5
1 Interacting Quantum Gases	7
1.1 Interactions between Cold Atoms	8
1.2 Feshbach Resonances	9
1.3 Bose-Einstein Condensation and Gross-Pitaevskii Equation	10
1.4 Thomas-Fermi Limit	13
1.5 Superfluid and Insulating States	14
1.5.1 The Landau Criterion for Superfluidity	16
1.5.2 Absence of Superfluidity: Insulating States	18
1.6 Lower-Dimensional Systems	19
2 Numerical Methods	25
2.1 Fourier Split-Step Method	25
2.2 Exact Diagonalization	29
2.3 Benchmarking: Analytically Solvable Models	30

II	Quantum Control, Shortcuts to Adiabaticity & Feshbach Engines	33
3	Shortcuts to Adiabaticity	35
3.1	Counterdiabatic Driving, Inverse Engineering and Quantum Speed Limits	36
3.2	Shortcuts in Interacting Many-Body Systems	39
3.3	Coherent Control of Bose-Einstein Condensates	43
3.3.1	Attractive Interactions: Bright Solitons	43
3.3.2	Repulsive Interactions: Thomas-Fermi Regime	46
4	Feshbach engine in the Thomas-Fermi regime (Publication [1])	51
4.1	Introduction	51
4.2	Quantum Thermodynamics and Feshbach Engines	53
4.3	Publication	57
4.4	Experimental Considerations	58
4.5	Conclusion & Outlook	59
4.5.1	Isochoric Strokes	59
4.5.2	Extracting Work from the Engine	60
5	Adiabatic critical quantum metrology cannot reach the Heisenberg limit even when shortcuts to adiabaticity are applied (Publication [2])	61
5.1	Introduction	61
5.2	Critical Quantum Metrology	62
5.3	Shortcuts for Critical Toy Models	63
5.3.1	Landau-Zener Model	63
5.3.2	Quantum Rabi Model	64
5.4	Publication	68
5.5	Conclusion & Outlook	68
III	Interacting Two-Component Systems in 1D	69
6	Background	71
6.1	Pinning Transition	71
6.2	Atomic Mixtures	73
7	Self-Pinning Transition of a Tonks- Girardeau Gas in a Bose-Einstein Condensate (Publication [3])	77
7.1	Introduction	77
7.2	Model	79
7.2.1	Self-Pinned State	80
7.2.2	Finite Temperature	81
7.3	Publication	84
7.4	Supplemental Material	84
7.5	Experimental Considerations	84
7.6	Conclusion & Outlook	87
7.6.1	Phonons	87

7.6.2	Symmetry Breaking & Supersolidity	87
7.6.3	Quantum Magnetism & FFLO Superconductor	88
8	Fermionization of a One-Dimensional Bose Gas Immersed into a BEC	91
8.1	Introduction	91
8.2	Model	92
8.3	Superfluid State	93
8.4	Phase Diagram	97
8.5	Conclusion & Outlook	100
	Conclusion	103
	Bibliography	105

List of Figures

1.1	Two-channel model for Feshbach resonances	10
1.2	Excitation spectra of a Bose-Einstein condensate and ^4He	16
1.3	Peierls instability in a linear chain of atoms	19
2.1	Eigenenergies and ground state density of two interacting particles in a 1D harmonic trap	31
3.1	Accompanying local counterdiabatic trapping frequency ramp for changing the interaction of two atoms in 1D	41
3.2	Evaluation of shortcut performance for ramping the interaction strength between two harmonically trapped particles in 1D	42
3.3	Interaction ramp shortcuts for a 1D bright soliton	45
3.4	Bright soliton energy as a function of their width in 1D, 2D and 3D	46
4.1	Classical Otto engine cycle in the pressure-volume plane	54
4.2	Schematic Feshbach engine cycles for a 1D bright soliton and a 3D Thomas-Fermi BEC working medium	56
5.1	Local counterdiabatic ramp for the coupling strength in the quantum Rabi model	66
6.1	Phase diagram of a 1D quantum gas in a lattice potential	73
7.1	Solutions of the self-consistency equation for the finite temperature self-pinning transition	83
7.2	Quantum magnetism with two-component self-pinning transition	89
8.1	Density of $N = 2$ and $N = 3$ particles immersed into a BEC as a function of intraspecies repulsion	94
8.2	Energy of $N = 2$ and $N = 3$ particles immersed into a BEC as a function of intraspecies repulsion	96
8.3	Coherence of $N = 2$ and $N = 3$ particles immersed into a BEC as a function of intraspecies repulsion	98
8.4	Phase diagram of $N = 2$ and $N = 3$ particles immersed into a BEC as a function of intraspecies repulsion and interspecies interaction	99

List of Tables

7.1	Experimental estimates for the self-pinning transition	85
-----	--	----

Introduction

In the last century, the first quantum revolution developed a theory that helped us understand the laws of physics on a microscopical scale and brought technologies like lasers or transistors that now govern our day-to-day life. Right now, we are in the middle of a second quantum revolution [4]. Where in the first quantum revolution we simply made use of the newly found quantum materials, the second quantum revolution is about actively controlling, engineering and designing quantum systems to our liking. While there is a general consensus which milestones need to be achieved in order to construct, for example, a universal quantum computer [5], which is often viewed as the primary goal for this second quantum revolution, they all pose great challenges to physicists both on the experimental and theoretical level.

One particular aspect of this is the precise control of interacting many-body or even macroscopic quantum systems, which often behave quite different from their individual constituents [6]. Control, the ability to not just scientifically explain your surroundings, but to actually engineer them to your liking, is the key factor that leads from the scientific understanding of a physical phenomenon to its use in technological applications [7]. In the case of quantum systems, obtaining this control is particularly hard since they need to be cooled down and isolated from their surroundings at all times in order to shield them from unwanted interactions.

In this thesis, I will present two studies of quantum systems, where in order to control their properties, we can use the intrinsic interaction of a many-body quantum system as well as the interaction with its environment to our advantage instead. The first study is situated in the field of quantum thermodynamics [8]. Technological advancements have allowed for continuous progress in the miniaturization of classical heat engines [9, 10] and yet the first successful operation of a heat engine using a quantum object as its working medium was only demonstrated in 2016 in the group of Ferdinand Schmidt-Kaler in Mainz [11] with their single-ion heat engine in a specifically designed Paul trap based on a theoretical proposal in 2012 [12]. This strikingly demonstrates the difficulties associated with achieving the necessary control for an intricate process like a quantum engine cycle and since then only a handful of other engines have been realized, e.g. using spin degrees of freedom [13, 14].

As opposed to technological improvements, in the first study I investigate how novel protocols, which in principle allow to reach a desired target state with perfect fidelity and in almost arbitrarily short times, are able to improve the operation of quantum heat engines. This is done at the example of a so-called Feshbach engine, which performs work by modulating the interaction strength of its superfluid Bose-Einstein condensate working medium. The protocols I use are shortcuts to adiabaticity

(STA) [15]. Similar to how optimal control methods can be used to find the fastest path for moving a quantum system from one point to another while minimizing losses and unwanted excitations, i.e. finding the ‘quantum brachistochrone’ [16], STA work by finding the path between an initial and a final state that mimics adiabatic evolution, i.e. avoids excitations altogether, for a given duration. Additionally, I show that there are other fields of quantum physics in which STA can be even detrimental in contrast, by demonstrating their ineffectiveness for increasing the attainable precision in critical quantum metrology.

The second study is an example of indirectly controlling a quantum system via its environment in the form of a quantum phase transition [17]. Phase transitions as a collective phenomenon of many individual constituents are one of the most interesting aspects of physics and the famous example of Bose-Einstein condensation [18, 19] is a central aspect of this thesis. Usually, phase transitions at finite temperature result from the competition between energy and entropy contributions to the free energy [20]. At zero temperature, the competition between two distinct energy contributions in the system can still lead to quantum phase transitions, driven purely by quantum fluctuations. In the field of ultracold atoms, one of the most prominent ones is the superfluid to Mott insulator transition for a Bose-Einstein condensate (BEC) trapped in an optical lattice potential [21]. If the system is dominated by the kinetic energy contribution, it remains in a spread out and phase-coherent superfluid state, while for stronger repulsive interactions, the energy is minimized by transitioning to a localized Mott insulator state with an integer number of atoms per lattice site and a gapped energy spectrum.

Such a behavior is reminiscent of metal to insulator transitions in solid state physics and this control over the fundamental character of the system, together with the high degree of tunability, their accessible length and time scales as well as their purity compared to condensed matter systems, is what makes neutral atoms in optical lattice potentials to ideal quantum simulators of such systems [22–25].

In the second study, I describe a novel superfluid-insulator transition in a one-dimensional, strongly repulsive quantum gas in the Tonks-Girardeau (TG) regime, in which the necessary periodic trapping potential is created by the TG gas itself via the backaction it exerts onto a homogeneous BEC into which it is immersed. I develop an effective model for accurately describing this self-pinned state even at finite temperatures and I also cover the case of finite repulsion in the immersed component, away from the Tonks-Girardeau limit, where a superfluid state can persist and an additional first-order phase transition is present. The non-rigid nature of the matter-wave trapping potential in the self-pinned state also enables phonon-like excitations, a crucial feature of condensed matter systems that has been lacking in quantum simulators until last year [26] and I provide an outlook to possible applications.

This thesis is structured into three parts, containing chapters built around the three peer-reviewed publications and the one preprint that have resulted from my work. The first part provides the necessary theories and methods used in this work. The second one focuses on quantum control, particularly on shortcuts to adiabaticity, both as a tool to boost the performance of Feshbach engines and in the context of critical quantum metrology. The third part describes the novel superfluid-insulator transition in a one-dimensional mixture of strongly correlated and weakly correlated systems mentioned above.

The following provides a brief overview over each part and its chapters:

- **Part I: Fundamentals**

- **Chapter 1** introduces the theory of cold atoms and interacting quantum gases that this thesis is based on. A particular focus is on the concept of superfluidity and its absence in insulating states as well as on lower-dimensional systems.
- **Chapter 2** introduces the numerical methods that have been used to obtain a majority of the results presented in this thesis, namely the Fourier split-step method and exact diagonalization, as well as ways to benchmark the numerical results.

- **Part II: Quantum Control, Shortcuts to Adiabaticity & Feshbach Engines**

- **Chapter 3** introduces the concept of shortcuts to adiabaticity and presents derivations for various shortcuts for interaction ramps in several quantum many-body systems.
- **Chapter 4** presents the context and possible extensions of Publication [1]

Tim Keller, Thomás Fogarty, Jing Li, and Thomas Busch
Feshbach engine in the Thomas-Fermi regime
 Physical Review Research **2**, 033335 (2020),

where a novel shortcut presented in the preceding chapter was used to boost the performance of a Feshbach quantum heat engine.

- **Chapter 5** presents the context and impact of Publication [2]

Karol Gietka, Friederike Metz, Tim Keller, and Jing Li
Adiabatic critical quantum metrology cannot reach the Heisenberg limit even when shortcuts to adiabaticity are applied
 Quantum **5**, 489 (2021),

where it was shown at the example of two toy models that counterintuitively shortcuts to adiabaticity are not able to improve the obtainable precision in critical quantum metrology.

- **Part III: Interacting Two-Component Systems in 1D**

- **Chapter 6** introduces the pinning or commensurate-incommensurate transition of a strongly-interacting, one-dimensional quantum gas in a lattice potential as well as important results from the study of atomic mixtures.
- **Chapter 7** presents the context and possible extensions of Publication [3]

Tim Keller, Thomás Fogarty, and Thomas Busch
Self-Pinning Transition of a Tonks-Girardeau Gas in a Bose-Einstein Condensate
 Physical Review Letters **128**, 053401 (2022) (Editor's Suggestion),

where a novel self-pinning transition of a strongly correlated gas in the Tonks-Girardeau limit immersed into a Bose-Einstein condensate was described and an effective model capturing the physics both at zero and at finite temperature was developed.

- **Chapter 8** presents a study of the self-pinning transition away from the Tonks-Girardeau limit, where a superfluid state of the immersed component can persist at finite intraspecies repulsion. The effective model is extended to include this superfluid state and the phase diagram is calculated in the numerically tractable case of two and three immersed atoms.

Part I
Fundamentals

Chapter 1

Interacting Quantum Gases

In order to study the quantum behavior of matter, the thermal de Broglie wavelength λ_T [27] of a particle needs to be comparable to a characteristic length scale, like the average interparticle spacing of its constituents

$$\lambda_T = \sqrt{\frac{2\pi\hbar^2}{mk_B T}} \gtrsim n^{-1/3}.$$

Here n is the density of the system, m the mass of the particle, k_B the Boltzmann constant and T the system temperature. Dilute clouds of neutral alkali atoms are often the system of choice when trying to reach these regimes where quantum effects become relevant [28]. They possess a single valence electron in their outermost electronic shell and the resulting optical transitions in combination with their magnetic moments make them suitable for manipulation with electromagnetic fields. These fields allow for great flexibility to engineer and tune the geometry, dimensionality and even the interaction strength between particles [29] in the system. Fundamentally, such interacting quantum gases comprised of N atoms are described by a wave function $\psi(\mathbf{r}, t) = \psi(\mathbf{r}_1, \mathbf{r}_2, \dots, \mathbf{r}_N, t)$ obeying the Schrödinger equation

$$i\hbar \frac{\partial \psi(\mathbf{r}, t)}{\partial t} = \hat{H} \psi(\mathbf{r}, t) = \left[\sum_{i=1}^N \left(-\frac{\hbar^2}{2m} \nabla_{\mathbf{r}_i}^2 + V(\mathbf{r}_i) \right) + \sum_{i < j} V_{\text{int}}(\mathbf{r}_i, \mathbf{r}_j) \right] \psi(\mathbf{r}, t),$$

where the Hamiltonian \hat{H} , besides the kinetic energy term, contains potential terms $V(\mathbf{r}_i)$ for each particle as well as the interaction potential $V_{\text{int}}(\mathbf{r}_i, \mathbf{r}_j)$ [30].

This chapter introduces the theory of cold atoms and interacting quantum gases that my thesis is based on. A particular focus is on tuning interaction strengths via Feshbach resonances, the phenomenon of Bose-Einstein condensation and its treatment in a mean-field description, the concept of superfluidity and its absence in insulating states as well as lower-dimensional systems.

1.1 Interactions between Cold Atoms

Neutral atoms can interact with each other via scattering processes if their spatial separation becomes comparable to their size. A good measure for their size is given by the thermal de Broglie wavelength λ_T mentioned earlier [27].

In order to describe the interaction between two cold atoms, we will focus on radially symmetric interactions, depending solely on their relative distance $r = |\mathbf{r}_1 - \mathbf{r}_2|$. Making use of the spherical harmonics to describe the angular dependence, the Schrödinger equation for the remaining radial part $R_l(r)$ of the wave function can be rewritten as

$$\left[-\frac{\hbar^2}{2m_r} \left(\frac{\partial^2}{\partial r^2} + \frac{2}{r} \frac{\partial}{\partial r} \right) + V_{\text{eff}}(r) \right] R_l(r) = ER_l(r), \quad (1.1)$$

where m_r is the reduced mass pertinent to the relative motion of the atoms and E is the energy [30]. The effective potential contains both the actual interaction potential $V_{\text{int}}(r)$ as well as the rotational energy for a certain angular momentum quantum number l ,

$$V_{\text{eff}}(r) = l(l+1) \frac{\hbar^2}{2m_r r^2} + V_{\text{int}}(r). \quad (1.2)$$

A good model for the actual interaction potential between neutral atoms is given by the Lennard-Jones potential [31], which describes the repulsive force due to the hard core potential at short distances as a term $\sim r^{-12}$ and the attraction at long ranges due to the van-der-Waals force by a term $\sim r^{-6}$

$$V_{\text{int}}(r) = \frac{A}{r^{12}} - \frac{B}{r^6}, \quad (1.3)$$

where A and B are constants. At large distances r , these terms are dominated by the r^{-2} dependence in the rotational energy term. Accordingly, for scattering processes with $l \neq 0$ at some energy $E = \hbar^2 k^2 / 2m_r$, the atoms will never ‘see’ the interaction potential, as the classical turning point $r_{\text{cl}} = \sqrt{l(l+1)}/k$ for their motion as they encounter this centrifugal barrier lies far beyond the interaction range. Therefore, it is sufficient to focus on the $l = 0$ case to study the interaction between cold neutral atoms, the so-called s-wave scattering [30].

Since we are dealing with elastic collisions that leave the wavenumber k unchanged, the interaction can only affect the phase of the wave function. This collisional phase shift η_0 generally depends on the exact form of the interaction potential, but using model potentials to represent certain aspects of the interaction, we can obtain expressions for these cases [31].

Focusing, for example, on the repulsive part of the Lennard-Jones potential and modeling it as a hard sphere potential with a diameter a , the phase shift is given by $\eta_0 = -ka$ for the incoming particle with wavenumber k . Modeling the attractive part as a potential well with depth V_0 and width r_0 , we obtain an effective hard sphere diameter $a(k) = -\eta_0(k)/k$ which gives rise to a scattering length a_s in the long-wavelength limit $k \rightarrow 0$

$$a_s \equiv \lim_{k \rightarrow 0} a(k) = -\lim_{k \rightarrow 0} \frac{\eta_0(k)}{k} = r_0 \left(1 - \frac{\tan(\kappa_0 r_0)}{\kappa_0 r_0} \right), \quad (1.4)$$

where $\kappa_0^2 = -2m_r V_0/\hbar^2$. More generally, in the long-wavelength limit $k \rightarrow 0$ in which the scattered particle is not able to resolve the exact form of the scattering potential, the scattering length for an arbitrary short-range potential is given by

$$\frac{1}{a_s} = -\lim_{k \rightarrow 0} k \cot(\eta_0(k)) , \quad (1.5)$$

recovering the hard-sphere result $\eta_0 = -a_s k$ in the absence of any resonance or open scattering channel that might modify the phase shift. Since it cannot resolve the exact scattering potential, the scattered particle cannot distinguish between an arbitrary short-range potential and a hard sphere. This behavior is reminiscent of electrostatics, where both a spherically symmetric charge distribution and a point charge with corresponding properties generate the same far field [32]. Thus, we can represent the interaction of cold atoms in the s-wave regime with a so-called pseudo potential in the form of a point interaction that will produce the desired phase shift for a given scattering length [33]. In the case of two identical atoms with mass m scattering off each other, one obtains

$$V_{\text{int}}(\mathbf{r}_1, \mathbf{r}_2) = \frac{4\pi\hbar^2 a_s}{m} \delta(\mathbf{r}_1 - \mathbf{r}_2) \frac{\partial}{\partial r}(r \cdot) \equiv g \delta(\mathbf{r}_1 - \mathbf{r}_2) \frac{\partial}{\partial r}(r \cdot) , \quad (1.6)$$

with the interaction strength g only depending on the scattering length a_s . The derivative term is needed to regularize any singularities that might appear in the wave function as $r \rightarrow 0$.

1.2 Feshbach Resonances

We have seen how the interaction between cold atoms can be expressed as a simple contact potential whose strength depends on the scattering length for two-particle collisions. The great advantage and versatility of cold atom systems becomes apparent when recognizing that Feshbach resonances [34] allow one to tune the scattering length almost arbitrarily, making it possible to realize practically any attractive or repulsive interaction strength, as first demonstrated experimentally in 1998 [35, 36]. Taking into account that alkali metals like rubidium have a single valence electron with an additional spin- $\frac{1}{2}$ degree of freedom leads to a different interaction potential and therefore a different scattering length depending on if both electron spins of the identical atoms scattering off each other form a singlet state with total spin $S = 0$ or a triplet state with $S = 1$. The degeneracy of the triplet state with respect to the magnetic quantum number $m_S = \{-1, 0, 1\}$ can be lifted by applying an external magnetic field, which will change the energy of the state depending on m_S .

A Feshbach resonance occurs if the energy E of two atoms colliding in the respective magnetic substate is brought close to a bound state at energy E_c in the interaction potential of the singlet state, resulting in a diverging scattering length. This is also known as a magnetically induced Feshbach resonance. The general principle for such Feshbach resonances involving an open channel with some background scattering potential V_{bg} and a closed channel with some scattering potential V_c and a bound state

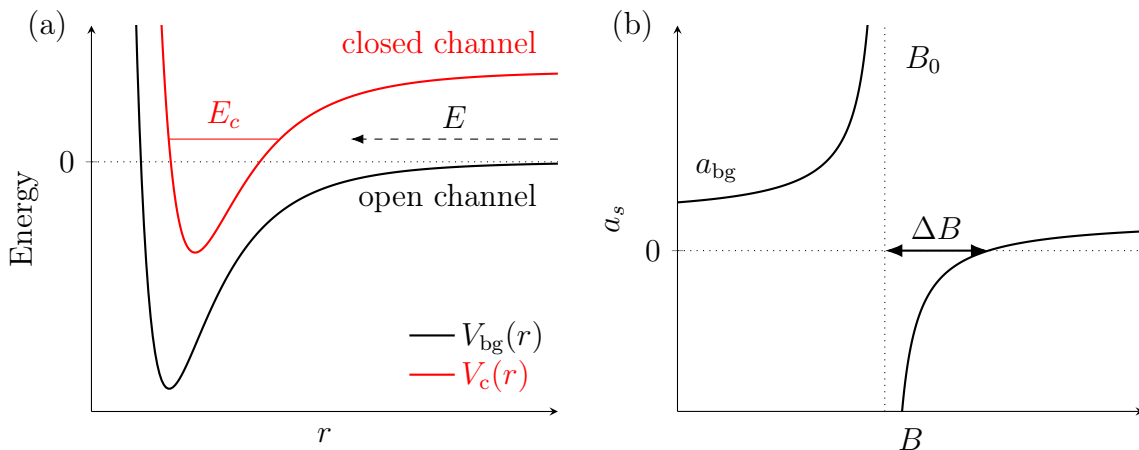


Figure 1.1: (a) A Feshbach resonance occurs when two atoms scattering with energy E in the background potential $V_{\text{bg}}(r)$, the so-called open channel, resonantly couple to a bound state at energy E_c in the so-called closed channel $V_c(r)$. (b) The resulting s -wave scattering length a_s , according to Eq. (1.7), for a magnetic Feshbach resonance where the open and closed channels are given by different internal spin states whose energy can be tuned by an external magnetic field via the Zeeman effect.

at E_c is demonstrated in Fig. 1.1 (a). The channel is called closed since its asymptotic energy at large atomic separation r lies above the incident energy E and it is therefore only accessible during the resonant coupling throughout the scattering process.

The dependence of the scattering length on the magnetic field B can be written as

$$a_s(B) = a_{\text{bg}} \left(1 - \frac{\Delta}{B - B_0} \right), \quad (1.7)$$

highlighting the Feshbach resonance around a field strength of B_0 , where a_{bg} is the scattering length of the background potential outside the resonance and Δ is the resonance width [37]. The resonance is plotted in Fig. 1.1 (b). In the case of a quasi-one-dimensional system, in which dynamics in two directions are essentially frozen out, e.g. via a tight confinement by a trapping potential in these directions, the effective one-dimensional interaction strength can be changed both via Feshbach resonances and by changing the frequency of the trapping potential [38], see also Section 1.6.

1.3 Bose-Einstein Condensation and Gross-Pitaevskii Equation

Let us consider a non-interacting ideal Bose gas at low temperatures. In the grand canonical ensemble the partition function of the system is simply given by [39]

$$Z = \prod_i \sum_{n_i=0}^{\infty} e^{\beta(\mu - \epsilon_i)n_i} = \prod_i \frac{1}{1 - e^{\beta(\mu - \epsilon_i)}}, \quad (1.8)$$

where $\beta = 1/k_B T$, μ is the chemical potential, ϵ_i are the single particle eigenenergies, depending on the environment, and n_i are the corresponding occupation numbers for each state. Calculating the grand canonical potential gives

$$\Omega = -k_B T \ln(Z) = k_B T \sum_i \ln(1 - e^{\beta(\mu - \epsilon_i)}) , \quad (1.9)$$

from which one can obtain the total number of particles as

$$\langle N \rangle = -\frac{\partial \Omega}{\partial \mu} = \sum_i \frac{1}{e^{\beta(\epsilon_i - \mu)} - 1} = \sum_i \bar{n}_i . \quad (1.10)$$

This yields the average occupation numbers \bar{n}_i for each single particle state, according to the Bose-Einstein statistics. Since the occupation numbers need to be positive, this creates the constraint $\mu < \epsilon_0$ for the chemical potential, assuming the eigenenergies fulfill $\epsilon_0 \leq \epsilon_i$. As $\mu \rightarrow \epsilon_0$, the ground state occupation diverges, revealing the mechanism behind Bose-Einstein condensation [27]. If we split the total number of atoms into a condensed part $N_0 \equiv \bar{n}_0$ and a thermal component N_T

$$\langle N \rangle = N_0 + N_T = N_0 + \sum_{i \neq 0} \bar{n}_i , \quad (1.11)$$

then as $\mu \rightarrow \epsilon_0$ or as the temperature is lowered below some critical value T_c , Bose-Einstein condensation manifests itself as a macroscopic occupation of the ground state $N_0 = \langle N \rangle - N_T$. Let us assume the environment is given by a square box of length L with volume $V = L^3$ and periodic boundary conditions, then the eigenenergies are of the form $\epsilon = \mathbf{p}^2/2m$, where the momentum \mathbf{p} is quantized according to $\mathbf{p} = 2\pi\hbar(n_x, n_y, n_z)/L$ with integer $n_{x,y,z}$. We make the replacement $\sum_{\mathbf{p} \neq 0} \rightarrow \frac{V}{(2\pi\hbar)^3} \int d\mathbf{p}$, obtaining

$$N_T = \frac{V}{\lambda_T^3} g_{3/2}(e^{\beta\mu}) , \quad (1.12)$$

where λ_T is again the thermal de Broglie-wavelength and

$$g_{3/2}(z) = \frac{2}{\sqrt{\pi}} \int_0^\infty dx \frac{x^{1/2}}{z^{-1}e^x - 1} . \quad (1.13)$$

The lowest eigenenergy is $\epsilon_0 = 0$, therefore condensation will occur for $\mu \rightarrow 0$ and we can calculate an expression for the critical temperature T_c from the previous equation (1.12), giving

$$k_B T_c = \frac{2\pi\hbar^2}{m} \left(\frac{n}{g_{3/2}(1)} \right)^{2/3} , \quad (1.14)$$

where $n = N/V$ and $g_{3/2}(1) \approx 2.61$. So for non-interacting particles with fixed mass m in a box, Bose-Einstein condensation can be reached by lowering the system temperature below a critical value T_c for fixed density n , or equivalently by increasing its density beyond some critical value n_c for a fixed temperature T .

As we have seen, even for an ideal, non-interacting gas of ultracold atoms Bose-Einstein condensation occurs. In general, the situation is more complicated considering external trapping potentials $V(\mathbf{r})$ in experimental realizations as well as usually weak interactions between the atoms in the dilute quantum gas. The latter are needed for the gas to thermalize, allowing it to be cooled down.

These effects can be taken into account in second quantization, where the many-body Hamiltonian of an interacting quantum gas, using bosonic field operators $\hat{\Psi}(\mathbf{r})$, reads

$$\hat{H} = \int d\mathbf{r} \hat{\Psi}^\dagger(\mathbf{r}) \left[-\frac{\hbar^2}{2m} \nabla^2 + V(\mathbf{r}) \right] \hat{\Psi}(\mathbf{r}) + \frac{1}{2} \int d\mathbf{r} d\mathbf{r}' \hat{\Psi}^\dagger(\mathbf{r}) \hat{\Psi}^\dagger(\mathbf{r}') V_{\text{int}}(\mathbf{r}, \mathbf{r}') \hat{\Psi}(\mathbf{r}') \hat{\Psi}(\mathbf{r}), \quad (1.15)$$

where the first integral contains the single particle Hamiltonian, while the second term describes the interaction between atoms [40]. We assume a dilute gas of cold atoms, allowing us to use the contact potential $V_{\text{int}}(\mathbf{r}, \mathbf{r}') = g\delta(\mathbf{r} - \mathbf{r}')$ derived in the previous section, where $g = 4\pi\hbar^2 a_s/m$, and yielding

$$\hat{H} = \int d\mathbf{r} \hat{\Psi}^\dagger(\mathbf{r}) \left[-\frac{\hbar^2}{2m} \nabla^2 + V(\mathbf{r}) + \frac{g}{2} \hat{\Psi}^\dagger(\mathbf{r}) \hat{\Psi}(\mathbf{r}) \right] \hat{\Psi}(\mathbf{r}). \quad (1.16)$$

In the fully condensed state, all atoms have the same single-particle wave function. Therefore, it is convenient to treat the system with a mean-field approach

$$\hat{\Psi}(\mathbf{r}) = \langle \hat{\Psi}(\mathbf{r}) \rangle + \delta\hat{\Psi}(\mathbf{r}), \quad (1.17)$$

separating the field operator into its mean-field value $\psi(\mathbf{r}) \equiv \langle \hat{\Psi}(\mathbf{r}) \rangle$ and fluctuations $\delta\hat{\Psi}(\mathbf{r})$ around this value, scaling as $1/N$ with the number of condensed particles N . If we restrict our treatment to almost fully condensed systems with large N , we can neglect these fluctuations and the system evolves in time according to

$$i\hbar \frac{\partial \hat{\Psi}(\mathbf{r})}{\partial t} = \left[\hat{\Psi}(\mathbf{r}), \hat{H} \right]. \quad (1.18)$$

Plugging ansatz (1.17) into Eqs. (1.16) and (1.18), using the commutation relations

$$\begin{aligned} \left[\hat{\Psi}(\mathbf{r}), \hat{\Psi}^\dagger(\mathbf{r}') \right] &= \delta(\mathbf{r} - \mathbf{r}') \\ \left[\hat{\Psi}(\mathbf{r}), \hat{\Psi}(\mathbf{r}') \right] &= \left[\hat{\Psi}^\dagger(\mathbf{r}), \hat{\Psi}^\dagger(\mathbf{r}') \right] = 0 \end{aligned} \quad (1.19)$$

for the bosonic field operators and neglecting all terms proportional to $\delta\hat{\Psi}(\mathbf{r})$, we obtain a mean-field equation for the BEC wave function ψ , called the Gross-Pitaevskii equation (GPE) after Eugene Gross and Lev Pitaevskii who both derived it independently in 1961 [41, 42]

$$i\hbar \frac{\partial \psi(\mathbf{r}, t)}{\partial t} = \left(-\frac{\hbar^2}{2m} \nabla^2 + V(\mathbf{r}) + g|\psi(\mathbf{r}, t)|^2 \right) \psi(\mathbf{r}, t). \quad (1.20)$$

It is also called the nonlinear Schrödinger equation since in the limit $g \rightarrow 0$, where the nonlinear interaction proportional to the density $n(\mathbf{r}) = \langle \hat{\Psi}^\dagger(\mathbf{r}) \hat{\Psi}(\mathbf{r}) \rangle = |\psi(\mathbf{r})|^2$ vanishes, the linear Schrödinger equation is recovered. The normalization of the condensate wave function is determined by the density as well, giving the number of atoms in the condensate as

$$\int d\mathbf{r} n(\mathbf{r}) = \int d\mathbf{r} |\psi(\mathbf{r})|^2 = N. \quad (1.21)$$

Another important effect of finite interactions is the lowering of the critical temperature for condensation compared to the ideal gas case in Eq. (1.14), see e.g. Ref. [43] for an in-depth discussion.

1.4 Thomas-Fermi Limit

One of the most relevant regimes for the study of Bose-Einstein condensates, both experimentally and theoretically, is the limit of large system sizes and repulsive interactions $Na_s/x_0 \gg 1$, where the repulsion leads to an expansion of the atomic cloud and $x_0 = \sqrt{\hbar/m\omega}$ is the length scale associated with the typically harmonic trapping of the cloud at a frequency of ω . The ratio of kinetic energy per particle to interaction energy per particle in such a cloud is on the order of $\sim N^{-4/5}$ [44] and therefore becomes insignificant for large particle numbers.

Neglecting the kinetic energy term in the Gross-Pitaevskii equation (1.20) and assuming a time-dependence $\psi(\mathbf{r}, t) = \psi(\mathbf{r})e^{-i\mu t/\hbar}$ with the chemical potential μ leads to

$$\mu\psi(\mathbf{r}) = (V(\mathbf{r}) + g|\psi(\mathbf{r})|^2)\psi(\mathbf{r}), \quad (1.22)$$

from which we can immediately solve for the density to obtain the Thomas-Fermi approximation

$$\psi_{\text{TF}}(\mathbf{r}, t) = \begin{cases} \sqrt{\frac{1}{g}(\mu - V(\mathbf{r}))}e^{-i\mu t/\hbar} & \text{for } \mu \geq V(\mathbf{r}) \\ 0 & \text{otherwise} \end{cases}. \quad (1.23)$$

The BEC density mirrors its trapping potential up to the point $\mu = V(\mathbf{r})$. Assuming for example an isotropic harmonic oscillator potential $V(\mathbf{r}) = \frac{1}{2}m\omega^2\mathbf{r}^2$ leads to a cloud radius of $R_{\text{TF}} = 2\mu/m\omega^2$ in each direction. The chemical potential is determined in terms of particle number and interaction strength from the normalization condition

$$N \stackrel{!}{=} \int d\mathbf{r} |\psi_{\text{TF}}(\mathbf{r})|^2, \quad (1.24)$$

which leads to

$$\mu_{\text{TF}} = \left(\frac{15Ng(m\omega^2)^{\frac{3}{2}}}{16\pi\sqrt{2}} \right)^{\frac{2}{5}} = \frac{\hbar\omega}{2} \left(15N \frac{a_s}{x_0} \right)^{2/5}. \quad (1.25)$$

Calculating the total system energy in the Thomas-Fermi approximation yields

$$E_{\text{TF}} = \int d\mathbf{r} \left(\frac{1}{2} m \omega^2 \mathbf{r}^2 |\psi(\mathbf{r})|^2 + \frac{g}{2} |\psi(\mathbf{r})|^4 \right) = \frac{5}{7} N \mu_{\text{TF}} . \quad (1.26)$$

The Thomas-Fermi approximation provides excellent agreement with experimentally and numerically observed condensate densities in many cases. The most notable difference occurs at the condensate edges, where ψ_{TF} exhibits an unphysical kink with diverging spatial derivative at the point of vanishing density, but it is possible to calculate better approximations to the smooth vanishing of the physical wave function [45]. Experimentally, the definition of the Thomas-Fermi radius $R_{\text{TF}} = 2\mu_{\text{TF}}/m\omega^2$ provides a convenient way to obtain accurate estimates for the number of condensed particles via Eq. (1.25) for an atomic cloud with a certain radius observed e.g. via absorption imaging.

1.5 Superfluid and Insulating States

In order to discuss superfluidity in the context of ultracold atomic gases, it is advantageous to switch to a hydrodynamic description for the BEC wave function $\psi(\mathbf{r}, t) = \sqrt{\rho(\mathbf{r}, t)} e^{i\phi(\mathbf{r}, t)}$ in terms of its real-valued amplitude $|\psi(\mathbf{r}, t)| = \sqrt{\rho(\mathbf{r}, t)}$ and phase $\phi(\mathbf{r}, t)$. Starting from the Gross-Pitaevskii equation (1.20), multiplying it with $\psi^*(\mathbf{r}, t)$ and then subtracting the complex conjugate of the resulting expression from the original equation leads to the continuity equation

$$\frac{\partial \rho(\mathbf{r}, t)}{\partial t} + \nabla \cdot \mathbf{j}(\mathbf{r}, t) \equiv 0 \quad (1.27)$$

for the density $\rho(\mathbf{r}, t) = |\psi(\mathbf{r}, t)|^2$ and where the probability current is defined as

$$\mathbf{j}(\mathbf{r}, t) = -\frac{i\hbar}{2m} (\psi^*(\mathbf{r}, t) \nabla \psi(\mathbf{r}, t) - \psi(\mathbf{r}, t) \nabla \psi^*(\mathbf{r}, t)) . \quad (1.28)$$

From this quantity we can also obtain the velocity field via

$$\mathbf{v}(\mathbf{r}, t) = \frac{\mathbf{j}(\mathbf{r}, t)}{\rho(\mathbf{r}, t)} = \frac{\hbar}{m} \nabla \phi(\mathbf{r}, t) . \quad (1.29)$$

This simple expression shows that the velocity only depends on the phase gradient of the wave function and also that the flow of the condensate must be irrotational since

$$\nabla \times \mathbf{v} = \frac{\hbar}{m} \nabla \times \nabla \phi(\mathbf{r}, t) \equiv 0 . \quad (1.30)$$

This only holds if the phase is ‘well-behaved’ however, since there are condensates exhibiting rotational flow caused by vortices that are characterized by singularities in the phase $\phi(\mathbf{r}, t)$ and corresponding vanishing densities $\rho(\mathbf{r}, t)$. The study of vortices in BEC is a large field in itself with topics ranging from triangular Abrikosov vortex lattices in highly rotating condensates [46] to the spontaneous formation of vortices during Bose-Einstein condensation as a result of the Kibble-Zurek mechanism [47].

One obtains an equivalent to the continuity equation (1.27) for the phase respectively the velocity from taking the imaginary part of the Gross-Pitaevskii equation (1.20) in terms of the new quantities and then calculating the gradient according to

$$m \frac{\partial \mathbf{v}(\mathbf{r}, t)}{\partial t} = -\nabla \left(-\frac{\hbar^2}{2m\sqrt{\rho(\mathbf{r}, t)}} \nabla^2 \sqrt{\rho(\mathbf{r}, t)} + \frac{1}{2}m|\mathbf{v}(\mathbf{r}, t)|^2 + V(\mathbf{r}) + g\rho(\mathbf{r}, t) \right). \quad (1.31)$$

The first term inside the parentheses is often referred to as ‘quantum pressure’ [27]. We want to describe the elementary excitations in the condensate in this description and consider a density $\rho = \rho_0 + \delta\rho$ with a homogeneous background ρ_0 and some small fluctuations $\delta\rho(\mathbf{r}, t)$ in a constant potential $V(\mathbf{r}) \equiv \text{const.}$. After linearizing Eqs. (1.27) and (1.31), i.e. discarding terms of order larger equal two in both $\delta\rho$ and \mathbf{v} , which is also assumed to be small, we combine them into a single equation of motion

$$m \frac{\partial^2 \delta\rho(\mathbf{r}, t)}{\partial t^2} = \nabla \cdot \left[\rho_0 \nabla \left(-\frac{\hbar^2}{4m\rho_0} \nabla^2 \delta\rho(\mathbf{r}, t) + g\delta\rho(\mathbf{r}, t) \right) \right]. \quad (1.32)$$

Assuming that the solution has a form of a travelling wave $\delta\rho(\mathbf{r}, t) \sim \exp[i(\mathbf{q} \cdot \mathbf{r} - \omega t)]$ with wave vector \mathbf{q} and frequency ω yields

$$m\omega^2 \delta\rho(\mathbf{r}, t) = \left(\frac{\hbar^2 \mathbf{q}^4}{4m} + g\rho_0 \mathbf{q}^2 \right) \delta\rho(\mathbf{r}, t), \quad (1.33)$$

from which we obtain the dispersion relation for the elementary excitations according to

$$\epsilon(\mathbf{q}) = \hbar\omega = \sqrt{\frac{\hbar^2 \mathbf{q}^2}{2m} \left(\frac{\hbar^2 \mathbf{q}^2}{2m} + 2g\rho_0 \right)}. \quad (1.34)$$

Interestingly, this result in the hydrodynamic description is identical to the spectrum first obtained by Bogoliubov from a microscopic theory for the Bose-Einstein condensate [48]. For small quasi-momenta, the spectrum is approximately linear and proportional to the speed of sound $c_s = \sqrt{g\rho_0/m}$, while for larger momenta the free-particle spectrum with an additional mean-field shift from the interactions is obtained according to

$$\epsilon(\mathbf{q}) \approx \begin{cases} \sqrt{\frac{\hbar^2 g\rho_0}{m}} q = c_s \hbar q & \text{for } q \ll 1/\xi \\ \frac{\hbar^2 q^2}{2m} + g\rho_0 & \text{for } q \gg 1/\xi \end{cases} \quad (1.35)$$

with $q = |\mathbf{q}|$. The change in asymptotic behavior occurs around $q \sim 1/\xi$, where $\xi = \sqrt{\hbar/2mg\rho_0}$ is the healing length. The spectrum is plotted in Fig. 1.2 (a).

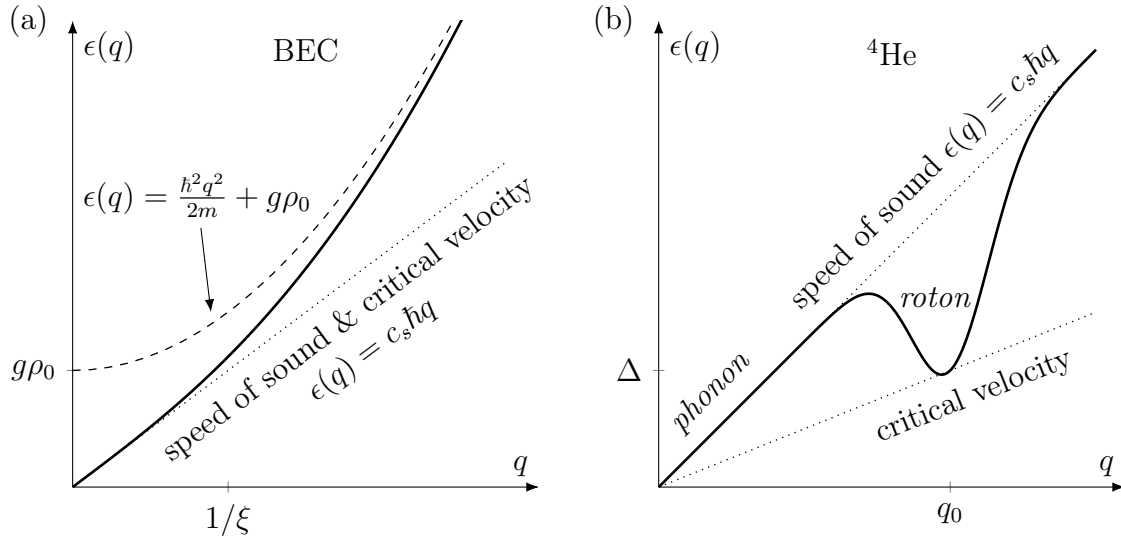


Figure 1.2: (a) Bogoliubov excitation spectrum (solid line) of a BEC according to Eq. (1.34) together with its asymptotic phonon-like (dotted line, valid for small q) and free particle-like (dashed line, valid for large q) approximations according to Eq. (1.35). The behavior changes once the quasi-momentum q becomes larger than the inverse healing length ξ . The speed of sound $c_s = \sqrt{g\rho_0/m}$ and the critical velocity for superfluidity according to the Landau criterion (1.38) are identical. (b) Schematic excitation spectrum for ${}^4\text{He}$. Due to the roton minimum at some quasi-momentum q_0 leading to excitations with decreased energy Δ compared to the phonon-like branch, the critical velocity for superfluidity is smaller than the speed of sound.

1.5.1 The Landau Criterion for Superfluidity

Consider a fluid of total mass M in its ground state with energy $E = E_0$ in a reference frame in which the fluid is at rest, i.e. in which its momentum vanishes such that $\mathbf{p} = 0$. If an obstacle is moved through the fluid at a relative velocity \mathbf{v} , then a Galilean transform $\mathbf{p}' = \mathbf{p} - M\mathbf{v}$ and $E' = E_0 + \mathbf{p}'^2/2M$ yields

$$E' = E_0 + \frac{1}{2}M|\mathbf{v}|^2 \quad (1.36)$$

for the energy of the fluid in the reference frame moving with the obstacle. If now a single excitation with momentum \mathbf{p} and energy $\epsilon(\mathbf{p})$ is present, then the energy in the moving reference frame reads

$$E' = E_0 + \epsilon(\mathbf{p}) - \mathbf{p} \cdot \mathbf{v} + \frac{1}{2}M|\mathbf{v}|^2. \quad (1.37)$$

From the perspective of the obstacle it is therefore energetically favorable to create an excitation in the fluid once the change in energy $\Delta E = \epsilon(\mathbf{p}) - \mathbf{p} \cdot \mathbf{v} < 0$ becomes negative. Therefore, there exists a critical velocity

$$v_{\text{crit}} = \min_{\mathbf{p}} = \frac{\epsilon(\mathbf{p})}{|\mathbf{p}|} \quad (1.38)$$

beyond which the system can lower its energy by creating excitations, corresponding to the dissipation of kinetic energy due to friction in a classical fluid, and thereby destroying superfluid or frictionless behavior. Exactly at the critical velocity the quasi-particle momentum \mathbf{p} is parallel to the velocity \mathbf{v} of the perturbation, but for higher velocities they may have a finite angle between them as long as $\Delta E < 0$ is fulfilled. Eq. (1.38) is commonly known as the Landau criterion [27].

From the Landau criterion one can directly see that the ideal, non-interacting Bose gas with $\epsilon(\mathbf{p}) = \mathbf{p}^2/2m$ is not superfluid since $v_{\text{crit}} = 0$ and therefore any finite-velocity flow will immediately create excitations in the fluid, while a Bose-Einstein condensate with dispersion relation (1.34) is superfluid with a critical velocity identical to the speed of sound $v_{\text{crit}} = c_s$. Atomic interactions and the resulting linear dispersion for long wavelengths therefore seem to play a crucial role for the existence of superfluidity. In the case of a strongly interacting liquid like ${}^4\text{He}$, the infamous roton minimum [27] leads to a critical velocity smaller than the speed of sound, $v_{\text{crit}} < c_s$, as shown in Fig. 1.2 (b).

The notions of Bose-Einstein condensation and superfluidity are closely related but not synonymous. As described above, there are systems like the ideal Bose gas that can have large condensate fractions below the critical temperature and yet they are not superfluid. On the other hand, close to absolute zero ${}^4\text{He}$ has a superfluid fraction near unity while its condensate fraction is less than 10% [39]. In general, experimentally determining superfluid behavior of quantum gases is highly non-trivial [49].

Throughout this thesis I only consider Bose-Einstein condensates of finitely interacting gases and therefore all of the systems studied in Part II are also superfluids. In Part III I also consider strongly interacting systems in one dimension. They are sometimes referred to as quasi-condensates since they are not Bose condensed but they still exhibit some degree of phase coherence. In particular, some degree of ‘off-diagonal long-range order’ (ODLRO), which is the term coined by Yang [50] for the general criterion proposed by Penrose and Onsager [51] for Bose-Einstein condensation. Namely, if the reduced single-particle density matrix (RSPDM) $\rho(\mathbf{r}, \mathbf{r}') = \langle \hat{\Psi}^\dagger(\mathbf{r})\hat{\Psi}(\mathbf{r}') \rangle$, which only depends on the relative distance $|\mathbf{r} - \mathbf{r}'|$ for a translationally invariant system, tends to some non-vanishing value

$$\lim_{|\mathbf{r}-\mathbf{r}'|\rightarrow\infty} \rho(\mathbf{r}, \mathbf{r}') = \frac{N_0}{V} \neq 0 \quad (1.39)$$

in the limit $|\mathbf{r} - \mathbf{r}'| \rightarrow \infty$, where N_0 is the number of atoms in the zero-momentum state and V is the volume. Most physical systems as well as the systems studied numerically in this thesis have a finite size and therefore it is necessary to slightly adapt the Penrose-Onsager criterion. The RSPDM is Hermitian and positive definite which means that it can be diagonalized according to

$$\rho(\mathbf{r}, \mathbf{r}') = \sum_n \lambda_n \varphi_n^*(\mathbf{r}') \varphi_n(\mathbf{r}) \quad (1.40)$$

in terms of its real and positive eigenvalues λ_n , also known as occupation numbers, and its eigenstates $\varphi_n(\mathbf{r})$, also known as natural orbitals [52]. The Penrose-Onsager

criterion now translates to

$$\lambda_0 \sim \mathcal{O}(N) \quad \text{and} \quad \lambda_{n>0} \sim \mathcal{O}(1), \quad (1.41)$$

i.e. the lowest single-particle orbital is macroscopically occupied, while in bosonic gases above the critical temperature for condensation as well as in fermionic gases we have $\lambda_n \sim \mathcal{O}(1) \forall n$. In the case of a degenerate ground state, one can have multiple macroscopically occupied orbitals in the form of fragmented Bose-Einstein condensates [53]. The quasi-condensates studied in Part III exhibit a behavior in between these two limiting cases. For example in the Tonks-Girardeau limit of infinitely strong repulsion, in which the one-dimensional bosons ‘fermionize’, we have $\lambda_0 \sim \mathcal{O}(N^{1/2})$ [54, 55].

1.5.2 Absence of Superfluidity: Insulating States

As we have seen in the previous sections, superfluidity is characterized by a spatially extended state with long-range phase coherence, hinting towards the spontaneously broken continuous $U(1)$ symmetry of the underlying Hamiltonian, and also at a finite compressibility of the system [56]. In contrast, the absence of superfluidity implies the existence of a localized, incoherent state with vanishing compressibility. In analogy to metal-insulator transitions in solid-state physics [57], such states are known as insulating states and often they are also studied in the same context, e.g. if the quantum gas is confined to a periodic lattice potential similar to electrons in a crystal. There are several mechanisms that can cause a system to localize, aptly termed ‘enemies of Bose-Einstein condensation’ by Nozières [56], with the most prominent ones being Mott localization and Anderson localization. Both of them assume the presence of a lattice potential and their exact interplay is still an active topic in the research of metal-insulator transitions [58, 59]. An introduction in the context of one-dimensional quantum gases can be found in Ref. [60].

Mott localization [61, 62] is caused by strong repulsive interactions between the particles, preventing them from moving between different lattice sites and therefore resulting in an insulating state with one particle per lattice site in the case of fermions or an integer number of particles per site in the case of bosons if additionally the number of particles and lattice sites is commensurate [63].

Anderson localization [64] is caused by disorder or randomness in the underlying lattice potential due to e.g. impurities or lattice defects. Beyond a critical degree of disorder, destructive interference of the wave function destroys the long-range phase coherence, resulting in an insulating state.

A hallmark of these insulating states is the emergence of a gap in the energy spectrum. In one-dimensional fermionic or ‘fermionized’ systems like the ones I am studying in Part III of this thesis, another mechanism for localization is the Peierls instability [65], which is triggered by electron-phonon interactions in its original context of condensed matter physics. Here, the system is able to lower its energy by creating an energy gap in the spectrum exactly at the Fermi wave vector k_F , if a suitable phononic excitation with wave vector $2k_F$ is present.

The gap is created because the electron-phonon coupling lowers (raises) the energy of states in the vicinity of k_F with $k < k_F$ ($k > k_F$) by the same mechanism that leads

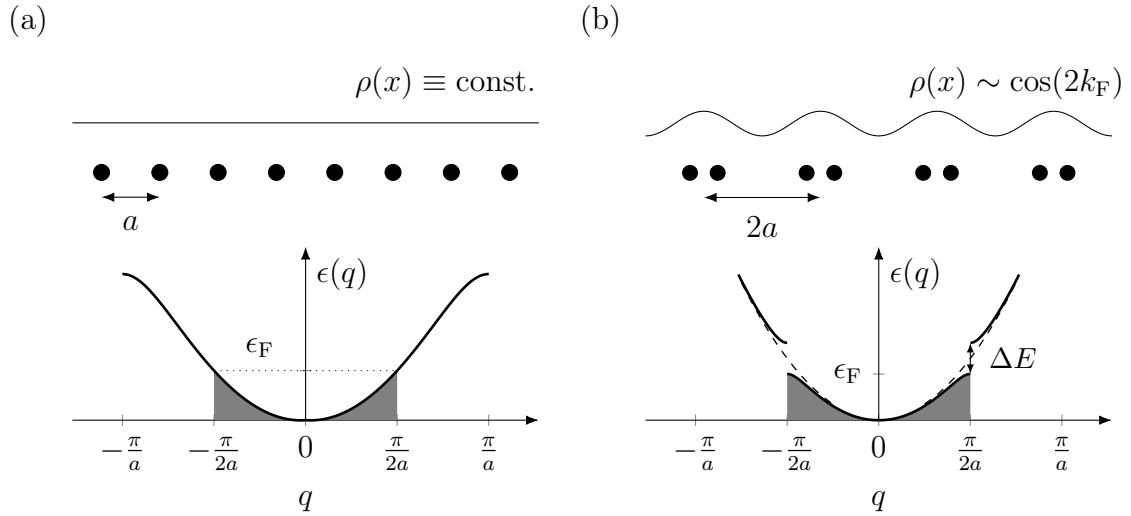


Figure 1.3: (a) A linear chain of atoms with regular spacing a between them and one electron per atom results in a constant charge density $\rho(x)$ and a half-filled band structure up to the Fermi energy ϵ_F at wave vector $k_F = \pi/2a$. The periodicity causes an energy gap with vanishing slope at the edge of the Brillouin zone at $q = \pi/a$. This configuration is unstable since the system can lower its energy by dimerizing and forming a crystal with twice the spacing $2a$ after undergoing the Peierls transition as shown in panel (b). This creates a new energy gap ΔE exactly at the Fermi surface and thereby lowers the energy of the states just below it and also forms a charge density wave $\rho(x) \sim \cos(2k_F)$.

to the development of energy bands in periodic potentials. But since only states up to wave vector k_F are occupied in the fermionic system, this leads to a net decrease in energy. Peierls used this argument to show that a one-dimensional crystal with one electron per atom is unstable. If the crystal has a lattice spacing of a , then this situation corresponds to a half-filled lattice up to $k_F = \pi/2a$ [see Fig. 1.3 (a)]. The system can lower its energy by dimerization, i.e. creating a new crystal structure with twice the spacing $2a$ that now contains 2 atoms per Brillouin zone [see Fig. 1.3 (b)]. The new periodicity $2a$ leads to the emergence of an energy gap at the edge of the new Brillouin zone which corresponds exactly to the Fermi edge of the original crystal k_F , thereby leading to a net decrease in energy. The resulting spatial modulation $\rho(x) \sim \cos(2k_F x)$ of the electrons in the dimerized state is known as charge-density wave [66].

1.6 Lower-Dimensional Systems

So far, we only discussed three-dimensional quantum gases. Lower-dimensional systems are interesting because they offer a behavior often fundamentally different from their three-dimensional counterparts, as we will see in the following section, and particularly in the one-dimensional case they often allow for analytic solutions [67].

Experimentally, they can be realized by trapping atoms in highly anisotropic geometries that freeze out the dynamics along one or two axes. For example, if in a harmonic potential the trapping frequencies fulfill $\omega_{\perp} := \omega_{y,z} \gg \omega_x =: \omega$ and if additionally the chemical potential of the system does not exceed $\hbar\omega_{\perp}$, then it remains in the ground state of the trap in the y - and z -directions. Since the ground state has a size on the order of $d_{\perp} = \sqrt{\hbar/m\omega_{\perp}} \ll d = \sqrt{\hbar/m\omega}$ in these directions, the system can be considered to be quasi-one-dimensional. Often optical lattices are employed to create arrays of quasi-one-dimensional tubes with this technique. In this way, it was possible to successfully demonstrate the fermionization of strongly repulsive interacting bosons in one dimension [68, 69] or to study the equilibration properties of a 1D Bose gas [70].

First, let us examine the effect of dimensionality on Bose-Einstein condensation. In general, Eq. (1.12) in Section 1.3 for the number of thermal atoms can be written as [27]

$$N_T = \int_0^{\infty} d\epsilon \frac{\rho(\epsilon)}{e^{\beta\epsilon} - 1} = \int_0^{\infty} d\epsilon \frac{C_{\alpha}\epsilon^{\alpha-1}}{e^{\beta\epsilon} - 1} = C_{\alpha} (k_B T)^{\alpha} \int_0^{\infty} dx \frac{x^{\alpha-1}}{e^x - 1} = C_{\alpha} (k_B T)^{\alpha} \Gamma(\alpha)\zeta(\alpha), \quad (1.42)$$

where we assume that the density of states is of the form $\rho(\epsilon) = C_{\alpha}\epsilon^{\alpha-1}$ with some coefficient α depending on the dimension of the system and where $\Gamma(\alpha)$ and $\zeta(\alpha)$ denote the gamma function and the Riemann zeta function respectively.

For a uniform, non-interacting Bose gas in free space in d dimensions we have $\alpha = d/2$ and therefore the integral in Eq. (1.42) diverges for $d < 3$, preventing the existence of Bose-Einstein condensates in true one-dimensional and two-dimensional systems. If the non-interacting Bose gas is harmonically trapped instead, we have $\alpha = d$, which means that the integral now converges at least for the $d = 2$ case, in principle allowing for the existence of a true 2D BEC in a harmonic trap.

For the uniform case, these observations are a direct result of the Mermin-Wagner-Hohenberg theorem, which states that in one-dimensional and two-dimensional homogeneous systems continuous symmetries cannot be spontaneously broken at finite temperatures $T > 0$ [71, 72], which prevents the existence of off-diagonal long-range order necessary for Bose-Einstein condensation. However, in two dimensions there is another type of superfluid quasi-condensate (see the discussion in the previous section) even in uniform systems, which is reached by a topological, infinite-order phase transition of Berezinskii-Kosterlitz-Thouless (BKT) type that does not involve a spontaneous breaking of a continuous symmetry [73, 74]. In a spherically symmetric 2D system of area $A = \pi R^2$ and density n_{2D} , the energy of a single vortex with a radius on the order of the healing length ξ is up to a constant given by [27]

$$E \simeq \pi n_{2D} \frac{\hbar^2}{m} \ln \left(\frac{R}{\xi} \right). \quad (1.43)$$

The number of different possible locations for the vortex $\sim R^2/\xi^2$ results in an entropy $S = 2k_B \ln(R/\xi)$. Creating a vortex therefore changes the free energy of the system by an amount

$$\Delta F = E - TS = \left(\pi n_{2D} \frac{\hbar^2}{m} - 2k_B T \right) \ln \left(\frac{R}{\xi} \right) \quad (1.44)$$

and one can immediately see that there is a phase transition indicated by $\Delta F = 0$, where above a temperature

$$T_{\text{BKT}} = \frac{\pi n_{2\text{D}} \hbar^2}{2mk_{\text{B}}} \quad (1.45)$$

the change in free energy becomes negative and it is favorable for the system to create a vortex. However, once there is more than one vortex their interactions need to be taken into account as well. The total energy of two vortices with vorticity l_1 and l_2 at a distance $\xi \ll d \ll R$ is [75]

$$E \simeq \pi n_{2\text{D}} \frac{\hbar^2}{m} (l_1 + l_2)^2 \ln \left(\frac{R}{\xi} \right) + 2\pi n_{2\text{D}} \frac{\hbar^2}{m} l_1 l_2 \ln \left(\frac{\xi}{d} \right). \quad (1.46)$$

This expression is minimized for a vortex-antivortex pair with $l_1 = -l_2$, with the added benefit that the unphysical divergence of the energy in the thermodynamic limit $R \rightarrow \infty$ disappears. The system will therefore always prefer states with vanishing total vorticity $\sum_i l_i = 0$ and the BKT transition can be understood as the breaking up of bound vortex pairs of opposite circulation into independent vortices above a temperature T_{BKT} . In a quasi-2D quantum gas a Berezinskii-Kosterlitz-Thouless type transition was first observed by Hadzibabic et al. in 2006 [76].

In the presence of interactions, a 2D superfluid quasi-condensate can also be reached at finite temperatures and the critical temperature can be related to the interaction strength for an extremely dilute system as shown in Ref. [77]. The question of how interactions affect the existence of a true 2D BEC in trapped systems according to Eq. (1.42) and how this relates to the BKT transition was at the center of a lengthy debate, see e.g. Ref. [29] and references therein. Eventually, the existence of two distinct superfluid phases, a true condensate for low temperatures $0 < T < T_c$ and a quasi-condensate for intermediate temperatures $T_c < T < T_{\text{BKT}}$, were predicted theoretically [78] and confirmed with numerical simulations [79].

Finally, in one-dimensional cold atomic systems one of the most striking differences can be seen in the interaction strength

$$\begin{aligned} g_{1\text{D}} &= -\frac{2\hbar^2}{ma_{1\text{D}}} \\ &= \frac{4\pi\hbar^2 a_s}{m} \frac{1}{\pi d_{\perp}^2 \left(1 - C \frac{a_s}{d_{\perp}}\right)} \approx 2\hbar\omega_{\perp} a_s \end{aligned} \quad (1.47)$$

of an ultracold bosonic gas in a one-dimensional geometry [38]. It is inversely proportional to the 1D scattering length $a_{1\text{D}}$ and has the opposite sign compared to $g_{3\text{D}}$ in Eq. (1.6). The second line in Eq. (1.47) shows the relation to the physical three-dimensional scattering length a_s , where $C \approx 1.46$ is a constant and $d_{\perp} = \sqrt{\hbar/m\omega_{\perp}}$ is the radial confinement. The final approximation nicely shows how increasing the radial trapping frequency ω_{\perp} and making the system ‘more one-dimensional’ results in a stronger interaction.

Furthermore, since particles in one dimension can only move along a single axis without being able to avoid each other, any excitation in 1D has to be of a collective

nature. Without further trapping potentials along the axis of motion, the Hamiltonian of this situation reads

$$\hat{H} = -\frac{\hbar^2}{2m} \sum_i \frac{\partial^2}{\partial x_i^2} + g_{1D} \sum_{i<j} \delta(|x_i - x_j|) \quad (1.48)$$

and was solved by Lieb and Liniger [80, 81]. The system is fully characterized by the Lieb-Liniger parameter $\gamma = mg_{1D}/\hbar^2 n_{1D}$ relating the interaction energy to the kinetic energy via the line density n_{1D} . The reduced dimensionality has the peculiar effect that counterintuitively the limit of strong interactions $\gamma \gg 1$ can also be reached for low densities n_{1D} .

In the limit of infinitely strong repulsion $\gamma \rightarrow \infty$, the probability of finding two bosons at the same position $x_1 = x_2$ vanishes. This is reminiscent of the behavior of two non-interacting, identical fermions obeying the Pauli exclusion principle. The bosons can be thought of as impenetrable spheres in this case and the system is known as a Tonks-Girardeau gas. Their wave function can be obtained by symmetrizing the wave function of the corresponding system comprised of non-interacting, identical fermions, as described by the Bose-Fermi mapping theorem [82]. The bosonic wave function Ψ_B is therefore calculated as

$$\begin{aligned} \Psi_B(x_1, x_2, \dots, x_N) &= A(x_1, x_2, \dots, x_N) \Psi_F(x_1, x_2, \dots, x_N) \\ &= \prod_{1 \leq i < j \leq N} \text{sgn}(x_i - x_j) \Psi_F(x_1, x_2, \dots, x_N) \end{aligned} \quad (1.49)$$

with the symmetrizing function $A(x_1, x_2, \dots, x_N)$ and where the fermionic wave function Ψ_F is obtained from the single-particle eigenstates ϕ_n of the corresponding Hamiltonian via the Slater determinant

$$\Psi_F(x_1, x_2, \dots, x_N) = \frac{1}{\sqrt{N!}} \begin{vmatrix} \phi_1(x_1) & \phi_1(x_2) & \cdots & \phi_1(x_N) \\ \phi_2(x_1) & \phi_2(x_2) & \cdots & \phi_2(x_N) \\ \vdots & \vdots & \ddots & \vdots \\ \phi_N(x_1) & \phi_N(x_2) & \cdots & \phi_N(x_N) \end{vmatrix}. \quad (1.50)$$

For example, the ground state of a simple two-particle Tonks-Girardeau gas is therefore given by

$$\Psi_0^B(x_1, x_2) = |\Psi_0^F(x_1, x_2)| = \frac{1}{\sqrt{2}} |\phi_0(x_1)\phi_1(x_2) - \phi_0(x_2)\phi_1(x_1)|, \quad (1.51)$$

and most importantly, the line densities of a bosonic Tonks-Girardeau and a spin-polarized fermionic gas in an equivalent setting are identical

$$\rho(x) = |\Psi_B(x)|^2 = |\Psi_F(x)|^2 = \int dx_2 \dots dx_N |\Psi_F(x, x_2, \dots, x_N)|^2 = \sum_{n=1}^N |\phi_n(x)|^2 \quad (1.52)$$

and simply obtained from summing up all occupied single-particle eigenstates, which we will use in Part III of this thesis.

While in general all local properties of the bosonic Tonks-Girardeau gas are identical to their fermionic counterparts, they differ for example in their momentum distributions $n(k)$ [52], which can be calculated from the RSDPM as

$$n(k) = \frac{1}{2\pi} \int dx dx' \rho(x, x') e^{ik(x-x')} = \sum_i \lambda_i \tilde{\phi}_i^*(k) \tilde{\phi}_i(k) \quad (1.53)$$

with the Fourier transforms $\tilde{\phi}_i(k)$ of the natural orbitals and where we express the momentum p in units of \hbar according to $p = \hbar k$. The fermionic momentum distribution $n_F(k) = (\Theta(k+k_F) - \Theta(k-k_F))/2k_F$ is simply constant up to the Fermi momentum k_F , while the bosonic Tonks-Girardeau momentum distribution is strongly peaked around $k = 0$ and decays as

$$n_B(k \rightarrow \infty) \sim \frac{1}{k^4} \quad (1.54)$$

at large momenta as a result of the δ -function pseudo-potential for the interactions [83–85]. The fermionized Tonks-Girardeau gas has already been observed experimentally [68, 69], even for just two particles [86]. A detailed review of one-dimensional bosonic systems that covers many of the topics touched upon in this thesis can be found in Ref. [87].

Chapter 2

Numerical Methods

This chapter introduces the numerical methods that have been used to obtain a majority of the results presented in this thesis, namely the Fourier split-step method and exact diagonalization, as well as ways to benchmark the numerical results.

2.1 Fourier Split-Step Method

The (nonlinear) Schrödinger equations studied in quantum mechanics cannot be solved analytically in most cases, particularly in three-dimensional systems, and therefore need to be solved numerically. There are a variety of methods available for solving such partial differential equations, e.g. implicit Euler methods or Crank-Nicholson and Runge-Kutta schemes [88, 89]. Throughout this thesis, I will mostly use the simple and efficient Fourier split-step method, which provides sufficient accuracy at reasonable numerical cost and is widely used for cold atomic systems [90–95], but also in other areas of physics like fiber optics, where the propagation of wave packets through an optical fiber is also described by a nonlinear Gross-Pitaevskii type equation [96].

We are considering a general Schrödinger equation

$$i\hbar \frac{\partial \Psi(\mathbf{r}, t)}{\partial t} = \hat{H} \Psi(\mathbf{r}, t) = \left(\hat{K} + \hat{V} \right) \Psi(\mathbf{r}, t) \quad (2.1)$$

consisting of a kinetic energy term $\hat{K} = \hat{\mathbf{p}}^2/2m$ acting in momentum space and a local potential term $\hat{V}(\mathbf{r})$ acting in position space, whose formal solution is given by

$$\Psi(\mathbf{r}, t) = e^{-i\hat{H}t/\hbar} \Psi(\mathbf{r}, 0) = e^{-i(\hat{K}+\hat{V})t/\hbar} \Psi(\mathbf{r}, 0) . \quad (2.2)$$

The central idea of split-step methods is now to separate the sum of momentum and potential operators in the exponent of Eq. (2.2) into a product of exponential functions since their individual effects on the wave function can be calculated explicitly, in contrast to their combined effect. Position and momentum in quantum mechanics are canonical conjugate quantities and due to the non-vanishing commutator $[\hat{K}, \hat{V}] \neq 0$ such a decomposition generally involves an infinite product, which can be obtained e.g. via the Baker-Campbell-Hausdorff formula [30]. For computational purposes it is necessary to find a truncated finite product that provides a good compromise between

numerical effort and accuracy compared to the exact expression. If we evolve the wave function by a small time step dt , then a Taylor expansion of the exact expression reads

$$e^{-i(\hat{K}+\hat{V})dt/\hbar} = \hat{\mathbb{1}} + dt \left(\frac{-i}{\hbar} \right) (\hat{K} + \hat{V}) + \frac{dt^2}{2} \left(\frac{-i}{\hbar} \right)^2 (\hat{K}^2 + \hat{K}\hat{V} + \hat{V}\hat{K} + \hat{V}^2) + \mathcal{O}(dt^3), \quad (2.3)$$

while a naive separation of the exponentiated product into a product of exponents yields

$$e^{-i\hat{K}dt/\hbar}e^{-i\hat{V}dt/\hbar} \approx \hat{\mathbb{1}} + dt \left(\frac{-i}{\hbar} \right) (\hat{K} + \hat{V}) + \frac{dt^2}{2} \left(\frac{-i}{\hbar} \right)^2 (\hat{K}^2 + 2\hat{K}\hat{V} + \hat{V}^2), \quad (2.4)$$

which differs in the second-order term compared to Eq. (2.3). Therefore, this approximation introduces an error on the order of $\mathcal{O}(dt^2)$ and is also known as first-order accurate asymmetric Lie-Trotter splitting due to its similarity with the Lie-Trotter product formula in the limit $dt \rightarrow 0$ [97]. A more accurate scheme is given by the second-order accurate symmetric Strang splitting [98]

$$e^{-i(\hat{K}+\hat{V})dt/\hbar} = e^{-i\hat{V}dt/2\hbar}e^{-i\hat{K}dt/\hbar}e^{-i\hat{V}dt/2\hbar} + \mathcal{O}(dt^3), \quad (2.5)$$

which only differs from Eq. (2.3) starting with the third-order term.

The time steps in position space can simply be evaluated by expressing both the wave function and the potential term on a discrete position grid $\mathbf{r} \in \{\mathbf{r}_1, \dots, \mathbf{r}_N\}$ and computing the resulting element-wise or Hadamard product $\exp(-i\hat{V}dt/2\hbar) \circ \Psi(\mathbf{r}, t)$ [99]. If using a first-order accurate scheme, it is also possible to compute the momentum term in position space within the same order of accuracy since $\exp(-i\hat{K}dt/\hbar) = \hat{\mathbb{1}} - i\frac{dt}{\hbar}\frac{\hat{\mathbf{p}}^2}{2m} + \mathcal{O}(dt^2)$. The momentum operator $\hat{\mathbf{p}}^2 = -\hbar^2\nabla^2$ is then evaluated by explicitly performing the spatial derivative on the chosen position grid, e.g. by using a finite difference scheme similar to the one introduced in the following section about exact diagonalization. However, this method introduces an additional error based on the grid size and is not very practical except for one-dimensional systems. A better approach is to Fourier transform the wave function to momentum space $\Psi(\mathbf{k}, t) = \mathcal{F}[\Psi(\mathbf{r}, t)]$, where the momentum term can be evaluated with the same simple element-wise Hadamard product

$$\exp(-i\hat{K}dt/\hbar)\Psi(\mathbf{r}, t) \implies \exp\left(-i\frac{dt}{\hbar}\frac{\hbar^2\mathbf{k}^2}{2m}\right) \circ \Psi(\mathbf{k}, t) \quad (2.6)$$

due to the formal mapping of derivation and multiplication $\partial_x f(x) \leftrightarrow ik\tilde{f}(k)$ during Fourier transformation. The momentum grid cannot be chosen freely but depends on the used position grid according to

$$k_{\max}^i = \frac{2\pi}{\Delta r^i} \quad \text{for } i \in \{x, y, z\} \quad (2.7)$$

as a direct result of the uncertainty relation. Furthermore, as a result of the Nyquist sampling theorem [100] the grid spacings Δr^i need to be chosen smaller than half the size of the smallest spatial structure present in the wave function in order to

be able to faithfully resolve and simulate the system on the grid. For example, a harmonically trapped BEC in the Thomas-Fermi regime has an extent on the order of $2R_{\text{TF}} = 2\sqrt{2\mu_{\text{TF}}/m\omega^2}$ (see Section 1.4), while the smallest spatial features are on the order of the healing length $\xi = (8\pi n a_s)^{-1/2} \approx \sqrt{\hbar^2/2m\mu_{\text{TF}}}$ [40]. The required number of grid points in each spatial direction is therefore on the order of

$$N_{\text{grid}} \gtrsim \frac{2R_{\text{TF}}}{\xi/2} = \frac{8\mu_{\text{TF}}}{\hbar\omega} = 4 \left(15N \frac{a_s}{x_0} \right)^{2/5}, \quad (2.8)$$

with the harmonic oscillator length scale $x_0 = \sqrt{\hbar/m\omega}$. For a typical ^{87}Rb -BEC of $N = 10^5$ atoms with a scattering length of approximately $a_s \approx 100 a_0$ Bohr radii and $x_0 \approx 1.5 \mu\text{m}$ [101], this leads to $N_{\text{grid}} \gtrsim 123$. Ideally N_{grid} is chosen as a power of two however, in order to considerably speed-up the numerical Fast Fourier Transforms (FFT) [102], e.g. $N_{\text{grid}} = 2^7 = 128$ in that case.

Finally, the complete procedure for evolving the wave function in time via the symmetric Strang splitting method is then given by repeatedly advancing it first by half a time step in position space, Fourier transforming it to momentum space and advancing it by a full time step before Fourier transforming back to position space and advancing by another half time step. Or expressed in equation form

$$\Psi(\mathbf{r}, t + dt) \approx \hat{U}_{\mathbf{r}} \left(\frac{dt}{2} \right) \mathcal{F}^{-1} \left[\hat{U}_{\mathbf{k}}(dt) \mathcal{F} \left[\hat{U}_{\mathbf{r}} \left(\frac{dt}{2} \right) \Psi(\mathbf{r}, t) \right] \right], \quad (2.9)$$

where \mathcal{F} denotes the Fourier transform and where we introduce the shorthand notation $\hat{U}_{\mathbf{r}}(dt) = \exp(-i\hat{V}dt/\hbar)$ and $\hat{U}_{\mathbf{k}}(dt) = \exp(-i\hat{K}dt/\hbar)$ for the evolution operators in position and momentum space respectively.

If a nonlinear term such as in the Gross-Pitaevskii equation is present in the potential part \hat{V} , the accuracy of the split-step method crucially depends on which version of the wave function during a combined evolution step is used for evaluating the density in the nonlinear term as Javanainen and Ruostekoski show in Ref. [93]. They find that always using the most recent wave function for calculating the density, i.e. updating the nonlinear term after the momentum space step and before the final position space half-step when using the symmetric Strang splitting, guarantees the same order of accuracy as for the linear Schrödinger equation. Since the nonlinear term can be considered as a time-dependent addition to the external potential, the same argument should also hold in general if the external potential itself is time-dependent.

Most of the results presented in Part II of this thesis were obtained using the Fourier split-step method described above for studying the dynamics of a quantum system and evolving a known initial state in time. An equally important application of this method is to find unknown ground states of quantum systems whose Schrödinger equations cannot be solved analytically by performing a so-called Wick rotation [103] for the time operator according to $t \rightarrow -it$, which is akin to evolving the system in imaginary time. Most of the results presented in Part III of this thesis were obtained using this imaginary time evolution. Any wave function that has a finite overlap with the unknown ground state can be expressed in terms of eigenstates $|\phi_n\rangle$ of the

Hamiltonian, so that the formal solution (2.2) after applying the Wick rotation reads

$$\Psi(\mathbf{r}, -it) = e^{-\hat{H}t/\hbar}\Psi(\mathbf{r}, t) = \sum_n c_n e^{-E_n t/\hbar} |\phi_n(\mathbf{r})\rangle, \quad (2.10)$$

with eigenenergies E_n and basis coefficients c_n . The imaginary time evolution works because the contributions from different eigenstates decay exponentially in time at different rates according to their corresponding energy E_n . The ground state, i.e. the state with the lowest energy E_0 , decays the slowest and should therefore become the dominant contribution the longer the system is evolved in imaginary time, while renormalizing the wave function after each time step to account for the gradual loss of density. If the imaginary time evolution with subsequent renormalization is continued until the wave function converges, then ideally the system has reached its ground state according to $\Psi(\mathbf{r}, -it \rightarrow \infty) \rightarrow |\phi_0(\mathbf{r})\rangle$ and we can immediately obtain both the corresponding wave function and energy.

The rate of convergence depends on the quality of the chosen initial state in terms of similarity to the unknown ground state and on the energy level structure of the underlying Hamiltonian. There is a risk of not obtaining the true ground state if the Hamiltonian has many eigenstates with similar energy or if there is a higher lying metastable state.

We also use the Fourier split-step method in Chapters 3 and 8 for real and imaginary time propagation of the many-body wave function of two-particle and three-particle systems with finite interactions in one spatial dimension. Interpreting the particle coordinates as spatial dimensions allows one to use the same numerical framework for the algorithm as for the wave function of a BEC obeying the Gross-Pitaevskii equation in two or three dimensions. In this case, there is no nonlinear term and depending on the numerical platform it can be cumbersome to properly transform the potential terms for each particle along the correct dimension. However, for two particles the contact interaction becomes a simple diagonal matrix

$$(V_{\text{int}})_{ij} = [g\delta(x_1 - x_2)]_{ij} = g\delta[\Delta x(i - j)] = \frac{g}{\Delta x}\delta_{ij}, \quad (2.11)$$

where the finite position grid with spacing Δx leads to a rescaling of the interaction strength.

When implementing the split-step Fourier method, the main numerical cost is caused by repeatedly Fourier transforming the wave function. The element-wise multiplications both in position and momentum space have a complexity on the order of $\mathcal{O}(N_{\text{grid}})$, while commonly used Fast-Fourier-Transform algorithms like the Cooley-Tukey method [104] have a higher complexity on the order of $\mathcal{O}(N_{\text{grid}} \log(N_{\text{grid}}))$. Particularly for longer evolutions in real-time or when simulating fast dynamic processes that require small time steps in 2D and 3D systems, this can quickly result in very time-consuming numerical simulations. For this reason, I used a modified version of the open-source *GPUE* codebase [105] developed by Schloss and O’Riordan for simulating the long-time dynamics of a three-dimensional BEC after applying interaction ramps in Chapter 4. The codebase implements the split-step Fourier method on graphics processing units (GPUs), making use of their highly parallel architecture especially

in order to speed-up the FFT calculations and resulting in about two orders of magnitude faster execution times compared to e.g. a *Matlab* implementation [106].

2.2 Exact Diagonalization

The density of the immersed Tonks-Girardeau gas in Chapter 7 can be constructed by summing up the lowest eigenstates of the corresponding single-particle Hamiltonian, since the Bose-Fermi mapping theorem states that all local properties of the TG gas are equivalent to an identical gas made up of fermions instead. These eigenstates can be obtained by the so-called ‘exact diagonalization’ of the single-particle Hamiltonian in which its Hilbert space is truncated to a finite dimension by discarding certain elements of the chosen basis, expressing the Hamiltonian in the truncated basis and then in most cases numerically diagonalizing the resulting matrix.

When exact diagonalization is used for solving Hamiltonians of interacting many-body systems, the treatment is often restricted to very small basis sets due to the exponential growth of the Hilbert space dimension with particle numbers and the technical limitations for the size of numerically diagonalizable matrices [107]. In such cases it can be advantageous to work in a basis in which the single-particle part of the Hamiltonian is already diagonal, e.g. the harmonic oscillator basis for a harmonically trapped system, in order to achieve higher precision for the numerical results, despite the limited basis set [108, 109]. In our case, this issue is not a concern, since we are only dealing with a single-particle Hamiltonian in one spatial dimension

$$\hat{H} = -\frac{\hbar^2}{2m} \frac{\partial^2}{\partial x^2} + V(x). \quad (2.12)$$

We can therefore work in the position basis and achieve nearly arbitrary precision simply by using smaller and smaller rasterizations when discretizing position space. The Hilbert space truncation is achieved by restricting the position axis to some physically relevant interval, e.g. between $[-a, a]$, and dividing it into $N_{\text{grid}} - 1$ identical parts of length $\Delta x = 2a/(N_{\text{grid}} - 1)$ which yields N_{grid} equidistant position grid points according to $x_i = -a + (i - 1)\Delta x$ for $i = 1, \dots, N_{\text{grid}}$. The kinetic energy term in Eq. (2.12) is approximated in this truncated position basis by means of a finite difference scheme [110] for the second spatial derivative according to

$$\left. \frac{\partial^2 \psi}{\partial x^2} \right|_{x=x_i} \approx \frac{\psi_{i+1} - 2\psi_i + \psi_{i-1}}{\Delta x^2} \quad (2.13)$$

and using the values of the wave function $\psi_i = \psi(x_i)$ at the grid points, which leads to an error on the order of $\mathcal{O}(\Delta x^2)$. The potential term is already diagonal in this basis and simply expressed at the grid points as $V_i = V(x_i)$.

This leads to a tridiagonal $N_{\text{grid}} \times N_{\text{grid}}$ -matrix

$$\hat{H} = -\frac{\hbar^2}{2m\Delta x^2} \begin{pmatrix} -2 & 1 & 0 & \cdots & 0 \\ 1 & -2 & 1 & \ddots & \vdots \\ 0 & 1 & \ddots & \ddots & 0 \\ \vdots & \ddots & \ddots & \ddots & 1 \\ 0 & \cdots & 0 & 1 & -2 \end{pmatrix} + \text{diag}(V_1, V_2, \dots, V_{N_{\text{grid}}}) \quad (2.14)$$

which is then diagonalized in order to obtain the eigenvalues and eigenstates. The accuracy of this numerical scheme is determined by the grid spacing Δx and can be improved by increasing the number of grid points for a fixed position interval or by using a higher order finite difference scheme [110] for fixed grid spacing, e.g.

$$\left. \frac{\partial^2 \psi}{\partial x^2} \right|_{x=x_i} = \frac{-\psi_{i+2} + 16\psi_{i+1} - 30\psi_i + 16\psi_{i-1} - \psi_{i-2}}{\Delta 12x^2} + \mathcal{O}(\Delta x^4). \quad (2.15)$$

However, this has the disadvantage that the resulting matrix is no longer tridiagonal, which generally increases the effort resp. duration of numerically diagonalizing it [111].

2.3 Benchmarking: Analytically Solvable Models

In order to test the accuracy of numerical solutions, one can benchmark the results against known analytical solutions in certain limiting cases. I will not provide explicit benchmarks here, as the split-step and exact diagonalization methods used in this thesis are commonly known and simple enough that their accuracy can be controlled essentially entirely via the position grid spacing as well as the time step. Instead, I will just describe the general approach and some suitable models for benchmarking.

Using the Fourier split-step method with imaginary time propagation for the Gross-Pitaevskii equation of a harmonically trapped system, one can for example check if the obtained ground state and energy are close to the values expected from the Thomas-Fermi approximation in Section 1.4 in the limit of large systems and reasonably strong repulsion and similarly if they give the appropriate harmonic oscillator ground state for the ideal gas in the limit of vanishing interaction. In the case of real-time propagation, one needs to check that the energy of the system is conserved if one of its eigenstates is propagated.

For the exact diagonalization method for a single particle, one can also make use of the well-known harmonic oscillator solutions, particularly to check the accuracy of higher lying states, which are not immediately accessible with the split-step method, or similarly the analytic solutions for a particle in an infinite box.

Another important benchmark for the exact diagonalization scheme in the presence of interactions, but also for the split-step method if used for a many-body wave-function in the way described in the paragraph above Eq. (2.11), involves the analytic solution of two harmonically trapped interacting atoms.

The interaction between two cold atoms in a quasi-one-dimensional harmonic trap can be described by the pseudo-potential introduced previously and a Hamiltonian that

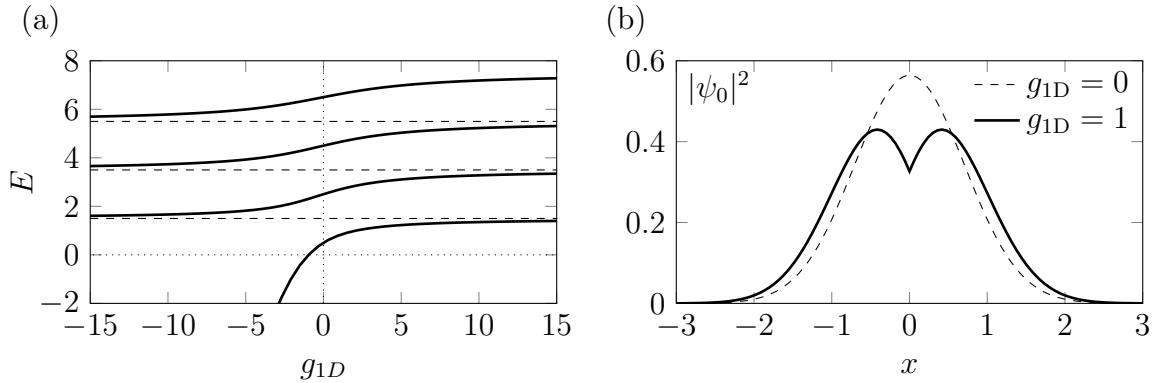


Figure 2.1: (a) Eigenenergies for the one-dimensional relative motion of two harmonically trapped cold atoms interacting with strength g_{1D} . The eigenenergies belonging to even states (solid lines) become degenerate with the unperturbed odd states (dashed lines) as $|g_{1D}| \rightarrow \infty$. (b) Groundstate density $|\psi_0|^2$ (solid line) for the relative motion and an interaction strength of $g_{1D} = 1$. The δ -barrier causes a notable cusp around $x = 0$ compared to the unperturbed Gaussian ground state (dashed line).

reads

$$\hat{H} = \sum_{i=1}^2 \left(-\frac{\hbar^2}{2m} \frac{\partial^2}{\partial x_i^2} + \frac{1}{2} m \omega^2 x_i^2 \right) + g_{1D} \delta(x_2 - x_1), \quad (2.16)$$

where the interaction strength $g_{1D} \approx \hbar \omega_{\perp} a_s$ can be tuned both by the original three-dimensional scattering length a_s and the transverse confinement ω_{\perp} [38]. For convenience we switch to dimensionless harmonic oscillator units in the following and express all lengths in units of $x_0 = \sqrt{\hbar/m\omega}$, energy in units of $\hbar\omega$ and the interaction strength in units of $\hbar\omega x_0$. By changing to center-of-mass and relative coordinates $X = \frac{1}{\sqrt{2}}(x_1 + x_2)$ and $x = \frac{1}{\sqrt{2}}(x_1 - x_2)$, the problem can be separated into a simple harmonic oscillator Hamiltonian for the center-of-mass motion and a harmonic oscillator with an additional δ -shaped barrier in its center for the relative motion

$$\hat{H} = \left(-\frac{1}{2} \frac{\partial^2}{\partial X^2} + \frac{1}{2} X^2 \right) + \left(-\frac{1}{2} \frac{\partial^2}{\partial x^2} + \frac{1}{2} x^2 + \frac{g_{1D}}{\sqrt{2}} \delta(x) \right), \quad (2.17)$$

which can both be solved analytically [112]. The odd eigenstates of the Hamiltonian for the relative motion vanish at the position of the barrier at $x = 0$ and they are therefore given by the unperturbed harmonic oscillator eigenstates. The even eigenstates are given by

$$\psi_i(x) = \mathcal{N}_i U \left(\frac{1}{4} - \frac{E_i}{2}, \frac{1}{2}, x^2 \right) e^{-x^2/2}, \quad i = 0, 2, 4, \dots, \quad (2.18)$$

with a normalizing constant \mathcal{N}_i and the confluent hypergeometric function of the second kind $U(a, b, z)$, also known as Kummer or Tricomi function [113]. The corresponding eigenenergies E_i are given by the relation

$$g_{1D} = -2\sqrt{2} \frac{\Gamma(-\frac{E_i}{2} + \frac{3}{4})}{\Gamma(-\frac{E_i}{2} + \frac{1}{4})}, \quad i = 0, 2, 4, \dots, \quad (2.19)$$

and are plotted in Fig. 2.1 (a). They become degenerate with the unperturbed odd eigenenergies $E_i = i + \frac{1}{2}$, $i = 1, 3, 5, \dots$, as $|g_{1D}| \rightarrow \infty$. Fig. 2.1 (b) shows the perturbed ground state for $g_{1D} = 1$. The δ -barrier causes a visible cusp around $x = 0$ and the wave function eventually vanishes at that point $\psi(x = 0) \rightarrow 0$ in the limit $|g_{1D}| \rightarrow \infty$.

Another important application of these exact solutions is the effective interaction approach in exact diagonalization schemes. By rescaling the interaction strength in an appropriate way, one can exactly reproduce the correct low-lying spectrum [114, 115].

Part II

Quantum Control, Shortcuts to Adiabaticity & Feshbach Engines

Chapter 3

Shortcuts to Adiabaticity

According to the adiabatic theorem, a quantum system subject to some perturbation will remain in its instantaneous eigenstate if the perturbation is applied slow enough [116]. This entails that in order to control quantum systems with a high degree of fidelity and avoid unwanted excitations, any manipulation needs to be performed on a timescale that is slow compared to the intrinsic one determined by its energy levels. This leaves very little room to achieve the simple, fast and reliable control that is needed e.g. for the development of quantum technologies [4] as the lifetime of quantum systems is limited by their susceptibility to decoherence if they are not perfectly isolated from the environment.

Besides improving said technology for confining and isolating them from the environment, another approach for enhancing the control over quantum systems is to develop novel protocols for their manipulation. One prominent type of such protocols are so-called shortcuts to adiabaticity (STA), which allow the system to mimic adiabatic evolution in a finite time. The term STA was first coined by Chen et al. in Ref. [117], but similar concepts have been applied already earlier, most notably by Demirplak and Rice [118] and Berry [119]. The goal they try to achieve is closely related to optimal control theory [120] and there is a wide variety of different techniques to construct such shortcuts, usually using approaches well suited for a specific target system. Detailed reviews of the most common techniques and examples of their experimental applications can be found in Refs. [15, 121].

For instance, successful realizations of shortcuts to adiabaticity include improving the fidelity of processes important for the operation of quantum computers such as executing quantum gates on a single superconducting qubit [122] or transporting trapped ions as a means of quantum information transfer [123]. Fast and controlled transport has also been realized in cold atomic systems [124, 125] as well as the compression and expansion of Bose-Einstein condensates via their trapping potentials [126, 127].

In this chapter I introduce the concepts of counterdiabatic driving and inverse engineering that are the basis of the results presented in the subsequent Chapters 4 and 5 as well as a class of general shortcuts for scale-invariant interacting many-body systems that require the driving of both trapping frequencies and interaction strengths. I then extend a known pure interaction shortcut for attractive 1D Bose-Einstein condensates to higher dimensions and derive a novel interaction shortcut for repulsive BECs in the Thomas-Fermi regime.

3.1 Counterdiabatic Driving, Inverse Engineering and Quantum Speed Limits

One of the most straightforward approaches for constructing a shortcut to adiabaticity is counterdiabatic driving (CD), in which an extra term \hat{H}' that perfectly cancels all non-adiabatic contributions is added to the original Hamiltonian \hat{H}_0 . In this way, implementing the counterdiabatic Hamiltonian $\hat{H}_{\text{CD}} = \hat{H}_0 + \hat{H}'$ ensures that the system remains adiabatic at all times. For a time-dependent Hamiltonian $\hat{H}_0 = \sum_n E_n(t) |n(t)\rangle \langle n(t)|$ with instantaneous eigenvalues $E_n(t)$ and instantaneous eigenstates $|n(t)\rangle$ the counterdiabatic Hamiltonian can be computed to be [119]

$$\begin{aligned} \hat{H}_{\text{CD}} &= \hat{H}_0 + \hat{H}' \\ &= \sum_n E_n(t) |n(t)\rangle \langle n(t)| + i\hbar \sum_n [|\partial_t n(t)\rangle \langle n(t)| - \langle n(t)| \partial_t n(t)\rangle |n(t)\rangle \langle n(t)|] . \end{aligned} \quad (3.1)$$

This simple and general expression comes with the large drawback that it requires exact knowledge of the instantaneous eigenstates at all times, which essentially limits its application to simple and exactly solvable models like the harmonic oscillator or the Landau-Zener two-level system and the quantum Rabi model treated in Chapter 5.

Another approach that also works for more complicated systems and which is at the basis of the results presented in Chapter 4 is the so-called inverse engineering [15]. Whereas counterdiabatic driving takes the system from an initial to a final state along the adiabatic path between them, inverse-engineering works by constructing alternative paths that coincide with the adiabatic paths at its start and end points but may differ in between.

A simple illustrative example is a harmonic oscillator with time-dependent frequency, where such a path can be constructed based on the theory of Lewis-Riesenfeld invariants that were developed in 1969 to solve time-dependent Hamiltonians with the help of time-dependent invariants [128]. The Hamiltonian reads

$$\hat{H}(t) = \frac{\hat{p}^2}{2m} + \frac{1}{2}m\omega^2(t)\hat{x}^2 \quad (3.2)$$

and one can find a time-dependent invariant $\hat{I}(t)$ fulfilling the equation

$$\frac{d\hat{I}(t)}{dt} = \frac{\partial \hat{I}(t)}{\partial t} - \frac{1}{i\hbar} [\hat{H}(t), \hat{I}(t)] = 0 \quad (3.3)$$

in the form of a generalized harmonic oscillator

$$\begin{aligned} \hat{I}(t) &= \frac{\hat{\pi}^2}{2m} + \frac{1}{2}m\omega_i^2 \hat{q}^2 \\ &= a^2(t) \frac{\hat{p}^2}{2m} + \frac{1}{2}m \left(\frac{\omega_i^2}{a^2(t)} + \dot{a}^2(t) \right) \hat{x}^2 - \frac{\dot{a}(t)a(t)}{2} (\hat{x}\hat{p} + \hat{p}\hat{x}) , \end{aligned} \quad (3.4)$$

where $\hat{\pi}(t) = a(t)\hat{p} - m\dot{a}(t)\hat{x}$ is the conjugated momentum to $\hat{q}(t) = \hat{x}/a(t)$, the initial oscillator frequency is $\omega_i := \omega(t = 0)$ and the scaling factor $a(t)$ has to fulfill the Ermakov equation

$$\ddot{a} + \omega^2(t)a = \frac{\omega_i^2}{a^3}. \quad (3.5)$$

Lewis and Riesenfeld showed that a general solution of the original time-dependent Schrödinger equation is given in terms of an expansion in dynamical modes $|\psi_n(t)\rangle$ as

$$|\Psi(t)\rangle = \sum_n c_n |\psi_n(t)\rangle = \sum_n c_n e^{i\alpha_n(t)} |\phi_n(t)\rangle, \quad (3.6)$$

with time-independent constants c_n , the orthonormal eigenstates $|\phi_n(t)\rangle$ of the invariant $\hat{I}(t)$ and some phases $\alpha_n(t)$ defined as

$$\alpha_n(t) = \frac{1}{\hbar} \int_0^t dt' \langle \phi_n(t') | i\hbar \frac{\partial}{\partial t'} - \hat{H}(t') | \phi_n(t') \rangle. \quad (3.7)$$

For the time-dependent harmonic oscillator one finds

$$\begin{aligned} \psi_n(x, t) &= \langle x | \psi_n(t) \rangle \\ &= \frac{e^{-i(n+\frac{1}{2})\omega_i \int_0^t dt' \frac{1}{a^2(t')}}}{\sqrt{2^n n! a(t)}} \left(\frac{m\omega_i}{\pi\hbar} \right)^{1/4} e^{i\frac{m\dot{a}(t)}{2\hbar a(t)} x^2} e^{-\frac{m\omega_i x^2}{2\hbar}} H_n \left(\sqrt{\frac{m\omega_i}{\hbar}} \frac{x}{a(t)} \right) \\ &= \frac{1}{\sqrt{a(t)}} e^{i\varphi(x,t)} \psi_n^{HO} \left(\frac{x}{a(t)} \right) e^{-iE_n \tau(t)/\hbar}, \end{aligned} \quad (3.8)$$

with the rescaled eigenfunctions ψ_n^{HO} of a time-independent harmonic oscillator with Hermite polynomials H_n , eigenenergies $E_n = \hbar\omega_i(n + 1/2)$, evolving in a rescaled time $\tau(t) = \int_0^t dt' a^{-2}(t')$ and multiplied with a position and time-dependent phase $\varphi(x, t) = \frac{m\dot{a}(t)}{2\hbar a(t)} x^2$.

The shortcut to adiabaticity, e.g. for driving the oscillator from one frequency ω_i to another ω_f in some time T_f , can then be constructed by inverse engineering the time-dependence of $\omega(t)$. By imposing the boundary conditions

$$a(0) = 1, \quad a(T_f) = \sqrt{\frac{\omega_i}{\omega_f}} \quad \text{and} \quad \dot{a}(0) = \dot{a}(T_f) = \ddot{a}(0) = \ddot{a}(T_f) = 0 \quad (3.9)$$

one ensures that $[\hat{I}(0), \hat{H}(0)] = [\hat{I}(T_f), \hat{H}(T_f)] = 0$ and therefore that \hat{H} and \hat{I} have common eigenstates at $t = 0$ and $t = T_f$. As a result, any initial eigenstate of $\hat{H}(0)$ will evolve according to Eq. (3.6) and be identical to the corresponding eigenstate of the final trap with frequency ω_f at time T_f , apart from the phase factors $\alpha_n(T_f)$ in each mode. This means that, while \hat{H} and \hat{I} generally do not commute during intermediate times, the population levels of the final oscillator are the same as the initial ones, fulfilling the condition for an adiabatic process.

The exact form of the scaling function $a(t)$ can then be determined e.g. via a polynomial with an order high enough to fulfill the boundary conditions in Eq. (3.9)

and the driving function for $\omega(t)$ is obtained via the Ermakov equation (3.5). In this way, a shortcut to adiabaticity is constructed, which will take the harmonic oscillator from an initial frequency ω_i to a final frequency ω_f in a finite time T_f , while preserving the initial level populations, thus mimicking an adiabatic process.

Extending this approach to many-body systems or mean-field approximations like the nonlinear Gross-Pitaevskii equation is not straightforward, especially since it still requires the knowledge of an exact solution. But as I will show in the following sections, it is still possible to find exact or at least approximate shortcuts to adiabaticity in these cases by making use of a scaling ansatz similar to the solution in Eq. (3.8) for the time-dependent harmonic oscillator. Then either the Ermakov equation and the time rescaling $\tau(t)$ are modified to include the nonlinear interaction wherever possible or the Gross-Pitaevskii equation is reformulated in terms of a Lagrangian, including the phase of the wave function and the scaling factor $a(t)$ as independent variables that are determined via the Euler-Lagrange equations. A general framework for the design of shortcuts to adiabaticity in a large class of such scale-invariant systems is presented in Ref. [129].

Finally, it is important to keep in mind that, even though the shortcut duration T_f seems arbitrary, the time evolution of a quantum system cannot be sped up arbitrarily. The time-energy uncertainty relation

$$\Delta t \Delta E \gtrsim \hbar \quad (3.10)$$

gives a fundamental limit on the amount of time Δt in which the energy of a state can be changed by ΔE [130, 131]. This is known as the quantum speed limit (QSL). Considering for example an initial state $|\psi_i\rangle$ evolving according to some Hamiltonian \hat{H} with eigenenergies E_n and eigenstates $|n\rangle$, the time-dependent overlap between the initial state and its time-evolution at time t is

$$\nu(t) = \langle \psi_i | \psi(t) \rangle = \sum_n |c_n|^2 e^{-iE_n t/\hbar}, \quad (3.11)$$

with $c_n = \langle n | \psi_i \rangle$. Using trigonometric identities, it can be shown that

$$\text{Re } \nu(t) \geq 1 - \frac{2}{\pi} \frac{\langle \hat{H} \rangle}{\hbar} t + \frac{2}{\pi} \text{Im } \nu(t), \quad (3.12)$$

where $\langle \hat{H} \rangle = \sum_n |c_n|^2 E_n$ and $\text{Re } \nu$ and $\text{Im } \nu$ denote the real and imaginary part of the overlap respectively. So if we want to evolve the initial state during some time period τ to a final state that is orthogonal to it with $\nu(\tau) = 0$, then Eq. (3.12) gives the minimal amount for τ as

$$\tau \geq \tau_{QSL} = \frac{\pi}{2} \frac{\hbar}{\langle \hat{H} \rangle}. \quad (3.13)$$

A more detailed review on different expressions of this speed limit for different physical situations, including the Margolus-Levitin type limit used in the original Feshbach engine with a bright solitonic BEC working medium [132], can be found in Ref. [133]. Furthermore, contrary to the fact that the shortcut is usually designed such that the energy contributions from the driving vanish at $t = T_f$, giving the adiabatic

Hamiltonian in the end, implementing the shortcut requires a certain amount of energy beyond the truly adiabatic process, depending on its duration [134]. In other words, while shortcuts to adiabaticity based on Lewis-Riesenfeld invariants can be performed arbitrarily quickly in theory, doing so requires an infinite amount of energy as $\tau \rightarrow 0$ as a consequence of the time-energy uncertainty relation. This additional energetic cost needs to be accounted for when evaluating the performance of a heat engine making use of shortcuts.

3.2 Shortcuts in Interacting Many-Body Systems

The main focus of this thesis are interacting many-body systems for which finding shortcuts to adiabaticity is usually only possible under specific conditions. In Ref. [135] del Campo shows how to derive shortcuts for a large class of many-body systems fulfilling certain scaling laws by counterdiabatic driving. The starting point is the many-body Hamiltonian

$$\hat{H} = \sum_{i=1}^N \left[-\frac{\hbar^2}{2m} \nabla_{\mathbf{r}_i}^2 + \frac{1}{2} m \omega^2(t) \mathbf{r}_i^2 + U(\mathbf{r}_i, t) \right] + \epsilon(t) \sum_{i>j} V(\mathbf{r}_i - \mathbf{r}_j) \quad (3.14)$$

with time-dependent harmonic trapping, additional time-dependent trapping $U(\mathbf{r}_i, t)$ and a time-dependent two-body interaction $\epsilon(t)$. If the potentials fulfill

$$V(\mathbf{r}) = \lambda^\alpha V(\lambda \mathbf{r}) \quad \text{and} \quad U(\mathbf{r}, t) = \frac{1}{\gamma^2(t)} U(\sigma, 0) \quad (3.15)$$

with a rescaled position $\sigma = \mathbf{r}/\gamma(t)$ and e.g. $\alpha = d$ for the usual pseudo-potential describing s-wave scattering in a d -dimensional cold atom system, then the ansatz

$$\psi(t) = \gamma(t)^{-Nd/2} e^{-i\mu\tau(t)/\hbar} \phi(\mathbf{r}_1/\gamma(t), \dots, \mathbf{r}_N/\gamma(t); 0) \quad \text{with} \quad \frac{\partial\tau}{\partial t} = \frac{1}{\gamma^2(t)} \quad (3.16)$$

is a solution of the Hamiltonian in rescaled variables

$$\begin{aligned} \gamma^2(t) \hat{H}'_{CD} = & \sum_{i=1}^N \left[-\frac{\hbar^2}{2m} \nabla_{\sigma_i}^2 + \frac{1}{2} m \omega^2(t) \gamma^4(t) \sigma_i^2 + U(\sigma_i, 0) \right] + \frac{\epsilon(t)}{\gamma^{\alpha-2}(t)} \sum_{i>j} V(\sigma_i - \sigma_j) \\ & - i\hbar \sum_{i=1}^N \frac{\partial_\tau \gamma(t(\tau))}{2\gamma(t)} (\sigma_i \cdot \nabla_{\sigma_i} + \nabla_{\sigma_i} \cdot \sigma_i) , \end{aligned} \quad (3.17)$$

which has the form of a counterdiabatic Hamiltonian with the auxiliary term given by the expression in the second line. As a result of the scaling ansatz, this auxiliary term is proportional to $\propto (\hat{x}\hat{p} + \hat{p}\hat{x})/2$, which is the generator of scaling transformations or dilations [136]. Deffner, Jarzynski and del Campo later showed that this is generally fulfilled if the single-particle potential $U(\mathbf{r}, t)$ satisfies condition (3.15) as is the case

for a harmonic potential [129]. By choosing

$$\omega^2(t)\gamma^4(t) = \omega_i^2 \quad \text{and} \quad \epsilon(t)\gamma^{2-\alpha}(t) = 1 \quad (3.18)$$

the Hamiltonian becomes time-independent and $\phi(\sigma, 0)$ remains a stationary solution with chemical potential μ .

However, this expression is not very practical since the counterdiabatic driving term is nonlocal and it is generally not clear how such a driving term could be implemented in cold atom experiments and even implementing it numerically poses difficulties.

del Campo circumvents this problem by applying the unitary transformation $\hat{U} = \prod_{i=1}^N \exp\left(\frac{im\dot{\gamma}}{2\hbar\gamma}\mathbf{r}_i^2\right)$, which leaves the positions unaffected but transforms the momenta according to

$$\mathbf{p}_i \rightarrow \hat{U}\mathbf{p}_i\hat{U}^\dagger = \mathbf{p}_i - m\frac{\dot{\gamma}(t)}{\gamma(t)}\mathbf{r}_i, \quad (3.19)$$

which then yields a new counterdiabatic Hamiltonian

$$\begin{aligned} \hat{H}_{LCD} &= \hat{U}\hat{H}'_{CD}\hat{U}^\dagger - i\hbar\hat{U}\partial_t\hat{U}^\dagger \\ &= \sum_{i=1}^N \left[-\frac{\hbar^2}{2m}\nabla_{\mathbf{r}_i}^2 + \frac{1}{2}m\Omega^2(t)\mathbf{r}_i^2 + U(\mathbf{r}_i, t) \right] + \epsilon(t) \sum_{i>j} V(\mathbf{r}_i - \mathbf{r}_j) \end{aligned} \quad (3.20)$$

that does not contain nonlocal terms anymore and only consists of terms also appearing in the original Hamiltonian. This is also known as local counterdiabatic driving (LCD) [137]. The time-dependent harmonic trapping frequency is modified to

$$\Omega^2(t) = \omega^2(t) - \frac{\ddot{\gamma}(t)}{\gamma(t)}. \quad (3.21)$$

So by fulfilling the consistency equations (3.18) and choosing boundary conditions such that \hat{H} and \hat{H}_{LCD} as well as Ψ and ϕ are identical at initial and final times $t = \{0, T_f\}$, one can mimic an adiabatic evolution by driving the system with $\Omega(t)$ instead of $\omega(t)$.

As an example, we want to construct a shortcut to adiabaticity for tuning the interaction strength $g(t)$ from some initial value g_i to some final value g_f in some time T_f . For demonstration purposes, we consider a one-dimensional system with $\alpha = 1$. In that case the consistency equations (3.18) yield

$$g(t) = \frac{g_i}{\gamma(t)} \quad \text{and} \quad \Omega^2(t) = \frac{\omega_i^2}{g_i^4}g^4(t) + \frac{\ddot{g}(t)}{g(t)} - 2\frac{\dot{g}^2(t)}{g^2(t)} \quad (3.22)$$

for the local counterdiabatic driving. The interaction ramp $g(t)$ can be chosen arbitrarily as long as the boundary conditions

$$g(0) = g_i, \quad g(T_f) = g_f \quad \text{and} \quad \dot{g}(0) = \dot{g}(T_f) = \ddot{g}(0) = \ddot{g}(T_f) = 0 \quad (3.23)$$

are fulfilled, for example by a fifth-order polynomial $g(t) = g_i + (g_f - g_i)(10s^3 - 15s^4 + 6s^5)$ with $s = t/T_f$ in the form of a ‘*smoother step*’ function [138]. One important restriction of this protocol is that the trap frequency of the final state differs from

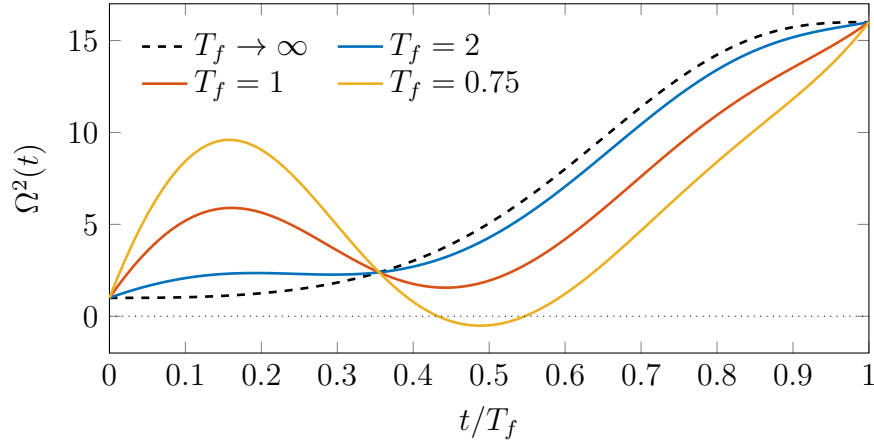


Figure 3.1: Accompanying modulation of the trapping potential according to Eq. (3.22) for a ‘*smoother step*’ interaction ramp $g(t)$ between $g_i = 1$ and $g_f = 2$. Initially $\Omega^2(0) = \omega_i^2 = 1$ and at the end $\Omega^2(T_f) = \omega_i^2(g_f/g_i)^4 = 16$. For decreasing ramp durations the harmonic trap needs to be inverted intermittently as $\Omega^2(t)$ becomes negative at times.

the initial one, ensuring the scale-invariance of the system, and is determined by the change in interaction strength according to $\omega_f^2 = \omega_i^2(g_f/g_i)^4$. Additionally, for short ramp durations the harmonic trapping potential needs to be inverted for a certain time during the ramp in order to accomplish the shortcut goal, since $\Omega^2(t)$ turns negative intermittently. This can be seen in Fig. 3.1, which shows the modulation of the trapping frequency according to Eq. (3.22) for a ‘*smoother step*’ interaction ramp and several values of T_f .

We can confirm the efficiency of the shortcut by studying the numerically tractable case of $N = 2$ particles for which we additionally know analytic expressions for the ground state wave function

$$\psi_0(x_1, x_2) = \mathcal{N}_0 \exp \left[-\frac{1}{2} (x_1^2 + x_2^2) \right] U \left(\frac{1}{4} - \frac{E_{\text{rel}}}{2}; \frac{1}{2}; \frac{1}{2} (x_1^2 - 2x_1x_2 + x_2^2) \right) \quad (3.24)$$

with normalizing constant \mathcal{N}_0 , Kummer function $U(a; b; z)$ and where E_{rel} solves

$$g_i = -2\sqrt{2} \frac{\Gamma \left(-\frac{E_{\text{rel}}}{2} + \frac{3}{4} \right)}{\Gamma \left(-\frac{E_{\text{rel}}}{2} + \frac{1}{4} \right)} \quad (3.25)$$

as introduced in Section 2.3 and where again all quantities are expressed in dimensionless harmonic oscillator units for a frequency ω_i . The ground state energy is given by

$$E_0(\omega_i, g_i) = E_{\text{rel}} + \frac{1}{2}. \quad (3.26)$$

The energy and the wave function of the ground state with final trap frequency ω_f and interaction g_f in the original dimensionless units for a trap frequency ω_i can be

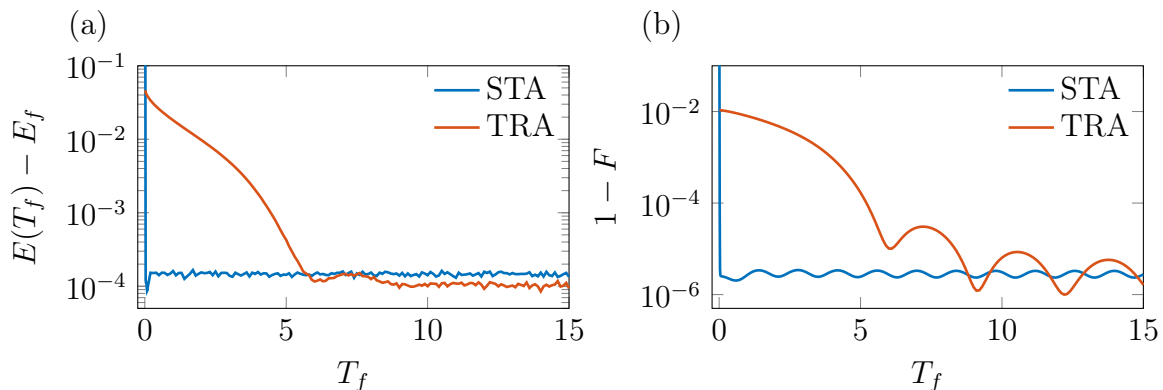


Figure 3.2: (a) Difference in energy to the target state after driving the interaction strength of two harmonically trapped bosons in 1D from $g_i = 1$ to $g_f = 2$ in time T_f both via a shortcut to adiabaticity (STA) and a time-rescaled adiabatic reference (TRA) ramp without the local counterdiabatic modulation of the trapping frequency. (b) The infidelity $1 - |\langle \psi(T_f) | \psi_f \rangle|^2$ after the same interaction ramps. The shortcut breaks down around $T_f \sim 0.01$ when the required modulations of the potentials become too large for the employed numerics. See text for details.

conveniently obtained from the initial ones via

$$E_f = E_0(\omega_f, g_f) = \frac{g_f^2}{g_i^2} E_0(\omega_i, g_i) \quad \text{and} \quad (3.27)$$

$$\psi_f(x_1, x_2) = \psi_0(\omega_f, g_f, x_1, x_2) = \sqrt{\frac{g_f}{g_i}} \psi_0\left(\omega_i, g_i, \frac{g_i}{g_f} x_1, \frac{g_i}{g_f} x_2\right)$$

due to the relation $(\omega_f/\omega_i)^2 = (g_f/g_i)^4$ mentioned above.

Figure 3.2 shows (a) the difference in energy $E(T_f) - E_f$ and (b) the discrepancy between the final state and target state quantified by the infidelity $1 - |\langle \psi(T_f) | \psi_f \rangle|^2$ after ramping the interaction strength in the two-particle system from $g_i = 1$ to $g_f = 2$ as a function of ramp time T_f , both for the shortcut to adiabaticity (STA) using the time-varying local counterdiabatic trapping frequency $\Omega(t)$ as well as for a time-rescaled adiabatic reference ramp (TRA). The reference ramp is a pure interaction ramp of equal duration and using the same smooth function, but without the trap modulation, i.e. how one might try to control the system without the shortcut. Note that E_f and $|\psi_f\rangle$ are different in both cases due to Eq. (3.18) affecting the final trap frequency. For both ramps the ‘*smoother step*’ function mentioned above was used.

The shortcut works as intended, reaching very small values for both the energy difference and infidelity independent of ramp duration, limited only by the chosen numerical accuracy. However, below ramp times of around $T_f \sim 0.01$ the shortcut breaks down in our case since the required modulations of the trapping potential become too large in magnitude compared to the chosen time step in the employed numerics. For the time-rescaled adiabatic reference, we need to choose ramp times longer than at least one or two trap oscillations in order to consistently see comparably small levels

of energy difference and infidelity. The modulations seen in the infidelity are a result of the underlying harmonic trap and nicely reflect the factor of $\omega_f = (g_f/g_i)^2\omega_i = 4\omega_i$ in the rescaled final trapping frequency for the STA case.

3.3 Coherent Control of Bose-Einstein Condensates

In general, controlling a system like a Bose-Einstein condensate via the external potential or the interparticle interaction strength will lead to changing length- and/or timescales [139, 140] which have already been observed experimentally [126, 127]. As we have seen in the previous section, it is possible to construct an exact shortcut to adiabaticity based on such scaling properties for changing the interaction strength of a quantum many-body system. This comes at the cost of having to simultaneously modulate the trapping frequency.

In this section I will introduce two approaches that accomplish the same on a mean-field level for Bose-Einstein condensates in different interaction regimes purely by tuning the interaction strength without the need for additional control fields. The first approach is a variational ansatz used by Li et al. in Ref. [132] for a one-dimensional bright solitonic BEC. I extend this approach to higher dimensional bright solitons which are in general not stable in free space [141], although, for example, in 2D they can be stabilized by changing the interaction strength in an STA-like fashion [142]. If an additional harmonic trapping potential is present, like in most BEC experiments, (meta)-stable bright solitons can exist as long as the particle number and interaction strength do not exceed certain thresholds. The second approach is based on the scaling ansatz that we have encountered in the previous section and which allowed me to derive an exact interaction shortcut for BECs in the experimentally common Thomas-Fermi regime that is at the basis of the publication in Chapter 4.

3.3.1 Attractive Interactions: Bright Solitons

We consider a one-dimensional Bose-Einstein condensate confined to a harmonic trap with frequency ω and described via the Gross-Pitaevskii equation

$$i\hbar\frac{\partial\psi}{\partial t} = \left(-\frac{\hbar^2}{2m}\frac{\partial^2}{\partial x^2} + \frac{1}{2}m\omega^2x^2 + g(t)|\psi|^2\right)\psi, \quad (3.28)$$

with the condensate wave function ψ , atomic mass m and time-dependent attractive interatomic interaction strength $g(t) < 0$. In the absence of the harmonic trapping potential, the GPE has an exact solution in the form of a bright soliton wave function $\psi = \sqrt{\frac{N^2|g|m}{4\hbar^2}}\text{sech}\left(\frac{Nm|g|x}{2\hbar^2}\right)$, which is normalized to the number of particles N in the condensate [27]. In order to portray an experimentally more realistic situation, the authors in Ref. [132] assume a regime in which the trapping potential is present but weak and that the bright soliton wave function is still a good approximation to the true ground state of the system.

The shortcut to adiabaticity is then constructed by first choosing a suitable trial function ψ for the variational ansatz, given by the hyperbolic secant

$$\psi(x, t) = A(t) \operatorname{sech} \left(\frac{x}{a(t)} \right) e^{ib(t)x^2}, \quad (3.29)$$

with soliton width $a(t)$ and a chirp $b(t)$, allowing the wave function to change shape during the ramp [143, 144] and subsequently calculating the Lagrangian density

$$\mathcal{L} = \frac{i\hbar}{2} \left(\psi^* \frac{\partial \psi}{\partial t} - \psi \frac{\partial \psi^*}{\partial t} \right) - \frac{\hbar^2}{2m} |\partial_x \psi|^2 - V(x) |\psi|^2 - \frac{g(t)}{2} |\psi|^4, \quad (3.30)$$

similarly to Ref. [145]. For simplicity, I present the procedure only for the one-dimensional case but give the results for two and three dimensions at the corresponding points. They are obtained from an analogous calculation assuming an isotropic system in 2D and 3D respectively. If we require the wave function to be normalized to the number of particles in the condensate N , the amplitude $A(t)$ is fixed to $\sqrt{N/2a(t)}$, $\sqrt{N/2\pi a^2(t) \ln(2)}$ and $\sqrt{3N/\pi^3 a^3(t)}$ in 1D, 2D and 3D respectively.

In the following we switch to dimensionless units, displaying energies in multiples of $\hbar\omega$, time in multiples of ω^{-1} and lengths in multiples of $x_0 = \sqrt{\hbar/m\omega}$, meaning the interaction strength is given in units of $\hbar\omega x_0^d$ in d dimensions. Using the ansatz from Eq. (3.29), the Lagrangian $L = \int d\mathbf{r} \mathcal{L}$ is calculated and the soliton width $a(t)$ and the chirp $b(t)$ are determined via the Euler-Lagrange equations

$$\frac{d}{dt} \frac{\partial L}{\partial \dot{q}_i} - \frac{\partial L}{\partial q_i} = 0, \quad (3.31)$$

with $q_i = \{a, b\}$. Independent of the system dimension, the shape of the phase chirp $b(t)$ is given by

$$\dot{a} = 2ab, \quad (3.32)$$

which in combination with the x^2 term in the ansatz is identical to the unitary transformation in Section 3.2 for obtaining a local version of the nonlocal counterdiabatic term. Combining this with the equation for \dot{b} gives us the equations of motion (EOM) for the soliton width

$$1\text{D} : \quad \ddot{a}(t) + a(t) = \frac{4}{\pi^2 a^3(t)} + \frac{2Ng(t)}{\pi^2 a^2(t)} \quad (3.33a)$$

$$2\text{D} : \quad \ddot{a}(t) + a(t) = \left(\frac{4(1 + \ln(4))}{27\zeta(3)} + Ng(t) \frac{2(\ln(16) - 1)}{27\pi \ln(2)\zeta(3)} \right) \frac{1}{a^3} \quad (3.33b)$$

$$3\text{D} : \quad \ddot{a}(t) + a(t) = \frac{20(\pi^2 + 12)}{21\pi^4} \frac{1}{a^3} + \frac{60(\pi^2 - 6)}{7\pi^7} \frac{Ng(t)}{a^4}, \quad (3.33c)$$

where $\zeta(s)$ is the Riemann zeta function. In general, there is no analytical solution to these equations, although in 2D the equation of motion has the form of an Ermakov equation, which has an analytical solution for constant $g(t)$ [146]. Similarly to the previous section, the shortcut to adiabaticity is inverse-engineered by solving the EOM

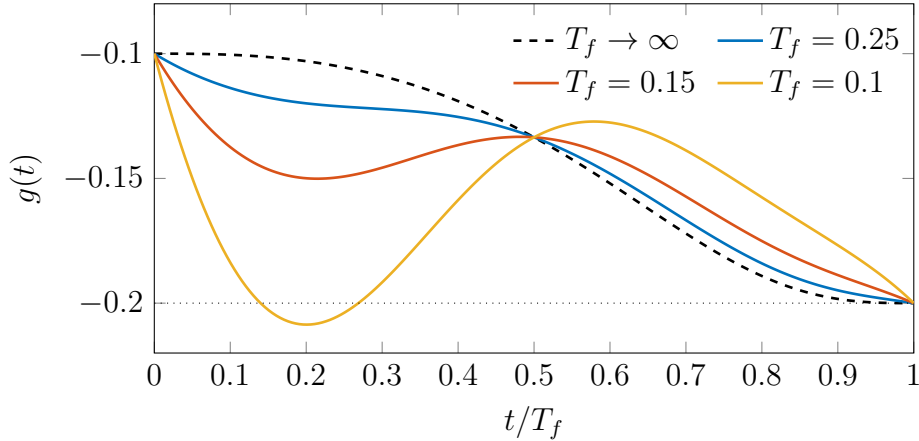


Figure 3.3: Shortcut to adiabaticity for ramping the interaction in a 1D bright soliton consisting of $N = 100$ atoms from $g_i = -0.1$ to $g_f = -0.2$ in a time T_f according to $g(t) = \frac{\pi^2 a^2(t)}{2N} [\ddot{a}(t) + a(t) - \frac{4}{\pi^2} \frac{1}{a^3(t)}]$, inverse engineered from Eq. (3.33a) and where $a(t)$ is a ‘*smoother step*’ function.

in Eqs. (3.33) for $g(t)$ and choosing an arbitrary function $a(t)$ fulfilling the boundary conditions

$$a(0) = a_i, \quad a(T_f) = a_f \quad \text{and} \quad \dot{a}(0) = \dot{a}(T_f) = \ddot{a}(0) = \ddot{a}(T_f) = 0, \quad (3.34)$$

e.g. again by the ‘*smoother step*’ function $a(t) = a_i + (a_f - a_i)(10s^3 - 15s^4 + 6s^5)$ with $s = t/T_f$ and where except for the 2D case a_i and a_f need to be determined numerically from $g(0) = g_i$ and $g(T_f) = g_f$. Figure 3.3 shows exemplary ramps for the 1D case. For fast ramps, the shortcut requires to increase the interaction beyond the initial and final values (see $T_f = 0.1$ curve). The ramps for the 2D and 3D cases are qualitatively similar, but this behavior might lead to a collapse of the bright soliton if their respective limits of stability, discussed in the following, are crossed.

In contrast to the one-dimensional case, there is a limit to the size respectively interaction strength of the bright soliton in order to ensure its stability in 2D and 3D [141]. Calculating its energy using the ansatz wave functions in Eq. (3.29) and integrating the energy density

$$E = \int_{-\infty}^{\infty} dx \left[\frac{1}{2} \left| \frac{\partial \psi}{\partial x} \right|^2 + \frac{1}{2} x^2 |\psi|^2 + \frac{g}{2} |\psi|^4 \right], \quad (3.35)$$

leads to the expressions

$$\text{1D:} \quad E = N \left[\frac{1}{6} \frac{1}{a^2} + \frac{\pi^2}{24} a^2 + \frac{1}{6} \frac{Ng}{a} \right] \quad (3.36a)$$

$$\text{2D:} \quad E = N \left[\frac{1 + \ln(4)}{12 \ln(2)} \frac{1}{a^2} + \frac{9\zeta(3)}{16 \ln(2)} a^2 + \frac{\ln(16) - 1}{24\pi \ln^2(2)} \frac{Ng}{a^2} \right] \quad (3.36b)$$

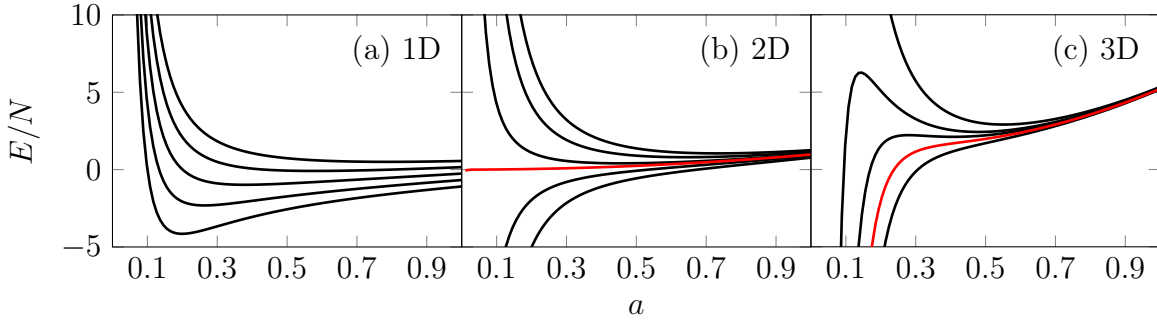


Figure 3.4: Bright soliton energy in 1D, 2D and 3D according to Eqs. (3.36) for different values of Ng between $Ng = -10$ (lowest line) and -0.1 (highest line) as a function of the soliton width a . The 2D and 3D plot include the graph for the respective $(Ng)_{\max}$ value in Eq. (3.37) below which there is no more stable minimum for the soliton width (red lines).

$$\text{3D : } E = N \left[\frac{\pi^2 + 12}{6\pi^2} \frac{1}{a^2} + \frac{\pi}{2} a^2 + \frac{\pi^2 - 6}{\pi^5} \frac{Ng}{a^3} \right] \quad (3.36c)$$

for the energies as a function of the soliton width. Since we are considering attractive interactions $g < 0$, this results in a condition for the product Ng in 2D and 3D to ensure the existence of the extrema and therefore the stability of the bright soliton.

Fig. 3.4 shows a plot of the soliton energy in different dimensions as a function of its width for different values of Ng . The graphs for the two- and three-dimensional case include the respective value $(Ng)_{\max}$ at which the soliton becomes unstable. They are given by

$$|(Ng)_{\max}|^{2D} = 2\pi \ln(2) \frac{\ln(4) + 1}{\ln(16) - 1} \approx 5.86 \quad \text{and} \quad |(Ng)_{\max}|^{3D} \approx 7.25, \quad (3.37)$$

where the 3D value was determined numerically.

Evaluations of the shortcut efficiency in the one-dimensional case can be found in Ref. [132]. There it is mainly used to boost the efficiency of a so-called Feshbach heat engine, which will be the topic of Chapter 4. It is important to note that this type of shortcut based on a variational principle is only approximate and yields greatly improved but not perfect results for the target energy and fidelity which also depend on the ramp duration in contrast to the exact shortcut in the previous section.

3.3.2 Repulsive Interactions: Thomas-Fermi Regime

The bright solitons studied in the previous part are prone to collapse due to their attractive interactions. Therefore, in the final part of this chapter I will now derive the exact shortcut to adiabaticity for interaction ramps of a Bose-Einstein condensate in the Thomas-Fermi regime of large system sizes and strong repulsive interactions introduced in Section 1.4, which is at the basis of the publication in the following

Chapter 4. The starting point is again the Gross-Pitaevskii equation

$$i\hbar \frac{\partial \psi}{\partial t} = \left(-\frac{\hbar^2}{2m} \frac{\partial^2}{\partial x^2} + \frac{1}{2} m \omega^2 x^2 + g(t) |\psi|^2 \right) \psi \quad (3.38)$$

of a one-dimensional Bose-Einstein condensate in a harmonic trapping potential. Based on our experience in the previous sections, we are again interested in scaling solutions in the form of

$$\psi(x, t) = \frac{1}{\sqrt{a(t)}} e^{i\varphi(x, t)} \phi(y(x, t), \tau(t)), \quad (3.39)$$

with some rescaled coordinate $y(x, t) = x/a(t)$ and a yet to be determined rescaled time $\tau(t)$. Inserting this ansatz into the Gross-Pitaevskii equation (3.38) yields

$$\begin{aligned} i\hbar \frac{\partial \phi}{\partial \tau} \frac{\partial \tau}{\partial t} = & \left[-\frac{\hbar^2}{2m} \frac{1}{a^2} \frac{\partial^2}{\partial y^2} + \frac{1}{2} m \omega^2 x^2 + \frac{g}{a} |\phi|^2 \right] \phi + \left[i\hbar \frac{\dot{a}}{a^2} x - \frac{i\hbar^2}{m} \frac{1}{a} \frac{\partial \varphi}{\partial x} \right] \frac{\partial \phi}{\partial y} \\ & + \left[\frac{i\hbar \dot{a}}{2a} + \hbar \dot{\varphi} - \frac{i\hbar^2}{2m} \frac{\partial^2 \varphi}{\partial x^2} + \frac{\hbar^2}{2m} \left(\frac{\partial \varphi}{\partial x} \right)^2 \right] \phi. \end{aligned} \quad (3.40)$$

By choosing the phase just like in previous examples of scale-invariant systems according to

$$\varphi(x, t) = \frac{m \dot{a}(t)}{2\hbar a(t)} x^2, \quad (3.41)$$

we can eliminate the term proportional to $\partial \phi / \partial y$. It can be interpreted physically as a gauge transformation $\hat{U} = e^{i\varphi(x, t)}$ which subtracts the momentum of the expanding or shrinking system according to

$$\hat{p} \rightarrow \hat{U} \hat{p} \hat{U}^\dagger = \hat{p} - m \frac{\dot{a}}{a} \hat{x}, \quad (3.42)$$

where $\dot{a}x/a$ is the local velocity in the system. This leads to a modified Gross-Pitaevskii equation in the rescaled coordinates

$$i\hbar \frac{\partial \phi}{\partial \tau} \frac{\partial \tau}{\partial t} = \left[-\frac{\hbar^2}{2m} \frac{1}{a^2} \frac{\partial^2}{\partial y^2} + \frac{1}{2} m (\ddot{a} + \omega^2 a) a y^2 + \frac{g}{a} |\phi|^2 \right] \phi. \quad (3.43)$$

Choosing the rescaled time τ and the term $\ddot{a} + \omega^2 a$ in such a way that it leads to a solvable Gross-Pitaevskii equation allows one to design control pulses for a frictionless evolution of the BEC, e.g. under varying the trap frequency ω [147, 148].

Many experiments involving Bose-Einstein condensates are carried out in a regime of repulsive interaction and high particle numbers, which fulfills the condition $Ng \gg \hbar \omega x_0^d$, meaning that the potential energy and the interaction energy are much larger than the kinetic energy [40]. Neglecting the kinetic energy term in the Gross-Pitaevskii equation in this so-called Thomas-Fermi (TF) limit allows to obtain an analytical solution in the form

$$\psi(x, t) = \sqrt{\frac{1}{g} (\mu - V(x))} e^{-i\mu t/\hbar} \quad \text{for} \quad \mu > V(x) \quad (3.44)$$

and $\psi(x, t) \equiv 0$ otherwise, where the chemical potential μ is determined via the normalization condition. Considering the TF limit and neglecting the kinetic energy term in the scaling GPE Eq. (3.43) and choosing scaling functions according to [149]

$$\ddot{a} + \omega^2 a = \omega^2 \frac{g(t)}{g_i} \frac{1}{a^2} \quad \text{and} \quad \tau = \int_0^t dt' \frac{g(t')}{g_i a(t')}, \quad (3.45)$$

with some initial interaction strength g_i , leaves us with

$$i\hbar \frac{\partial \phi}{\partial \tau} = \left[\frac{1}{2} m \omega^2 y^2 + g_i |\phi|^2 \right] \phi, \quad (3.46)$$

which has the aforementioned Thomas-Fermi solution

$$\phi(y, \tau) = e^{-i\mu_i \tau / \hbar} \sqrt{\frac{1}{g_i} \left(\mu_i - \frac{1}{2} m \omega^2 y^2 \right)} \quad \text{with} \quad \mu_i = \left(\frac{9}{32} m \omega^2 N^2 g_i^2 \right)^{1/3}. \quad (3.47)$$

Inserting this back into the scaling ansatz gives us an analytic expression for the time evolution of the wave function

$$\psi(x, t) = \frac{1}{\sqrt{a(t)}} e^{i \frac{m}{2\hbar} \frac{\dot{a}(t)}{a(t)} x^2} e^{-i \frac{\mu_i}{\hbar} \int_0^t dt' \frac{g(t')}{g_i a(t')}} \sqrt{\frac{1}{g_i} \left(\mu_i - \frac{1}{2} m \omega^2 \frac{x^2}{a^2(t)} \right)}. \quad (3.48)$$

So by changing the interaction strength according to

$$g(t) = g_i \frac{a^2(t)}{\omega^2} (\ddot{a}(t) + \omega^2 a(t)) \quad (3.49)$$

and requiring

$$a(0) = 1, \quad a(T_f) = \left(\frac{g_f}{g_i} \right)^{1/3} \quad \text{and} \quad \dot{a}(0) = \dot{a}(T_f) = \ddot{a}(0) = \ddot{a}(T_f) = 0, \quad (3.50)$$

we can drive the system from an initial interaction strength g_i to a final value g_f in an almost arbitrarily short time T_f while mimicking an adiabatic evolution. Similarly to the previous examples, the scaling factor $a(t)$ can be determined by choosing a polynomial ansatz of sufficient order according to the conditions in Eq. (3.50). The final state after this shortcut, apart from an irrelevant phase depending on the duration T_f , perfectly coincides with the state after an adiabatic evolution.

Analogous calculations for a d -dimensional BEC in an isotropic harmonic trap in the Thomas-Fermi limit allow to generalize the shortcut ramp which then stipulates a driving of the interaction strength according to

$$g(t) = g_i \frac{a^{d+1}(t)}{\omega^2} (\ddot{a}(t) + \omega^2 a(t)) , \quad (3.51)$$

while requiring $a(T_f) = (g_f/g_i)^{1/(d+2)}$. Additionally, in the time scaling τ in Eq. (3.45) the term $g_i a(t')$ needs to be replaced with $g_i a^d(t')$.

The performance of the shortcut is evaluated in Publication [1], where it is used to boost the performance of a Feshbach engine (see the following chapter). It is an exact shortcut but only within the Thomas-Fermi approximation, which means that similarly to the variational shortcut for bright solitons there are finite energy differences and infidelities after the ramp, stemming from the deviations of the BEC wave function from the Thomas-Fermi approximation, particularly around the condensate edges. Another point to note is that the system exhibits an intrinsic quantum speed limit in the form of a modulational instability that occurs for ultrashort ramp durations, where the shortcut requires to drive the system at attractive interactions intermittently. This is not obvious from the exact solution and in Publication [1] I derive an analytic expression for the minimum shortcut time.

Finally, even in the general case, where we cannot neglect the kinetic energy contribution, it is still possible to transform the scaling ansatz into a time-independent Gross-Pitaevskii equation. To this end, we choose

$$\ddot{a} + \omega^2(t)a = \frac{\omega_i^2}{a^3}, \quad \tau = \int_0^t dt' \frac{1}{a^2(t')} \quad \text{and} \quad g(t) = \frac{g_i}{a(t)}, \quad (3.52)$$

which leads to

$$i\hbar \frac{\partial \phi}{\partial \tau} = \left[-\frac{\hbar^2}{2m} \frac{\partial^2}{\partial y^2} + \frac{1}{2} m \omega_i^2 y^2 + g_i |\phi|^2 \right] \phi, \quad (3.53)$$

where we have assumed a time-dependent trap frequency $\omega(t)$ for the original system. Therefore, the solution to the original GPE is given by

$$\psi(x, t) = \frac{1}{\sqrt{a(t)}} e^{i \frac{m}{2\hbar} \frac{\dot{a}(t)}{a(t)} x^2} e^{-i \frac{\mu_i}{\hbar} \int_0^t dt' \frac{1}{a^2(t')}} \phi_i \left(\frac{x}{a(t)} \right), \quad (3.54)$$

where $\phi_i(x/a(t))$ is a solution to the rescaled GPE (3.53) with chemical potential μ_i . The additional third condition, needed to transform the rescaled GPE into a time-independent one, means that we cannot drive the system anymore just by changing the interaction strength alone, but that we need to assume a time-dependent trapping potential $\omega(t)$ as well [149], similarly to the exact many-body shortcut in Section 3.2.

Chapter 4

Feshbach engine in the Thomas-Fermi regime (Publication [1])

This chapter is based on the publication of the same name and presents its context, a connection to experimentally relevant parameter regimes and prospects for future work.

4.1 Introduction

Nearly two hundred years ago Sadi Carnot's work laid the foundations of modern thermodynamics and gave the first general description of a heat engine in the form of the Carnot cycle, connecting the concepts of heat and work [150]. Although steam engines had been powering the industrial revolution even fifty years before that, only this idealized description of a heat engine gave the necessary control to increase their efficiency reliably. In 1959 Schulz-DuBois and Scovil realized that the gain medium of a maser, which is typically described as a three level system pumped via an external source to create a population inversion, can also be viewed as a heat engine [151]. This was the first description of a heat engine whose working medium made use of the purely quantum mechanical property of discrete energy levels in contrast to the continuous energy spectrum of a classical working medium and therefore gave rise to the concept of quantum heat engines.

The temperatures T_h and T_c ($T_h > T_c$) of the hot and cold heat baths limit the efficiency of both classical and quantum heat engines according to the standard Carnot bound $\eta_{\text{Carnot}} = 1 - T_c/T_h$, as long as thermodynamic reversibility is ensured and the working medium is always in an equilibrium state [152]. For quantum heat engines, this was only proven rigorously recently in Ref. [153]. In 2003 Scully et al. proposed a quantum Carnot engine with an efficiency surpassing this bound by using atoms for the heat bath at high temperature that possess a certain degree of coherence, i.e. atoms whose wave functions have a fixed phase relation [154]. This surplus of efficiency means that even in the case $T_c \rightarrow T_h$, where $\eta_{\text{Carnot}} \rightarrow 0$, work can be extracted from two heat baths at the same temperature or essentially from a single heat bath. However, the second law of thermodynamics is not violated since work has to be provided in order to prepare the coherent heat bath.

Since then, many works extended the idea of extracting work from quantum effects, like quantum correlations [155], in order to demonstrate a supremacy of quantum heat engines over classical ones, e.g. by surpassing the Carnot bound. While work can also be extracted from a quantum mechanical measurement process, without the need for any heat bath [156], most of them suggest the use of specifically engineered, non-thermal heat baths [157–161], for example by using squeezed states [162]. Klaers et al. were able to achieve such a heat engine surpassing the Carnot bound experimentally with an oscillating nanobeam coupled to squeezed thermal noise [163]. Quantum supremacy due to a coherent working medium, but using standard thermal baths, was demonstrated recently with nitrogen vacancy centers in diamond [164]. Other possibilities of achieving quantum supremacy include the exploitation of the quantum nature of a many-particle working medium and its intrinsic interactions [165–167] or operating the engine for many cycles [168].

The concept of the Feshbach engine, which is the topic of this chapter, was introduced in Ref. [132]. There, Li et al. proposed an Otto-like engine cycle in which a one-dimensional Bose-Einstein condensate with attractive nonlinear interactions is used as the working medium. Work is performed by compressing and expanding the BEC via modulating the nonlinear interaction strength e.g. via Feshbach resonances (see Section 1.2), hence the name, and the authors showed how the engine performance can be boosted by using shortcuts to adiabaticity and by increasing the nonlinear interaction strength. Both the original Feshbach engine and its extension presented here consider BECs described by Gross-Pitaevskii equations on the mean-field level. Therefore, any coherence or correlations, which are possibly present in the system as a consequence of its quantum nature and which could lead to quantum supremacy in its performance, are neglected. The focus is purely on enabling high fidelity quantum control for an intricate process. Nonetheless, the Feshbach engine is conceptually interesting for the still young and growing field of quantum thermodynamics. Also especially because the BECs are considered at zero temperature, meaning that the heat baths of an ordinary engine cycle are replaced by another resource, namely particle baths.

In this chapter I extend the concept of the Feshbach engine to the Thomas-Fermi regime of large, repulsively interacting condensates that are commonly produced in experiments (see Section 1.4). After a brief introduction to quantum thermodynamics and the working principle of the Feshbach engine, I show in Publication [1] how the shortcut to adiabaticity derived in the previous chapter is able to boost the engine performance. The control pulse for the interaction strength can take on attractive values intermittently if the pulse length is short or the change in interaction strength is large. We find that if the duration or strength of this attractive part is large enough, it can lead to a modulational instability of the condensate [169], rendering the shortcut useless.

Experimentalists have taken advantage of this instability by successfully creating trains of bright solitons, forming as a result of suddenly quenching the interaction strength in a BEC from the repulsive to the attractive regime [170–172]. This prompted many theoretical investigations on the exact mechanisms behind the modulational instability and the soliton formation in different situations, see for example references [173, 174], and how to apply it to create a pulsed atomic soliton laser [175]. In a similar setting for the manipulation of Bose-Einstein condensates in the Thomas-Fermi regime

via the external trap, optimal control theory was used to show that ‘bang-bang’ protocols of sudden quenches between piece-wise constant trap frequencies provide the fastest possible shortcut to adiabaticity in this case, while adhering to predefined constraints on allowed trap frequencies [148].

In a related fashion I perform a stability analysis to derive an analytical expression for a lower bound on the cycle duration for given condensate parameters, similar to a quantum speed limit. The chapter concludes with some considerations regarding experimental requirements for a realization of the Feshbach engine and the shortcut strokes as well as considerations about future work regarding an implementation of the isochoric strokes and extracting useful work from the engine.

4.2 Quantum Thermodynamics and Feshbach Engines

Thermodynamics usually deals with quasi-static processes in which the system can be considered to be in internal equilibrium at all times. If additionally no entropy is produced during the process, it is called reversible. In other words, it deals with the change in energy of a working medium like the ideal gas by means of external manipulation. In the framework of thermodynamics, these energy flows can be classified into two categories, namely heat and work [152]. Heat Q is defined as the energy that spontaneously flows from one object to another as a consequence of a temperature difference between these objects. Any other transfer of energy to or from the system which involves for example an agent like a mechanical piston actively changing the energy of the system, is classified as work W . The conservation of energy can then be expressed as the first law of thermodynamics $\Delta U = Q + W$. The change in total energy U equals the heat added plus the work done.

In order to define these thermodynamic quantities for a quantum system, let us consider an arbitrary system with discrete energy levels E_n and corresponding eigenstates $|n\rangle$ in thermal equilibrium at some finite temperature T . Its Hamiltonian can be written as $H = \sum_n E_n |n\rangle \langle n|$ and the internal energy U of the system is given by $U = \langle H \rangle = \sum_n p_n E_n$. The occupation probabilities p_i are determined via the Boltzmann distribution [176] $p_i = \frac{e^{-\beta E_i}}{\sum_n e^{-\beta E_n}}$ with the partition function $Z = \sum_n e^{-\beta E_n}$ and where $\beta^{-1} = k_B T$ with the Boltzmann constant k_B . A change in the internal energy can therefore be written as

$$dU = \sum_n p_n dE_n + \sum_n E_n dp_n. \quad (4.1)$$

We know from classical thermodynamics that $\delta Q = TdS$. At the same time, the entropy of the system can be calculated via $S = -k_B \sum_n p_n \log p_n$ [177]. We can therefore make the connection

$$\begin{aligned} \delta Q = TdS &= -k_B T \sum_n (\log p_n + 1) dp_n = -k_B T \sum_n (-\beta E_n - \log Z + 1) dp_n \\ &= \sum_n E_n dp_n + k_B T (\log Z - 1) \sum_n dp_n = \sum_n E_n dp_n, \end{aligned} \quad (4.2)$$

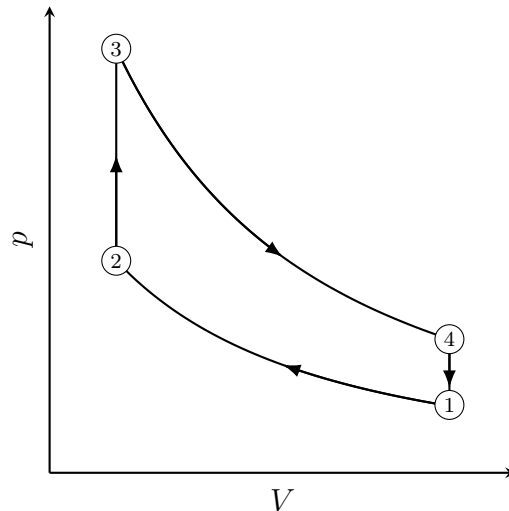


Figure 4.1: Classical Otto cycle displayed in the pressure-volume plane. It consists of an adiabatic compression (1) \rightarrow (2), an isochoric heating (2) \rightarrow (3), an adiabatic expansion (3) \rightarrow (4), and an isochoric cooling (4) \rightarrow (1).

since the condition $\sum_n p_n = 1$ at all times requires $\sum_n dp_n = 0$. Therefore, a quantum version of the first law of thermodynamics $dU = \delta Q + \delta W$ can be established by identifying [8]

$$\delta Q = \sum_n E_n dp_n \quad \text{and} \quad \delta W = \sum_n p_n dE_n. \quad (4.3)$$

An adiabatic process $\delta Q = 0$ is one that leaves the occupation probabilities p_n of a system unchanged, and therefore also its entropy S , while a change in its eigenenergies results in work being performed on or by the system.

The Feshbach engine uses an engine cycle reminiscent of a classical Otto cycle, which is the working principle of most modern combustion engines. Let us therefore first briefly recall its main characteristics. Assuming an ideal gas as the working medium, the classical Otto cycle is displayed in Fig. 4.1. The ideal gas consists of N point-like, non-interacting particles enclosed in a volume V at some temperature T which exerts a pressure p on the container walls. The equation of state is the ideal gas law $pV = Nk_B T$ [176]. The cycle consists of

1. an adiabatic compression from volume V_1 to volume V_2 , increasing the temperature from T_1 to T_2 .
2. an isochoric heating from T_2 to T_3 at constant volume of V_2 .
3. an adiabatic expansion from volume V_2 back to volume V_1 , while decreasing the temperature from T_3 to T_4 .
4. an isochoric cooling from temperature T_4 back to T_1 at a constant volume of V_1 .

The efficiency of the Otto cycle can be computed as [152]

$$\eta_{\text{Otto}} = 1 - \left(\frac{V_2}{V_1} \right)^{\gamma-1} = 1 - \frac{T_1}{T_2} = 1 - \frac{T_4}{T_3}, \quad (4.4)$$

where the adiabatic exponent $\gamma = (f + 2)/f$ depends on the degrees of freedom f of the working medium constituents, e.g. $f = 3$ for a monatomic gas. In order to increase the efficiency of the Otto engine, one needs to increase the compression ratio V_1/V_2 . It is also apparent that $\eta_{\text{Otto}} < \eta_{\text{Carnot}}$, since the ratios T_1/T_2 and T_4/T_3 are larger than the minimal ratio T_1/T_3 that would appear in the corresponding Carnot efficiency.

According to Eq. (4.3), we need to change the energy of the system in order to perform work. In analogy with the compression and expansion strokes in a classical Otto cycle, this is accomplished by changing the interaction strength g in the Feshbach engine, which also results in a compressed or expanded wave function of the quantum system. Finally, we need to close the engine cycle by fixing the interaction strength and varying the remaining parameter, which is the number of particles N since we are dealing with a system at zero temperature as mentioned in the introduction.

In a classical Otto cycle these would correspond to isochoric heating and cooling strokes putting the working medium into contact with two finite-temperature heat baths. For the Feshbach engine, we need to have ‘particle baths’ with the ability to add or remove atoms from the condensate assuming the role of the classical heat baths. However, recalling from Part I of this thesis that the condensate fraction and therefore the particle number N depends on the temperature of the non-condensed part of the atomic gas, the connection with the classical Otto cycle is restored. So even though the working medium itself is considered at $T = 0$, temperature indirectly plays a role via the surrounding thermal cloud.

Nonetheless, the Feshbach engine can also be operated entirely at $T = 0$ if the particle exchange is realized via a chemical potential gradient between the working medium and another condensate also at zero temperature acting as a reservoir for example. On the other hand, if either finite temperature or finite correlation effects are included in the working medium description as well, the engine performance is expected to decrease compared to the zero temperature, mean-field results derived in the following.

From the previous section we know that the Gross-Pitaevskii equation in free space has a stable, self-focusing bright soliton solution in one dimension [27]. In the presence of a harmonic trap, its energy is modified to the expression given in Eq. (3.36a) as a function of soliton width a . For the Feshbach engine in Ref. [132], the authors assume that the soliton width is still approximately given by the free space value $a = 2/N|g|$ so that the system energy in harmonic oscillator units reads

$$E(N, g) = \frac{\pi^2}{6} \frac{1}{N|g|^2} - \frac{N^3|g|^2}{24}. \quad (4.5)$$

Figure 4.2 (a) shows a schematic Feshbach engine cycle for a bright solitonic working medium based on Eq. (4.5). After an adiabatic compression by increasing the modulus of the attractive interaction from $|g_i|$ to $|g_f|$ performs some work $\langle W_C \rangle = E(N_i, g_f) - E(N_i, g_i)$, ‘heat’ $\langle Q_{N_-} \rangle = E(N_f, g_f) - E(N_i, g_f)$ is added to the system by decreasing the particle number from N_i to N_f . By providing some work $\langle W_E \rangle = E(N_f, g_i) - E(N_i, g_f)$ the wave function is expanded again to the initial interaction strength before some ‘heat’ $\langle Q_{N_+} \rangle = E(N_i, g_i) - E(N_f, g_i)$ is dissipated by increasing the particle number back to N_i .

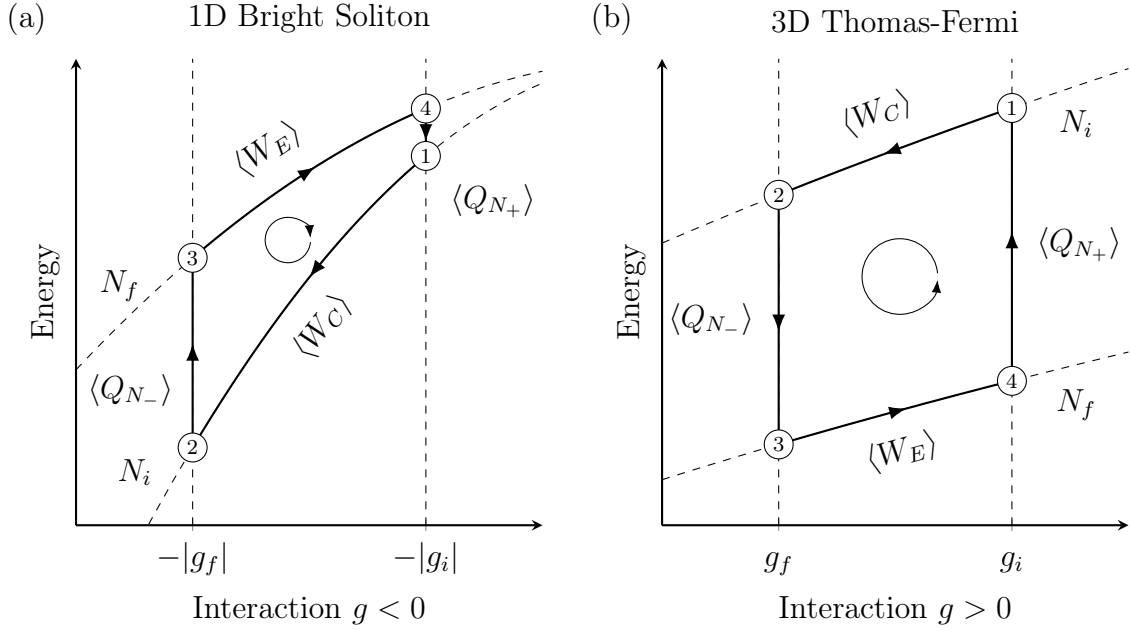


Figure 4.2: Schematic Feshbach engine cycles for (a) a harmonically trapped one-dimensional bright solitonic BEC and (b) a three-dimensional harmonically trapped BEC in the Thomas Fermi regime as the working medium. Note the clockwise and counterclockwise cycle operation in (a) and (b) respectively and see text for details.

In Publication [1] I extend this concept to repulsively interacting working media in the Thomas-Fermi regime. We know from Eq. (1.26) that in three dimensions the TF energy reads

$$E(N, g) = \frac{5}{7} N \mu_{\text{TF}} \quad \text{with} \quad \mu_{\text{TF}} = \left(\frac{15Ng}{16\pi\sqrt{2}} \right)^{2/5} \quad (4.6)$$

and the corresponding Feshbach engine cycle is shown in Figure 4.2 (b). In contrast to the bright solitonic working medium, where the engine cycle is performed in a clockwise fashion, the Thomas-Fermi engine cycle is performed counterclockwise in order to achieve finite values for the efficiency η and power P of the engine, which can be computed according to

$$\eta = -\frac{\langle W_C \rangle + \langle W_E \rangle}{\langle Q_{N_-} \rangle} \quad \text{and} \quad P = -\frac{\langle W_C \rangle + \langle W_E \rangle}{\tau} \quad (4.7)$$

as a function of cycle time τ . Assuming that the isochoric strokes are performed a lot faster than the adiabatic strokes, the complete cycle duration is assumed to be $\tau \approx 2T_f$. The maximum attainable adiabatic efficiency of the Feshbach engine is given to a good approximation by

$$\eta_{\text{AD}} \approx 1 - \left(\frac{|g_i|}{|g_f|} \right)^2, \quad (4.8)$$

for the one-dimensional bright solitonic working medium, after ignoring negligible contributions from the potential energy, and for a working medium in the Thomas-Fermi

regime we have

$$\eta_{\text{AD}} = 1 - \left(\frac{g_f}{g_i} \right)^\gamma, \quad (4.9)$$

with $\gamma = 2/3$ (1D BEC), $\gamma = 1/2$ (2D BEC), and $\gamma = 2/5$ (3D BEC).

The shortcuts to adiabaticity that we derived in the previous chapter come into play if we want to actually run the engine. If the adiabatic compression and expansion strokes are performed in some finite time T_f , their work output is modified by some amount known as irreversible work

$$W_{\text{irr}} = \langle W_{C/E}^{T_f} \rangle - \langle W_{C/E}^{\text{ad}} \rangle = E(T_f) - E_f \quad (4.10)$$

compared to the maximum attainable adiabatic amount, as a result of the adiabatic theorem. Similarly, the fidelity

$$F = |\langle \psi(T_f) | \psi_{\text{target}} \rangle|^2 \quad (4.11)$$

at the end of the stroke might be less than unity. It measures how close the state $|\psi(T_f)\rangle$ with energy $E(T_f)$ after the evolution is to the desired target state $|\psi_{\text{target}}\rangle$ with energy E_f . But if we simply increase the ramp duration to bring the efficiency of the engine closer to the adiabatic value, the power output will vanish as $\tau \rightarrow \infty$, thereby rendering the engine useless. In classical engines one generally aims for maximum power output in this trade-off between power and efficiency. Fundamentally, the Curzon-Ahlborn bound $\eta_{\text{CA}} = 1 - \sqrt{T_c/T_h}$ provides a limit to this efficiency at maximum work output [178, 179], where again T_c and T_h are the temperatures of the cold and hot heat baths.

The main focus of the publication presented in the following chapter is on evaluating the performance boost achieved by using the shortcuts to adiabaticity derived in the previous chapter for running a Feshbach engine cycle in finite time and for a repulsively interacting working medium in the Thomas-Fermi regime. In order to perform the numerically demanding simulations of the three-dimensional BEC dynamics on long timescales, I implemented the Fourier split-step method presented in Chapter 2 on a GPU, based on the open-source *GPUE* codebase [105]. Numerically, the minimum ramp duration T_f^{min} resulting from the onset of the modulational instability was determined by the sharp increase in irreversible work, in particular from the point where it crosses the threshold $W_{\text{irr}} > 10^4$ chosen based on the system parameters.

4.3 Publication

The main results of this chapter are published in Reference [1]:

Tim Keller, Thomás Fogarty, Jing Li, and Thomas Busch
Feshbach engine in the Thomas-Fermi regime
 Physical Review Research **2**, 033335 (2020).

I have derived all of the analytical results, performed all of the numerical simulations and wrote a first draft of the manuscript. All authors contributed to the discussion and interpretation of the results and to the writing of the final version.

4.4 Experimental Considerations

An experimental realization of even just a single Feshbach engine cycle might prove too challenging for current experiments, particularly because it is difficult to achieve the faithful control over BEC particle numbers required for the isochoric strokes. Also, at the moment the engine is not coupled to an external environment and there is no mechanism for extracting useful work from it. I will expand on this below and discuss several ideas for engineering such a coupling that would allow one to harness its power. Nonetheless, the main novelty of this work, which is the shortcut to adiabaticity for interaction ramps of Bose-Einstein condensates in the commonly found Thomas-Fermi regime and the associated analytical expression for the minimal ramp duration, might prove useful for improving the experimental control of BECs and are well within experimental reach. In order to enable precise tunability of the atomic interactions over a wide range, it is favorable to have a broad Feshbach resonance such as in ^{85}Rb [180] or particularly in ^7Li where the scattering length can be tuned over seven orders of magnitude [181].

Using Lithium as an example, we can translate the dimensionless quantities back into physical units. For the trapping potential we assume an isotropic harmonic trap with a frequency of roughly $\omega \approx 2\pi \times 40$ Hz, which is a typical value for the ^7Li experiment in the group of Prof. David Weld at UCSB in California with whom we have recently started to explore a collaboration [182]. The cycle endpoints for the three-dimensional BEC working medium presented in the publication were mainly chosen for numerical convenience. Using Eq. (1.6) to transform the dimensionless interaction strengths g according to $g\hbar\omega x_0^3 = 4\pi\hbar^2 a_s/m$ leads to

$$a_s = \frac{g}{4\pi} \sqrt{\frac{\hbar}{m\omega}}. \quad (4.12)$$

With the mass $m = 7.016 m_u$ of ^7Li , the endpoints translate to scattering lengths of $g_i = 1 \rightarrow a_s \approx 9025 a_0$ and $g_f = 0.8 \rightarrow a_s \approx 7220 a_0$ in units of the Bohr radius a_0 . Those are rather large values but still within reach of the Feshbach resonance. The system size of $N_i = 10^4$ and $N_f = 8 \times 10^3$ is rather small. An experimentally more common system size of e.g. $N \approx 10^5$ has the added benefit of being able to ‘trade’ atom number for interaction strength and equivalently reduce the scattering length by an order of magnitude to a more commonly found value of several hundreds of Bohr radii, while still remaining in the Thomas-Fermi regime to the same degree.

In this setup the interaction ramps presented in the publication therefore translate to e.g. $\omega T_f = 2 \rightarrow T_f \approx 7.96$ ms for a moderate, still nearly linear ramp that does not require any modulation of the interaction strength beyond the initial or final values. The minimal duration before triggering the modulational instability is $T_f^{\min} \approx 200 \mu\text{s}$ and the minimum time to ensure $g(t) \geq 0$ at all times, i.e. remaining on the positive branch of the Feshbach resonance is $T_f^{\min} \approx 2$ ms. These ramp times would enable nearly perfect adiabatic control over the interaction strength in a BEC on one to two orders of magnitude faster time scales than typical experimental state preparation times [182].

4.5 Conclusion & Outlook

I have derived a shortcut to adiabaticity for interaction ramps of the interparticle repulsion in a Bose-Einstein condensate in the Thomas-Fermi limit by exactly solving the dynamics using a scaling ansatz and showed how using this shortcut for the adiabatic strokes of a Feshbach engine can boost its performance. Numerical simulations of the full condensate dynamics unveiled that the need to drive the condensate at increasingly attractive interactions may trigger a modulational instability, leading to a condensate collapse and limiting the speed-up. Furthermore, I performed a stability analysis and determined an analytic criterion providing an accurate limit T_f^{\min} for given ramp and condensate parameters. Finally, the shortcut has good prospects of providing real-world benefits for experimental high-fidelity state preparation in systems with broad Feshbach resonances such as ^7Li .

Regarding future work, two things that come to mind immediately are the actual implementation of the isochoric engine strokes and engineering ways to harness the work of the engine. Both points are addressed in the following subsections.

4.5.1 Isochoric Strokes

In the presented work we have neglected the dynamics of the isochoric strokes in the Feshbach engine cycle in order to focus on the benefit provided by the shortcuts to adiabaticity for the engine operation. A natural extension to this work, also considering possible experimental implementations, is therefore to explicitly model these isochoric strokes as well. As shown in Chapter 1, the number of condensed atoms in a BEC mainly depends on the temperature of the system, which is determined from the thermal cloud of non-condensed atoms surrounding the BEC. The change in the number of condensed atoms during the isochoric strokes could therefore be modeled by including the thermal cloud and changing its temperature, which would also be the likely experimental procedure for these strokes.

There are several well-established models incorporating finite-temperature effects into the BEC description, see e.g. Refs. [183] and [184] for detailed and accessible reviews on the topic. There are two main approaches for modelling particle exchange between condensed and non-condensed fraction: one is the hydrodynamic quantum Boltzmann equation, commonly referred to as the Zaremba-Nikuni-Griffin or short ZNG formalism after the authors of Refs. [185, 186]. It uses two distinct equations for modeling the BEC and for modeling the thermal cloud. Another approach, which does not rely on this somewhat artificial separation and which is also able to capture other essential physics like the spontaneous symmetry breaking of the order parameter phase during the condensation, is the stochastic projected Gross-Pitaevskii equation (SPGPE) formalism. Most importantly, this approach includes number-conserving energy damping in the form of collisions between thermal and condensed atoms, which might play an important role during the fast shortcut strokes at fixed particle number [187]. In its present form, it was first introduced by Gardiner and coauthors in Refs. [188, 189] and detailed reviews of the SPGPE and related c-field techniques can be found in Refs. [190, 191].

Experimentally, it might be advantageous to use the concept of a dimple trap that made it possible e.g. to reach Bose-Einstein condensation purely by laser cooling [192] and that is currently used to create continuously replenished BECs [193]. It consists of a large cloud of harmonically trapped, pre-cooled atoms which acts as a particle reservoir for the BEC in the tight dimple potential at the center of the trap. This mechanism could allow one to reliably perform the changes in BEC size during the isochoric strokes.

4.5.2 Extracting Work from the Engine

The main purpose of an engine is to perform usable work. Using the mostly mechanical work supplied by classical heat engines is generally not a problem. For quantum heat engines however, coupling their working medium to the environment means introducing an additional channel for noise and decoherence. These are effects that experimentalists usually try to minimize at all costs in order to successfully study quantum systems. Nonetheless, finding ways to make the work of quantum heat engines usable without impairing their performance too much is a crucial step in the further development of these, up to now, mostly conceptual devices. One approach, which focuses on storing the work output in a flywheel [194] instead of using it directly, has recently been demonstrated experimentally for a single ion heat engine [195].

In the case of the Feshbach engine, different approaches for coupling the engine to a mechanical system and making its work usable can be conceived. First, an immediate coupling between the BEC and the system, directly converting the work of the engine into mechanical motion. Mechanical coupling between a BEC and an oscillating micro-cantilever was already demonstrated experimentally [196]. The coupling relies on the Casimir-Polder force [197] that arises from changes in vacuum fluctuations of the quantized electromagnetic field as two objects are brought in close proximity to each other. A more sophisticated approach suggests using a nano-cantilever equipped with a magnetic tip as well as a spinor or multi-component BEC, introduced in more detail in Section 6.2, and coupling them via the Zeeman effect [198].

An experimentally less challenging approach could be realized via an indirect coupling, e.g. by placing the BEC in an optomechanical cavity, containing a vibrating cavity mirror and driven by a pump laser. This system gives rise to an indirect coupling between the BEC working medium and the mechanical motion of the cavity mirror, mediated by the cavity field. In the dispersive limit, i.e. for a large atomic detuning between the laser frequency and an atomic transition frequency, the atoms can be regarded as linearly polarizable particles coherently scattering cavity photons [199, 200]. The BEC changes the optical path length inside the cavity, leading to a reduction in the effective cavity frequency proportional to $\sim \int dx |\psi(x)|^2 \cos(kx)$ with k being the wave vector of the cavity. However, preliminary calculations suggest that for typical cavities k is too large to resolve the compression and expansion of the atomic cloud by several μm considered in this work and the integral simply averages to the same value, independent of $|\psi(x)|^2$.

Therefore, one would need to find a way to circumvent this problem, possibly by making use of additional internal atomic states or collective effects available in driven-dissipative optomechanical cavities such as superradiance or bistability [201].

Chapter 5

Adiabatic critical quantum metrology cannot reach the Heisenberg limit even when shortcuts to adiabaticity are applied (Publication [2])

This chapter is based on the publication of the same name and presents its context, additional unpublished results based on my contribution to this work and its impact.

5.1 Introduction

The process of measuring is at the core of science itself and the field of metrology addresses the problem of obtaining both accurate and precise measurements. The acquired values are affected by systematic and stochastic errors. By repeating the same measurement on N identically prepared, independent probes and calculating the mean value $\bar{\Theta}_N = \sum_i \Theta_i / N$ of the outcomes Θ_i , the stochastic error can be reduced. As a result of the central limit theorem [202], the standard deviation σ_{mean} of the discrepancy between the measured mean and the desired quantity, i.e. the true mean μ , scales as

$$\sigma_{\text{mean}} = \sqrt{\text{Var}(\bar{\Theta}_N - \mu)} = \frac{\sigma}{\sqrt{N}} \quad (5.1)$$

for large enough N , independent of the underlying probability distribution and where $\sigma^2 = \text{Var}(\Theta_i)$ is the variance of the random samples. In other words, as σ_{mean} decreases proportional to $1/\sqrt{N}$ with the number of measurements taken, the precision of a measurement increases. In the context of quantum optics, e.g. when measuring the phase difference between two optical paths in an interferometer, one commonly uses a single probe beam consisting of N photons instead of N individual probes. Then the scaling of the phase estimation error with $\sim 1/\sqrt{N}$ is also known as the shot-noise or standard quantum limit (SQL) [203].

By making use of quantum resources such as squeezed or entangled states, the precision can be enhanced so that the error scales as $\sim 1/N$, a fundamental limit following from the uncertainty relation, the famous Heisenberg limit [204], which is a

central aspect of quantum metrology [205]. Critical quantum metrology, which is at the heart of this chapter and which will be introduced in more detail in the following section, is a variant of quantum metrology in which one tries to make use of the diverging susceptibility close to the critical point of a system in order to increase the precision of measurements.

In this chapter I first present a shortcut to adiabaticity for the Landau-Zener model and derive a local counterdiabatic shortcut for the quantum Rabi model in the Schrieffer-Wolff approximation. Both models are used as critical toy models in Publication [2], supporting the general result that shortcuts to adiabaticity cannot be used to increase the obtainable precision in critical quantum metrology, which is presented there. The chapter concludes with a summary and an outlook to numerous further works that already cite the publication.

5.2 Critical Quantum Metrology

In quantum metrology the variance of a measurement is limited by the Cramér-Rao bound [206]

$$\text{Var}(\Theta) \geq \frac{1}{\sqrt{\mathcal{I}_\Theta}}, \quad (5.2)$$

where the quantum Fisher information \mathcal{I}_Θ (QFI) for a pure state $|\psi(\Theta)\rangle$ depending on the measured quantity Θ is defined as

$$\mathcal{I}_\Theta = 4 \left(\langle \partial_\theta \psi | \partial_\theta \psi \rangle - \langle \partial_\theta \psi | \psi \rangle^2 \right). \quad (5.3)$$

Using perturbation theory and considering a Hamiltonian $\hat{H}(\Theta)$ with eigenenergies $E_n(\Theta)$ and eigenstates $|\psi_n(\Theta)\rangle$, the QFI can be expressed as [207]

$$\mathcal{I}_\Theta = 4 \sum_{n>0} \frac{\left| \langle \psi_n(\Theta) | \partial_\Theta \hat{H}(\Theta) | \psi_0(\Theta) \rangle \right|^2}{[E_n(\Theta) - E_0(\Theta)]^2}. \quad (5.4)$$

If the denominator vanishes, e.g. as the result of a closing energy gap $E_1(\Theta) \rightarrow E_0(\Theta)$ between the ground state and first excited state during a quantum phase transition, the quantum Fisher information diverges, allowing one in principle to achieve arbitrarily high precision according to Eq. (5.2). This is the basic idea behind critical quantum metrology [208].

For a more intuitive picture, one can also think in terms of susceptibilities or the response of a system to a perturbation. Phase transitions are characterized by a divergence in the susceptibility as a function of the parameter driving the transition [17]. Close to the critical point, small changes in the control parameter lead to large changes in the response of the system and this enhanced sensitivity can then in principle be used for precise measurements of the control parameter in critical quantum metrology.

However, as a result of the critical slowing down of the dynamics close to a critical point in a quantum system as described in the Kibble-Zurek mechanism [209–211], the time needed to adiabatically prepare such a critical state also diverges. If this is taken

into account, the seemingly arbitrarily high precision is still bounded by the Heisenberg limit, as shown e.g. in Ref. [212].

As we have seen in the previous chapters, shortcuts to adiabaticity allow one to mimic adiabatic evolution in a finite time. One can therefore immediately ask the question if it is possible to overcome the Heisenberg limit by applying shortcuts to adiabaticity in critical quantum metrology. It would then be possible to trade the energetic cost of realizing such a finite time adiabatic dynamics for increased measurement precision [213]. However, as my coworkers and I have shown in Publication [2], it is not possible to beat or even reach the Heisenberg limit by using shortcuts to adiabaticity in critical quantum metrology and they are even detrimental to the achievable precision in some cases. This even applies in the case where the desired quantity is already exactly known a priori, since the control protocols for performing a shortcut generally depend on the unknown parameter.

5.3 Shortcuts for Critical Toy Models

In this section I introduce the shortcuts to adiabaticity for the two models that were used in Publication [2] to show the general ineffectiveness of shortcuts in critical quantum metrology. The first one is the Landau-Zener model, for which shortcuts are well known, see e.g. Ref. [119]. The second one is the quantum Rabi model, where to the best of my knowledge shortcuts were given explicitly first in Ref. [214] shortly before our publication, but have not been presented anywhere for the quantum Rabi model after a Schrieffer-Wolff transformation that we use in Ref. [2]. Particularly, not the local counterdiabatic driving term and the connection to the scaling transformation which I derive here.

5.3.1 Landau-Zener Model

The Landau-Zener model [215, 216] is a simple two-level system describing a spin in a time-dependent field $g(t)$ and its Hamiltonian reads

$$\hat{H} = \frac{\Delta}{2}\hat{\sigma}_x + \frac{g(t)}{2}\hat{\sigma}_z, \quad (5.5)$$

where $\hat{\sigma}_i$ are the Pauli matrices and the instantaneous eigenenergies are given by $E_{\pm} = \pm\frac{1}{2}\sqrt{\Delta^2 + g^2(t)}$. It does not exhibit a phase transition, but for $g(t) = 0$ it shows an avoided crossing with a energy level splitting of Δ , which makes it a good toy model to study the criticality associated with the closing of an energy gap in phase transitions. The counterdiabatic driving term that needs to be added to \hat{H} can be obtained directly via Eq. (3.1) as

$$\hat{H}_{\text{CD}} - \hat{H} = -\frac{\dot{g}(t)\Delta}{2[\Delta^2 + g^2(t)]}\hat{\sigma}_y \quad (5.6)$$

by calculating the instantaneous eigenvalues of the simple 2×2 matrix \hat{H} . This term is again nonlocal in the sense that it contains a term proportional to $\hat{\sigma}_y$, which does not commute with the terms of the original Hamiltonian. With the help of a unitary

transformation, a local counterdiabatic version

$$\hat{H}_{\text{LCD}} = \frac{\Delta(t)}{2} \hat{\sigma}_x + \frac{g(t) - \eta(t)}{2} \hat{\sigma}_z \quad (5.7)$$

can be achieved [213]. Now the level splitting $\Delta(t) = \sqrt{\Delta^2 + \dot{\Theta}^2(t)}$ with $\Theta(t) = \text{arccot}(\frac{g(t)}{\Delta})$ also needs to be modulated in time and the time-dependent field $g(t)$ is modified by the term $\eta(t) = \arctan(\dot{\Theta}(t)/\Delta)$.

5.3.2 Quantum Rabi Model

The quantum Rabi model [217] describes a single two-level system described by Pauli matrices $\hat{\sigma}_i$, interacting with a single bosonic mode according to the Hamiltonian

$$\hat{H} = \Delta \hat{a}^\dagger \hat{a} + \frac{\Omega}{2} \hat{\sigma}_z + \frac{g(t)}{2} \hat{\sigma}_x (\hat{a} + \hat{a}^\dagger) , \quad (5.8)$$

where Δ is the frequency of the bosonic mode, whose creation and annihilation operators fulfill $[\hat{a}, \hat{a}^\dagger] = 1$, Ω is the energy splitting of the two-level system and $g(t)$ describes the time-dependent coupling strength. In line with the convention in the literature, we have set $\hbar = 1$. The model exhibits a superradiant phase transition with $\langle \hat{a}^\dagger \hat{a} \rangle \gg 1$ in the limit $\Delta/\Omega \rightarrow 0$ at the critical coupling strength $g_c = \sqrt{\Delta\Omega}$. In this limit the Hamiltonian can be diagonalized using a Schrieffer-Wolff transformation [218] $\hat{U} = \exp [i(g(t)/2\Omega)(\hat{a}^\dagger + \hat{a})\hat{\sigma}_y]$ and subsequent projection onto the lower eigenstate of $\hat{\sigma}_z$, denoted by $|\downarrow\rangle$, which up to order $\mathcal{O}(\Delta\sqrt{\Delta/\Omega})$ yields [219]

$$\hat{H}_{\text{SW}} = \langle \downarrow | \hat{U} \hat{H} \hat{U}^\dagger | \downarrow \rangle = \Delta \hat{a}^\dagger \hat{a} - \frac{\Omega}{2} - \frac{g^2(t)}{4\Omega} (\hat{a} + \hat{a}^\dagger)^2 . \quad (5.9)$$

The instantaneous eigenstates are given by squeezed Fock states $|n\rangle$ [162], which are the eigenstates of \hat{a} and \hat{a}^\dagger , according to

$$|n_s(t)\rangle = \hat{S}(t) |n\rangle = \exp \left\{ \frac{\xi(t)}{2} [(\hat{a}^\dagger)^2 - \hat{a}^2] \right\} |n\rangle \quad (5.10)$$

with the squeezing parameter $\xi(t) = -\frac{1}{4} \ln [1 - (g(t)/g_c)]$ and corresponding instantaneous eigenvalues $E_n(t) = n\Delta\sqrt{1 - (g(t)/g_c)^2}$. The average number of photons is given by

$$\begin{aligned} N = \langle \hat{a}^\dagger \hat{a} \rangle &= \sinh^2 \left[\frac{1}{4} \left| \ln \left(1 - \left(\frac{g(t)}{g_c} \right)^2 \right) \right| \right] = \frac{(\sqrt{1 - (g(t)/g_c)^2} - 1)^2}{4\sqrt{1 - (g(t)/g_c)^2}} \\ &\approx \frac{1}{4\sqrt{1 - (g(t)/g_c)^2}} \quad \text{for } g \rightarrow g_c , \end{aligned} \quad (5.11)$$

reflecting the superradiant character of the transition.

From these instantaneous eigenstates we can directly compute the counterdiabatic term for a shortcut to adiabaticity according to

$$\hat{H}_{\text{CD}} - \hat{H} = i \sum_n [|\partial_t n_s(t)\rangle \langle n_s(t)| - \langle n_s(t)| \partial_t n_s(t)\rangle |n_s(t)\rangle \langle n_s(t)|] . \quad (5.12)$$

The time derivative reads

$$|\partial_t n_s(t)\rangle = \frac{\dot{\xi}(t)}{2} [(\hat{a}^\dagger)^2 - \hat{a}^2] |n_s(t)\rangle = \frac{g(t)\dot{g}(t)}{4(g_c^2 - g^2(t))} [(\hat{a}^\dagger)^2 - \hat{a}^2] |n_s(t)\rangle \quad (5.13)$$

and therefore the overlap

$$\begin{aligned} \langle n_s(t)|\partial_t n_s(t)\rangle &= \frac{g(t)\dot{g}(t)}{4(g_c^2 - g^2(t))} \langle n|\hat{S}^\dagger [(\hat{a}^\dagger)^2 - \hat{a}^2] \hat{S}|n\rangle \\ &= f(t) \left(\langle n|\hat{S}^\dagger \hat{a}^\dagger \hat{S} \hat{S}^\dagger \hat{a}^\dagger \hat{S}|n\rangle - \langle n|\hat{S}^\dagger \hat{a} \hat{S} \hat{S}^\dagger \hat{a} \hat{S}|n\rangle \right) \\ &= f(t) \langle n| \left[(\hat{a}^\dagger \cosh(s) + \hat{a} \sinh(s))^2 - (\hat{a} \cosh(s) + \hat{a}^\dagger \sinh(s))^2 \right] |n\rangle \\ &= f(t)(2n+1) [\sinh(s) \cosh(s) - \sinh(s) \cosh(s)] = 0 \end{aligned} \quad (5.14)$$

vanishes, where we have set $f(t) = g(t)\dot{g}(t)/(4(g_c^2 - g^2(t)))$ and used [220]

$$\hat{S}^\dagger \hat{a} \hat{S} = \hat{a} \cosh(s) - \hat{a}^\dagger e^{i\vartheta} \sinh(s) \quad \text{with} \quad \xi = s e^{i\vartheta} = \frac{1}{4} \left| \ln \left(1 - \left(\frac{g(t)}{g_c} \right)^2 \right) \right| e^{i\pi} \quad (5.15)$$

in our case. Using the completeness $\sum_n |n_s(t)\rangle \langle n_s(t)| = \mathbb{I}$ of the instantaneous eigenbasis, the counterdiabatic term finally reads

$$\hat{H}_{\text{CD}} - \hat{H} = i \frac{g(t)\dot{g}(t)}{4(g_c^2 - g^2(t))} [(\hat{a}^\dagger)^2 - \hat{a}^2] . \quad (5.16)$$

Transforming the counterdiabatic term in Eq. (5.16) in analogy to the quantum harmonic oscillator according to $\hat{a} = \sqrt{\frac{m\Delta}{2}} \left(\hat{x} + \frac{i}{m\Delta} \hat{p} \right)$ with some arbitrary ‘mass’ m yields

$$\hat{H}_{\text{CD}} - \hat{H} = i \frac{g(t)\dot{g}(t)}{4(g_c^2 - g^2(t))} (\hat{x}\hat{p} + \hat{p}\hat{x}) \quad (5.17)$$

and the nonlocal property of the counterdiabatic term becomes more obvious. The reappearance of the generator of dilations highlights the scaling properties of the system as a result of its squeezed state eigenstates.

It is important to note that this nonlocality in the counterdiabatic driving term is not an issue for the numerical implementation of the shortcuts in this case, due to the simple structure of the underlying Hilbert space based on Fock states. The same applies to the Landau-Zener model based on simple 2×2 Pauli matrices and the results in Publication [2] were all obtained with \hat{H}_{CD} for both models.

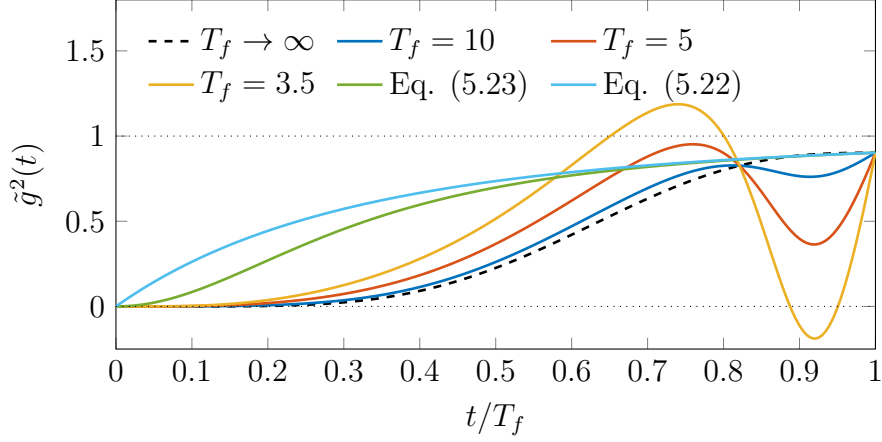


Figure 5.1: Plot of the modified local counterdiabatic driving $\tilde{g}^2(t)$ according to Eq. (5.20) for ramping from $g_i = 0$ to $g_f = 0.95$ in different times T_f . For fast ramps the driving exceeds the range of validity $0 \leq \tilde{g}^2(t) \leq 1$ of the model (dotted lines). The approximate shortcut in Eq. (5.23) (green line) needs to be driven slower than $T_f > 3.0424$ and the ramp in Eq. (5.22) (light blue line) is independent of T_f in this representation.

Nonetheless, local driving terms are desirable for physical shortcut implementations and using the results from Chapter 3, we can immediately write down the unitary transformation

$$\hat{U} = \exp [imf(t)\hat{x}^2] = \exp \left[i \frac{f(t)}{2\Delta} (\hat{a} + \hat{a}^\dagger)^2 \right] \quad (5.18)$$

that gives us a local version of the counterdiabatic driving. It reads

$$\hat{H}_{\text{LCD}} = \hat{U} \hat{H}_{\text{CD}} \hat{U}^\dagger + i \left(\partial_t \hat{U} \right) \hat{U}^\dagger = \Delta \hat{a}^\dagger \hat{a} - \frac{\Omega}{2} - \frac{\Delta}{4} \tilde{g}^2(t) (\hat{a} + \hat{a}^\dagger)^2 \quad (5.19)$$

with the modified driving function

$$\begin{aligned} \tilde{g}^2(t) &= \frac{g^2(t)}{g_c^2} + \frac{2}{\Delta^2} \left(2f^2(t) + \dot{f}(t) \right) \\ &= \frac{g^2(t)}{g_c^2} + \frac{2}{\Delta^2} \left[\dot{g}^2(t) \frac{2g_c^2 + 3g^2(t)}{8(g_c^2 - g^2(t))^2} + \frac{g(t)\ddot{g}(t)}{4(g_c^2 - g^2(t))} \right]. \end{aligned} \quad (5.20)$$

For \hat{H}_{CD} we were free to choose $g(t)$ arbitrarily, but now we need to make sure that $\tilde{g}(0) = g(0)$ and $\tilde{g}(T_f) = g(T_f)$ by imposing boundary conditions $\dot{g}(0) = \dot{g}(T_f) = \ddot{g}(0) = \ddot{g}(T_f) = 0$ which are fulfilled e.g. by the polynomial

$$g(t) = g_i + (g_f - g_i) (10s^3 - 15s^4 + 6s^5) \quad \text{with} \quad s = \frac{t}{T_f} \quad (5.21)$$

for ramping from g_i to g_f in a time T_f . Fig. 5.1 shows the resulting $\tilde{g}^2(t)$ for different ramp times and immediately one limitation of the shortcut becomes apparent. For short ramps we can have $\tilde{g}^2 < 0$, which is unphysical in the context of the quantum

Rabi model studied here, as well as $\tilde{g}^2 > 1$, where we would need to cross the phase transition.

It is tempting to try a different approach to make sure that \hat{H}_{LCD} and \hat{H} commute at $t = 0$ and $t = T_f$, namely to choose $g(t)$ in such a way that the LCD term $2f^2(t) + \dot{f}(t) \equiv 0$ in Eq. (5.20) vanishes at all times. However, this defeats the purpose and renders the shortcut useless as the mechanism achieving the adiabatic-like modulation of the wave function disappears. But it is still worth it to follow this approach as it allows one to draw an interesting connection in the end. The aforementioned condition is fulfilled by $f(t) = \frac{1}{c_0 + 2t}$ with $c_0 = 1/f(0)$ and this results in a Bernoulli type differential equation for $\dot{\tilde{g}}$ which is solved by the ramp

$$\tilde{g}(t) = \sqrt{1 + \frac{c_1}{(c_0 + 2t)^4}} = \sqrt{1 - \frac{1}{\left[1 + \left(\frac{1}{(1-g_f^2)^{1/4}} - 1\right) \frac{t}{T_f}\right]^4}}, \quad (5.22)$$

where the constants $c_1 = -c_0^4$ and c_0 are determined via the ramp boundaries $g(0) = 0$ and $g(T_f) = g_f$. As shown in Fig. 5.1, it has a fundamentally different shape from the ones using ‘*smoother step*’ polynomials. Also, in contrast to the local counterdiabatic driving, it remains bounded $g_i \leq g(t) \leq g_f$ by the initial and final values at all times and its required modulation is independent of the ramp duration T_f , which again indicates that it cannot work as a shortcut to adiabaticity. However, it is quite similar to the approximate shortcut given in Ref. [221] for the quantum Rabi model in the Schrieffer-Wolff approximation, also in the context of critical metrology. They derive the condition $\dot{\tilde{g}}(t) \sim \gamma\Delta(1 - g^2(t))^{\frac{3}{2}}$ for the dynamics to remain adiabatic, where $\gamma < 1$ is some small parameter describing the probability of exciting higher states. This is fulfilled by the approximate shortcut ramp

$$\tilde{g}(t) = \frac{1}{\sqrt{1 + \frac{1}{\gamma^2\Delta^2 t^2}}}, \quad (5.23)$$

which is also plotted in Fig. 5.1. Its duration is fixed by the final coupling strength according to $\gamma T_f = g_f/(1 - g_f^2)^{\frac{1}{2}} > 3.0424$ in our example.

Surprisingly, solving the differential equation for the driving field appearing in the local version of a counterdiabatic Hamiltonian leads to control ramps that do not work as shortcuts to adiabaticity, but that can act as very good nearly adiabatic ramps if performed on appropriate timescales. This can also be seen in the interacting many-body system in Section 3.2. There, the interaction ramp $g(t)$ can also be chosen in such a way that the additional term $\ddot{g}/g - 2(\dot{g}/g)^2 \equiv 0$ in Eq. (3.22) disappears. The resulting ramp

$$g(t) = \frac{g_i g_f}{g_f + \frac{t}{T_f}(g_i - g_f)}, \quad (5.24)$$

also does not work as a shortcut, but when used as an adiabatic reference it outperforms even the ‘*smoother step*’ polynomial in Fig. 3.2 on intermediate timescales, despite not fulfilling ‘smooth’ boundary conditions.

5.4 Publication

The main results of this chapter are published in Reference [2]:

Karol Gietka, Friederike Metz, **Tim Keller**, and Jing Li
*Adiabatic critical quantum metrology cannot reach the Heisenberg
 limit even when shortcuts to adiabaticity are applied*
 Quantum **5**, 489 (2021).

The project idea as well as the central analytical and numerical results stem from Karol Gietka. I have mainly contributed the novel shortcut to adiabaticity for the case study with the quantum Rabi model under the Schrieffer-Wolff transformation and to the interpretation of the results in terms of Fig. 5 in the publication. All authors contributed to the discussion and interpretation of the results and to editing the final version of the paper.

5.5 Conclusion & Outlook

I have derived a shortcut to adiabaticity in the local counterdiabatic form for the quantum Rabi model in the Schrieffer-Wolff approximation that was used together with a known shortcut for the Landau-Zener model to support the general result presented by my coworkers and me in Publication [2]. Namely, that STAs or any other unitary transformation for that matter are not able to reach the Heisenberg limit when used in critical quantum metrology. Surprisingly, they even lead to worse performance in some instances, as by construction they counteract the divergence of the geometrical distance between close-by quantum states as they approach a critical point, which is the working principle of critical quantum metrology. Moreover, I have described a surprising observation, whereby solving the differential equations appearing in the local counterdiabatic control ramps both for the quantum Rabi model and for the interacting quantum gas in Section 3.2 seemingly leads to well-performing adiabatic reference ramps. However, this is purely anecdotal and needs further investigation.

Despite its very recent publication, the work presented in this chapter has already found recognition in the community and has been cited numerous times. At the time of writing, it has been mentioned by Ilias et al., who derive novel protocols for criticality-enhanced sensing that work by continuously measuring the system during critical state preparation [222], Garbe and coworkers, who provide a unifying analysis for the scaling of the quantum Fisher information in critical quantum metrology as a function of the protocol duration [223] and who also describe a novel superradiant phase transitions for a light-matter system in the ultrastrong coupling regime [224]. Furthermore, Hatomura and coworkers, who consider the finite-time duration of preparing a state for quantum metrology based on symmetry-protected adiabatic transformations [225] and Aybar et al. who study critical quantum thermometry in spin systems [226]. Finally, the first author of the publication, Karol Gietka, also used it as a basis for deriving novel protocols for critical quantum metrology that work either by moving away from the critical point [227] or even by crossing it [228].

Part III

Interacting Two-Component Systems in 1D

Chapter 6

Background

In this chapter I introduce the superfluid to Mott insulator transition of a strongly interacting, one-dimensional bosonic quantum gas in a lattice potential that was the motivation for the studies performed in Chapters 7 and 8. It was described theoretically by Büchler et al. in Ref. [229] and measured experimentally by Haller et al. in Ref. [230]. In these and further publications it is also commonly referred to both as commensurate-incommensurate transition and pinning transition. I also present a general introduction to the very broad topic of atomic mixtures, as both of the following Chapters 7 and 8 deal with one-dimensional binary mixtures .

6.1 Pinning Transition

A one-dimensional bosonic quantum gas in a periodic lattice potential with wave vector $k = 2\pi/\lambda$, described in second quantization via creation and annihilation operators $\hat{\Psi}^\dagger(x)$ and $\hat{\Psi}(x)$, has the Hamiltonian

$$\hat{H} = \int dx \hat{\Psi}^\dagger(x) \left[-\frac{\hbar^2}{2m} \frac{\partial^2}{\partial x^2} + V_0 \sin^2(kx) \right] \hat{\Psi}(x) + \frac{g}{2} \int dx \hat{\Psi}^\dagger(x) \hat{\Psi}^\dagger(x) \hat{\Psi}(x) \hat{\Psi}(x), \quad (6.1)$$

where the depth of the potential V_0 is often expressed in terms of the recoil energy $E_R = \hbar^2 k^2 / 2m$ and where the atoms are interacting via the previously introduced contact interactions of strength g . In general, there is no analytic solution to the Hamiltonian (6.1), however there are two parameter regimes where it can be mapped to different Hamiltonians that allow for an easier treatment. To this end, we introduce the Lieb-Liniger parameter $\gamma = \frac{mg}{\hbar^2 n}$, which relates the interaction energy to the kinetic energy and characterizes the interaction strength in a system of average line density n . In the limit of strong interactions $\gamma \gg 1$ and shallow lattices $V_0 \ll E_R$, Büchler et al. showed in Ref. [229] that Hamiltonian (6.1) can be mapped to the exactly solvable sine-Gordon model

$$H = \frac{\hbar v_s}{2\pi} \int dx \left[K (\partial_x \phi)^2 + \frac{1}{K} (\partial_x \theta)^2 + \mathcal{V} \cos(2\theta) \right], \quad (6.2)$$

which is a field theory describing spatial fluctuations in the density and phase fields θ and ϕ obtained from the bosonic field operator according to

$$\hat{\Psi}(x) \sim \sqrt{n + \partial_x \theta(x)/\pi} \exp[i\phi(x)]. \quad (6.3)$$

They obey the commutation relation $[\partial_x \theta(x), \phi(y)] = i\pi\delta(x - y)$. Importantly, this mapping requires the atomic density to be commensurate to the lattice periodicity and assumes a density of $n = 2/\lambda$. The parameter v_s stands for the velocity of sound-like excitations in the one-dimensional gas, $\mathcal{V} = V_0 n \pi / (\hbar v_s)$ describes the lattice depth and the Luttinger liquid parameter K incorporates the interactions. In the absence of a lattice potential, an approximate closed expression in the limit of strong interactions, which is valid for $\gamma > 10$, reads $K(\gamma \rightarrow \infty) \approx (1 + 2/\gamma)^2$ [231].

The sine-Gordon model possesses a Berezinskii-Kosterlitz-Thouless type transition at $K_c = 2$ from a superfluid state for $K > 2$ to a gapped Mott insulating phase for $K < 2$ [232, 233]. Using a different asymptotic expression $K(\gamma \rightarrow 0) \approx \pi [\gamma - (\gamma^{3/2}/2\pi)]^{-1/2}$ for the Luttinger parameter [231], valid in the weak interaction regime up to $\gamma \lesssim 10$, the criterion translates to the phase transition line

$$\frac{V_0}{E_R} = 2 \left(\frac{\pi}{\sqrt{\gamma - \frac{\gamma^{3/2}}{2\pi}}} - 2 \right) \quad (6.4)$$

in the $\gamma - V_0$ -plane. From Eq. (6.4) we can immediately see that above a critical interaction strength $\gamma > \gamma_c \approx 3.5$, arbitrarily shallow lattice potentials cause the system to become pinned in the Mott insulating state.

In the opposite regime of weak interactions $\gamma \ll 1$ and deep lattices $V_0 \gg E_R$, Hamiltonian (6.1) can be mapped to the well-known Bose-Hubbard model

$$\hat{H} = -J \sum_i (\hat{b}_i^\dagger \hat{b}_{i+1} + \text{h.c.}) + \frac{U}{2} \sum_i \hat{b}_i^\dagger \hat{b}_i^\dagger \hat{b}_i \hat{b}_i, \quad (6.5)$$

where the operators \hat{b}_i^\dagger and \hat{b}_i create and destroy a particle at lattice site i respectively and the hopping term $J = \frac{4E_R}{\sqrt{\pi}} \left(\frac{V_0}{E_R}\right)^{3/4} \exp\left(-2\sqrt{\frac{V_0}{E_R}}\right)$ as well as the on-site interaction $U = \sqrt{2\pi} \frac{g}{\lambda} \left(\frac{V_0}{E_R}\right)^{1/4}$ are obtained from expanding the bosonic field operator $\hat{\Psi}(x) = \sum_i w(x - x_i) \hat{b}_i$ in terms of Wannier functions $w(x)$ [234]. Its famed phase diagram as a function of J , U and the chemical potential consists of several stacked lobes for small values of J/U , where the ground state is a Mott insulating phase with an integer number of particles per lattice site depending on the chemical potential [63]. These lobes are surrounded by a superfluid phase. Our case of $n = 2/\lambda$ with a single atom per lattice site corresponds to the lowest Mott lobe, for which the superfluid-insulator transition occurs at the critical ratio $(U/J)_{\text{crit}} \approx 3.85$ [235]. This translates to the implicit equation

$$4 \frac{V_0}{E_R} = \ln^2 \left[\frac{2\sqrt{2}\pi}{\gamma} \left(\frac{U}{J}\right)_{\text{crit}} \sqrt{\frac{V_0}{E_R}} \right] \quad (6.6)$$

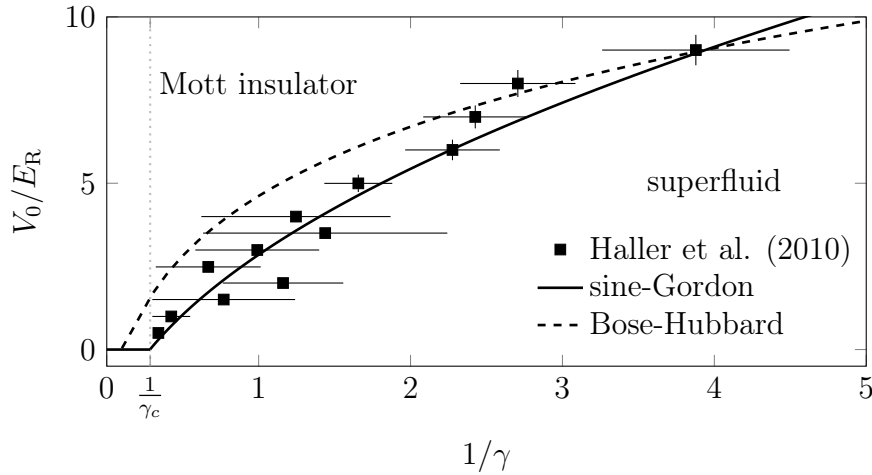


Figure 6.1: Phase diagram of Hamiltonian (6.1) according to its mapping to the sine-Gordon model [Eq. (6.4), solid line] and the Bose-Hubbard model [Eq. (6.6), dashed line]. The transition lines agree well with the experimentally observed data (squares, manually extracted from Fig. 4 in Ref. [230]) in their respective regimes of validity. The thin dotted line indicates the critical interaction strength $\gamma_c = 3.5$

determining the transition line in the $\gamma - V_0$ -plane. Figure 6.1 shows the phase diagram of Hamiltonian (6.1) according to the phase transition lines in Eqs. (6.4) and (6.6) from the mappings to the sine-Gordon and Bose-Hubbard models respectively. The critical lines agree well with the experimentally observed points by Haller et al. in Ref. [230] in their respective regimes of validity for large interaction strengths and shallow lattices (sine-Gordon model) and for weak interaction strengths and deep lattices (Bose-Hubbard model).

6.2 Atomic Mixtures

One of the most important and prominent examples of atomic mixtures in the field of ultracold physics is the Bose-Fermi mixture of ^3He and ^4He that acts as the coolant in dilution refrigerators [236]. It allows experiments to reach temperatures in the mK range and is at the basis of countless breakthroughs in solid state physics and quantum computing [237].

For quantum gases, the first binary mixture of Bose-Einstein condensates in two different hyperfine states of ^{87}Rb , a so-called spinor condensate [238], was observed experimentally in Ref. [239] after theoretical studies of Bose-Bose mixtures in Refs. [240, 241]. Since then many further examples of mixtures in the form of dual-species condensates [242–250] and spinor condensates [251–257] have been realized. The order parameter of spinor condensates can be described by a vector with several components for the internal degrees of freedom. In contrast to scalar Bose-Einstein condensates, spin-exchange collisions can change the populations of the sublevels, meaning that the number of condensed atoms in each species is not conserved, which leads to a rich phase diagram [258].

Originally, Bose-Fermi mixtures were used as a tool to circumvent the difficulty of direct cooling of fermions in order to reach the quantum degenerate regime of the fermionic component by means of sympathetic cooling via the bosonic component [259]. In 2014, the same mixture of fermionic ${}^6\text{Li}$ and bosonic ${}^7\text{Li}$ was created for the first time with the fermionic component at unitarity, so that both components are superfluid at the same time [260]. Theoretical studies of three-dimensional Bose-Fermi mixtures can be found for example in Refs. [261, 262]. Using the Thomas-Fermi approximation for the bosonic component, a comprehensive classification of possible density distributions was given more recently [263], after first studies in Ref. [264].

As we will see later on, the mixture of bosonic ${}^{87}\text{Rb}$ and fermionic ${}^{40}\text{K}$ is a very suitable candidate for observing the self-pinning transition reported in the following chapters, mainly due to the large attractive interspecies interaction [265, 266]. In the past, it has been used to study collapse phenomena [267, 268] and the loss of bosonic phase coherence in an optical lattice [269]. Other realizations of dual-species mixtures involving ${}^6\text{Li}$ include ${}^{23}\text{Na}$ [270] as well as ${}^{133}\text{Cs}$ [271], while other isotopic Bose-Fermi mixtures have been attained using ${}^{40/41}\text{K}$ [272], ${}^{84/87}\text{Sr}$ [273] and ${}^{173/174}\text{Yb}$ [274]. More recently, also a quantum degenerate mixture of ${}^{87}\text{Rb}$ and ${}^{171}\text{Yb}$ was achieved [275].

For completeness, it is also noteworthy to mention experimental realizations of dual-species Fermi-Fermi mixtures in ${}^6\text{Li}$ and ${}^{40}\text{K}$ [276, 277] and especially balanced mixtures of the lowest hyperfine states of either of the aforementioned species which allowed studying the BEC-BCS crossover from condensates of tightly bound molecules to a superfluid of weakly-bound Bardeen-Cooper-Schrieffer (BCS) pairs (see e.g. Refs. [29, 278] and references therein). As demonstrated in the group of Wolfgang Ketterle, having a population imbalance on the BEC side of the transition can even lead to the realization of an effective Bose-Fermi mixture in that case [279]. On the other hand, for a large enough mass imbalance, Fermi-Fermi mixtures are predicted to phase separate [280]. A more recent development in atomic mixtures is the observation of quantum liquid droplets that are stabilized by quantum fluctuations in a two-component mixture with intraspecies repulsion and interspecies attraction by Tarruell and colleagues [281], after a theoretical description by Petrov in 2015 [282].

Within the mean-field level description, a BEC consisting of multiple atomic species gives rise to additional intraspecies (g_{ii}) and interspecies (g_{ij} , $i \neq j$) interaction terms in the Gross-Pitaevskii equation for each order parameter ψ_j of the s different components

$$i\hbar \frac{\partial \psi_j}{\partial t} = \left(-\frac{\hbar^2}{2m} \nabla^2 + V_j(\mathbf{r}) + \sum_{i=1}^s g_{ij} |\psi_i|^2 \right) \psi_j. \quad (6.7)$$

Most notably, in the case of a homogeneous two-component BEC and $g_{ij} > 0 \forall i, j$, a simple energetic argument predicts a phase transition at

$$g_{12}^2 = g_{11}g_{22}, \quad (6.8)$$

driving the system from a miscible ($g_{12}^2 < g_{11}g_{22}$) to an immiscible ($g_{12}^2 > g_{11}g_{22}$), component-separated, phase [27, 39]. In the case of trapped condensates, the transition point is marginally shifted and for multiply connected geometries like toroidal traps, the phase transition allows the condensates to switch between quantized and

classical angular rotation in the miscible and immiscible regime respectively [283]. Experimentally, the miscible-immiscible transition was first observed in Ref. [244].

In this part of my thesis, I will focus on one-dimensional mixtures, which for example allows me to study the combination of weakly and strongly correlated systems. A detailed review of one-dimensional versions of the Bose-Bose, Fermi-Fermi, and Bose-Fermi mixtures mentioned above, with a focus on few-body systems, can be found in Ref. [284].

Chapter 7

Self-Pinning Transition of a Tonks-Girardeau Gas in a Bose-Einstein Condensate (Publication [3])

This chapter is based on the publication of the same name and presents its context, a connection to experimentally relevant parameter regimes and prospects for future work.

7.1 Introduction

Quantum phase transitions are one of the most interesting aspects of quantum many-body physics [17]. They underlie many of the novel states and unique properties that for example allow neutral atoms in optical lattice potentials to be used as quantum simulators of condensed matter physics [22–25]. As we have seen in the previous chapter, a one-dimensional quantum gas subject to a lattice potential undergoes a transition from a superfluid state to a gapped Mott insulator state for arbitrarily small lattice strengths beyond a critical value of the interparticle repulsion. The research presented in this chapter was motivated by the simple question if the same physics can be observed without the need for a commensurate lattice potential, but by immersing the strongly-correlated quantum gas into a weakly-correlated background such as a BEC instead. The immersed component might then be able to create its own always perfectly commensurate trapping potential via the backaction onto the background gas. In other words, we want to study if the resulting decrease in energy from opening a gap at the Fermi surface of a fermionic-like system, similar to the Peierls instability discussed in Subsection 1.5.2, outweighs the energetic cost of creating the necessary deformation in the BEC density in the first place, thus leading to the desired quantum phase transition.

Such backaction principles are for example able to create photon-mediated long-range interactions between atoms in optical cavities [200], which can lead to self-organization phase transitions such as the Dicke transition [285–288] and the superfluid-supersolid transition [289]. In atomic mixtures, mediated interactions are inherently attractive at short distances, independent of the sign of the interaction between the

components [290]. No matter if atoms of species A attract or repel atoms of species B, the resulting change in local density of species B around atoms of species A compared to the background density is attractive for other atoms of species A in either case. This mediated attractive interaction was used to collapse an inherently repulsive BEC immersed into a Fermi gas [291] and it was shown how induced interactions can lead to a damping of BEC excitations in a similar system [292]. Furthermore, mediated interactions are also predicted to lead to supersolid formation in 2D [293, 294] and 3D [295] Bose-Fermi mixtures.

One-dimensional binary mixtures like the one studied in this chapter have seen a lot of attention, particularly over the last twenty years. Despite the bosonic nature of the Tonks-Girardeau gas, all local properties of the system such as the densities should be identical to an equivalent Bose-Fermi mixture due to the mapping theorem of the same name [82, 296]. Therefore, I will focus on results obtained for Bose-Fermi mixtures in this introduction and present literature about Bose-Bose mixtures in the following Chapter 8, where I study the same system away from the Tonks-Girardeau limit.

The phase diagram of 1D Bose-Fermi mixtures has been studied both for homogeneous systems on a ring [297] and in optical lattices both at zero temperature [298] and with superimposed harmonic trapping [299] as well as at finite temperature [300–303]. For homogeneous systems with equal masses and identical interaction strengths, exact solutions are available both for spin-polarized [304, 305] and non-polarized [306] fermions. Adding external confinement, further solutions are given in the limit of infinitely repulsive interactions [307] and for few-body systems [308].

In general, it has been found that the system can be described as a miscible two-component Luttinger liquid, which in different interaction and density regimes exhibits instabilities like the formation of bound pairs or collapse for attractive intercomponent interactions or phase separation in the repulsive case [309, 310]. Later on, it was shown that this rich phase diagram can also be understood in terms of a Luttinger liquid of polarons, i.e. atoms dressed by clouds of the opposite species [311]. The paired phase is characterized by the opening of an energy gap and in the case of imbalanced mixtures with asymmetric masses it has been shown that this is caused by a generic mechanism that does not rely on the presence of a periodic potential and which is independent of the specific nature of the mixture components [312].

The pairing effect has also been studied specifically for a balanced ^{40}K – ^{87}Rb mixture [313]. In the imbalanced case, signatures of a self-trapped ground state and the appearance of bright solitons similar to the work described here were reported in Refs. [314–316] and in the presence of disorder, the system can exhibit an additional Bose-Fermi glass phase [317]. Solitonic density modulations were also predicted in the opposite case of a majority fermionic system [318].

Later on, the treatment of Bose-Fermi mixtures as a Luttinger liquid of polarons was put on a more stable footing [319] and extended to also cover arbitrary commensurate mixtures [320]. Finally, the phase diagram was amended by the discovery of a supersolid phase that can appear for imbalanced mixtures in an optical lattice [321].

Different from the Hubbard-type models and Luttinger liquid approaches used in the references mentioned above, already in 2004 Miyakawa et al. employed a Green's function approach to show that homogeneous 1D Bose-Fermi mixtures exhibit a Peierls

instability for perturbations with wave vector $k \approx 2k_F$ (see Section 1.6) leading to a density modulated ground state even without a lattice potential [322].

In this chapter I study a one-dimensional Bose-Bose mixture of a Tonks-Girardeau gas immersed into a Bose-Einstein condensate. I describe a novel self-pinning transition in which, similarly to the pinning transition described in Section 6.1, the Tonks-Girardeau gas undergoes a transition to a crystal-like Mott state with regular spacing between the atoms, but without any externally imposed lattice potential. I consider an initially homogeneous, heavily imbalanced situation where the BEC is a lot larger than the TG gas. The resulting state shows similarities to the gapped pairing phase and the modulated ground state mentioned above, but to the best of my knowledge it has not been described elsewhere, particularly also in combination with the analytical results presented here.

I develop an effective model that accurately describes the system in the pinned insulator state both at zero temperature and for a finite temperature of the immersed component and which allows us to derive the critical temperature of the transition. After a brief introduction of the model, the self-pinned state and the situation at finite temperature, I study the phase transition both at zero temperature and for a finite temperature of the immersed component as a function of the interspecies interaction in Publication [3].

Since the immersed component is considered in the Tonks-Girardeau limit, the resulting densities found in the mixture are identical to an equivalent Bose-Fermi mixture due to the Bose-Fermi mapping theorem. However, as I demonstrate in the publication, the TG gas has the benefit of showing signatures of the phase transition in observables like the momentum distribution that are easily accessible in cold atom experiments. Details concerning finite size effects, the energy functional of the system, the spectrum of the Tonks-Girardeau gas, and the derivation of the critical temperature for the pinning transition are presented in the accompanying supplemental material. The chapter concludes with considerations regarding the requirements for an experimental observation of the self-pinning transition and an outlook towards future work.

7.2 Model

We consider a small system of N atoms in one dimension, described by a full many-particle wave function $\Phi(\mathbf{x} = x_1, x_2, \dots, x_N)$, which is immersed into a Bose-Einstein condensate comprised of N_c atoms and described by a macroscopic wave function $\psi(x)$ in the mean-field limit. Assuming weak interactions between the immersed atoms and the condensate atoms, we can describe the interspecies interaction by a simple density coupling of strength g_m , leading to the coupled evolution equations

$$i\dot{\psi}(x) = \left[-\frac{1}{2} \frac{\partial^2}{\partial x^2} + g_m |\Phi|^2 + g_c |\psi|^2 \right] \psi(x) \quad (7.1a)$$

$$i\dot{\Phi}(\mathbf{x}) = \left[\sum_l -\frac{1}{2} \frac{\partial^2}{\partial x_l^2} + V(x_l) + g_m |\psi|^2 + V_{\text{int}} \right] \Phi(\mathbf{x}), \quad (7.1b)$$

where for simplicity we have set \hbar and all masses equal to one. The immersed atoms are interacting via an intraspecies coupling $V_{\text{int}} = g \sum_{k < l}^N \delta(|x_k - x_l|)$ of strength g and g_c describes the intraspecies coupling within the condensate. The immersed component is trapped in a box potential of width L with $V(x) \equiv 0$ for $|x| \leq L/2$ and $V(x) \equiv \infty$ otherwise and the condensate is assumed to be in free space with a homogeneous density $n_c \equiv N_c/L_c = \mu_0/g_c$.

Throughout this chapter we assume the Tonks-Girardeau limit $g \rightarrow \infty$ for the immersed component, as it allows one to solve Eq. (7.1b) even for larger particle numbers N , thanks to the Bose-Fermi mapping theorem (see Section 1.6). At zero temperature, the density of the TG gas, which is needed for the coupling term in Eq. (7.1a), is then simply computed as

$$\rho(x) = |\Phi(x)|^2 = \sum_{n=1}^N |\phi_n(x)|^2, \quad (7.2)$$

using the single particle eigenstates $\phi_n(x)$ with eigenenergies E_n , which are the solutions of Eq. (7.1b) with $V_{\text{int}} = 0$. The coupled Eqs. (7.1) are then solved numerically in a self-consistent fashion, using the Fourier split-step method in imaginary time for the BEC component and exact diagonalization for the single-particle Tonks-Girardeau Hamiltonian as described in Chapter 2. In this Tonks-Girardeau limit, the immersed component only exists in a pinned insulating state characterized by a gap in the energy spectrum. This state is described in detail in Publication [3] presented in the next section, but in the following I give a brief summary for the benefit of the reader.

7.2.1 Self-Pinned State

In general, for finite values of the interspecies coupling g_m the atoms in the immersed component are localized in a regularly spaced pattern in the minima of a matter-wave lattice potential, which is created in the BEC by the mutual backaction of the two components. In the regime where the overlap between neighboring pinned atoms vanishes, we can use an effective single particle description to derive an analytical model for the pinned state that provides excellent agreement with the numerically observed results.

In this model we neglect the kinetic energy of the BEC in Eq. (7.1a) and approximate its wave function as

$$\psi(x, t) = \sqrt{\frac{1}{g_c} (\tilde{\mu} - g_m |\Phi|^2)} e^{-i\tilde{\mu}t} \quad (7.3)$$

in the Thomas-Fermi limit for $g_m \ll \mu_0 L/N$ (see Section 1.4), since we consider heavily imbalanced particle numbers as well as a weak interspecies interaction. Here the density modulation only deviates slightly from the constant background value. The interaction with the immersed atoms leads to a change in the chemical potential according to $\tilde{\mu} = \mu_0 \left(1 + \frac{g_m N}{g_c N_c}\right)$.

Substituting Eq. (7.3) into Eq. (7.1b) leads to the Hamiltonian for the effective single particle description (see Refs. [323–328] for similar effective models in the context

of polaron physics)

$$\hat{H}'_1 = -\frac{1}{2} \frac{\partial^2}{\partial x^2} - \frac{g_m^2}{g_c} |\phi_1(x)|^2, \quad (7.4)$$

where the ground state energy is shifted by a constant term $E'_1 = E_1 - \frac{g_m}{g_c} \tilde{\mu}$. This nonlinear Hamiltonian has a well-known soliton-like solution of inverse width a_0 of the form [329]

$$\phi_1(x) = \sqrt{\frac{a_0}{2}} \frac{1}{\cosh(a_0 x)} \quad \text{with} \quad a_0 = \frac{g_m^2}{2g_c} \quad (7.5)$$

and $E'_1 = -a_0^2/2$.

The model does not take into account the energies needed by the BEC to keep the immersed atoms from dispersing and by the immersed atoms to displace the BEC density. Considering these effects leads to a reduction $a_{\text{pin}} < a_0$ in the wave function peak height of the immersed atoms and correspondingly to a reduction in the extent of the BEC density modulation. By minimizing the energy functional for the total system energy (see Supplemental Material of Publication [3]) it is possible to find the closed expression

$$a_{\text{pin}} = a_0 \frac{\sqrt{1+2\epsilon} - 1}{\epsilon} \quad \text{with} \quad \epsilon = \frac{6a_0^2}{5\tilde{\mu}} \quad (7.6)$$

in the case of moderate interaction strengths g_m , where the width of the atomic wave function and the density dip are proportional to each other.

The total energy for the coupled system of Bose-Einstein condensate and immersed gas in this pinned state is then given by

$$E_{\text{pin}} = N \left(\frac{g_m^2}{30\tilde{\mu}g_c} a_{\text{pin}}^3 + \frac{a_{\text{pin}}^2}{6} - \frac{g_m^2}{6g_c} a_{\text{pin}} \right) + \frac{\tilde{\mu}^2 L_c}{2g_c}, \quad (7.7)$$

where the expression in the bracket is the energy of a single immersed atom.

Finally, the density of the immersed component in the pinned state can then simply be written as an arrangement of single localized bright solitons

$$\rho_{\text{pin}}(x) = \frac{a_{\text{pin}}}{2} \sum_{n=1}^N \frac{1}{\cosh^2[a_{\text{pin}}(x - x_n)]} \quad (7.8)$$

at positions x_n and with inverse width a_{pin} , since deep in the pinned state the overlap between different atoms vanishes. The positions x_n are roughly given by $x_n = [n - (N+1)/2]L/N$, but if the pinned state is considered to be the result of an adiabatic ramp of the interspecies coupling from $g_m = 0$ to some final value $g_m > 0$, they can also be approximated by the maxima of their initial density in the infinite box $\rho(g_m = 0, x) = \frac{2}{L} \sum_{n=1}^N \sin^2 \left[\frac{n\pi}{L} \left(x + \frac{L}{2} \right) \right]$. In that case the x_n are determined by the odd solutions of $(2N+1) \tan(\pi z) = \tan((2N+1)\pi z)$ for $0 \leq z \leq 1$.

7.2.2 Finite Temperature

We also study the system for the case where the Tonks-Girardeau gas has a finite temperature, while assuming that the BEC is still effectively at zero temperature due to

the large difference in particle number. In that case, thermal excitations can lead to a depinning of the immersed atoms, eventually resulting in a completely delocalized thermal phase. The Bose-Fermi mapping theorem also extends to this finite temperature case and recently efficient techniques for calculating the reduced single-particle density matrix of the TG gas only using the single particle states $\phi_n(x)$ were presented in Refs. [330–332]. We also use these techniques to calculate the momentum distribution of the immersed component from the RSPDM as shown in Section 1.6. In the finite temperature case, the density of the TG gas is adjusted to

$$\rho(x) = \sum_{n=1}^{\infty} f_n |\phi_n(x)|^2, \quad \text{where} \quad f_n = \frac{1}{\exp[\beta(E_n - \mu)] + 1} \quad (7.9)$$

is the Fermi-Dirac distribution, $\beta = 1/k_B T$ and the chemical potential μ is fixed by the number of atoms according to $N = \sum_{n=1}^{\infty} f_n$.

The single impurity model can be modified to include the effect of finite temperatures by replacing $\phi_1 \rightarrow \sqrt{f_1} \phi_1$ in the Hamiltonian (7.4). Since $0 \leq f_n \leq 1$, this corresponds to an effective reduction of the interspecies coupling. The changed coupling leads to a changed energy E'_1 which, in turn, results in a modified occupancy f_1 and so on. It is therefore possible to determine the resulting equilibrium value f_{pin} in the pinned state from the self-consistency criterion

$$f_{\text{pin}} = \frac{1}{\exp\{\beta[E(f_{\text{pin}}) - \mu(f_{\text{pin}})]\} + 1}. \quad (7.10)$$

The energy term is given by the ground state energy of the effective Hamiltonian \hat{H}' of Eq. (7.4). Using the most accurate approximation presented in the Supplemental Material of Publication [3] (see the following Section 7.4), it can be calculated as

$$E(f_{\text{pin}}) = E'_1 \approx -\frac{a_0^2}{2} \frac{\sqrt{1 + 2\epsilon f_{\text{pin}}^2} - 1}{\epsilon}, \quad (7.11)$$

where $\epsilon = 6a_0^2/5\tilde{\mu}$ is calculated from the original coupling strength g_m . It is important to note that if other approximations for E'_1 , which include the reduced peak height a_{pin} , are used that they need to be evaluated for the reduced coupling strength $g_m^{\text{eff}} = g_m \sqrt{f_{\text{pin}}}$. The remaining Fermi-Dirac factors f_n , with $n \geq N + 1$, describe the non-pinned continuum states and they are required to determine the chemical potential $\mu(f_{\text{pin}})$. As they are not trapped by the matter-wave potential, their energies are well approximated by the energy spectrum of the box potential with an additional energy offset determined by the average density of the BEC. However, for better agreement with the numerical results we usually also use numerically determined eigenvalues for the continuum states. As shown in the supplemental material, the self-consistency equation is also used to estimate the critical temperature of the transition.

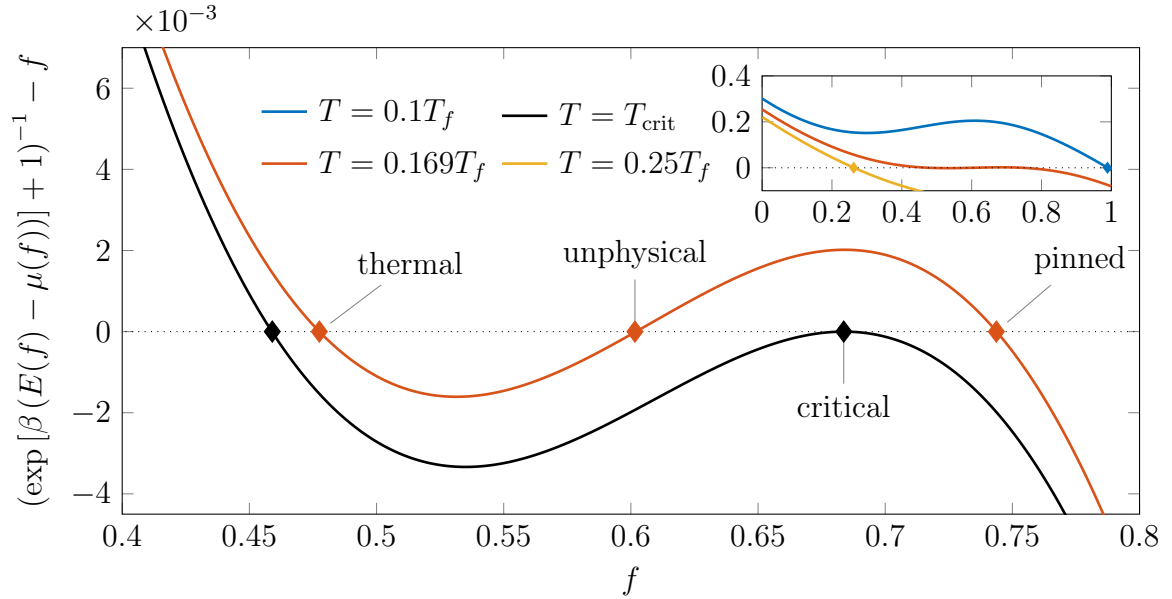


Figure 7.1: Self-consistency equation (7.10) for different temperatures and the same parameters as Fig. 2 (a) in Ref. [3]. Below and above the transition temperature there is only one solution (diamond mark) either in the pinned or thermal phase (blue and yellow curves in the inset). Close to the transition, they can exist simultaneously with one unphysical solution in between (red curve). At the critical point the unphysical solution and the pinned solution become degenerate (black curve).

We can draw an interesting connection to another well-known phase transition by defining $m := 2f_{\text{pin}} - 1 \in [-1, 1]$. The self-consistency equation for the Fermi-Dirac factors then reads

$$m := 2f_{\text{pin}} - 1 = \tanh[\beta J(m)m], \quad \text{where} \quad J(m) = -\frac{E(m) - \mu(m)}{2m}. \quad (7.12)$$

It has the same form as the consistency equation determining the equilibrium magnetization in the mean-field Ising model [333]. The parameter J , which describes the coupling strength between nearest neighbor spins in the Ising model, is a function of the ‘magnetization’ itself in our case, reflecting the backaction present in our system. In this form, also the structure of the solutions to the self-consistency equations, plotted in Fig. 7.1, becomes more clear. Deep in either the pinned or the thermal phase there is only one solution, while close to the transition there are three. One value of $f_{\text{pin}} > 2/3$ in the pinned phase, one lower value for the thermal phase and one unphysical solution in between. The transition is characterized by the point at which the pinned solution and the unphysical solution become degenerate around $f_{\text{pin}} \approx 2/3$.

7.3 Publication

The main results of this chapter are published in Reference [3]:

Tim Keller, Thomás Fogarty, and Thomas Busch
Self-Pinning Transition of a Tonks-Girardeau Gas in a Bose-Einstein Condensate
 Physical Review Letters **128**, 053401 (2022).
 Editor's Suggestion

I have derived all of the analytical results and performed all of the numerical simulations presented in the publication as well as in the supplemental material and wrote a first draft of the manuscript. All authors contributed to the discussion and interpretation of the results and to the writing of the final version.

7.4 Supplemental Material

Publication [3] is accompanied by supplemental material with details concerning finite size effects, the energy functional of the system, the spectrum of the Tonks-Girardeau gas, and the derivation of the critical temperature for the pinning transition.

7.5 Experimental Considerations

Similar to the Feshbach engine in Chapter 4, we want to go beyond the scope of the publication and explore the experimental requirements necessary to observe the self-pinned state in a physical system. Its defining quantity is the inverse width respectively peak height $a_{\text{pin}} \sim g_m^2/2g_c$ of the bright solitonic wave function. In the following we neglect the slight reduction in a_{pin} found in the actual ground state of the composite system due to the depletion of the BEC (cf. Eq. (7.6)).

The one-dimensional interspecies interaction strength can be written as [38]

$$g_m = \frac{2\pi\hbar^2 a_{12}}{\mu} \frac{1}{\pi d_{\perp}^2 \left(1 - \mathcal{C} \frac{a_{12}}{d_{\perp}}\right)} \approx 2\hbar\omega_{\perp} a_{12}, \quad (7.13)$$

where $\mathcal{C} \approx 1.46$ is a constant, the 3D interspecies scattering length is denoted by a_{12} and we need to work with the reduced mass

$$\mu = \frac{m_{\text{TG}} m_{\text{BEC}}}{m_{\text{TG}} + m_{\text{BEC}}} \quad (7.14)$$

since physical realizations of the Tonks-Girardeau component and the BEC component will likely have different masses m_{TG} and m_{BEC} respectively. The radial confinement $d_{\perp} = \sqrt{\hbar/\mu\omega_{\perp}}$ determines the degree of ‘1D-ness’ in the effectively one-dimensional setting, see Section 1.6. In the following, we will use the approximate expression $g_m \approx 2\hbar\omega_{\perp} a_{12}$, which is enough to estimate orders of magnitude.

Analogously, for the BEC interaction strength we have $g_c \approx 2\hbar\omega_{\perp} a_{11}$ with the BEC intraspecies scattering length a_{11} . In the following we give all scattering lengths in

Table 7.1: Estimates for the experimental realization of the self-pinning transition. The upper two rows use ^{87}Rb as the Tonks-Girardeau species and ^{41}K as the BEC background. In the first one, a weak interspecies interaction and weak radial confinement are assumed, while the second row uses larger values for both quantities. The third row is for a realization with fermionic ^{40}K as the TG species and ^{87}Rb for the BEC species. See text for details regarding the choice of values.

TG – BEC	\tilde{a}_{12}	\tilde{a}_{11}	$\nu_{\perp} [10^3]$	$\alpha [10^8]$	$a_{\text{pin}} [\frac{1}{\mu\text{m}}]$	$\Delta x [\mu\text{m}]$	$\frac{\Delta E}{2\pi\hbar} [\text{Hz}]$	$T_{\text{crit}} [\text{nK}]$
$^{87}\text{Rb} - ^{41}\text{K}$	75	65	12.5	0.94	0.49	1.84	14	0.11
$^{87}\text{Rb} - ^{41}\text{K}$	163	65	70.7	25.14	13.16	0.07	10 064	80.5
$^{40}\text{K} - ^{87}\text{Rb}$	-189	100.4	24	3.43	1.80	0.51	407	3.3

units of the Bohr radius a_0 according to $a_{ij} = \tilde{a}_{ij}a_0$, all masses in units of $m = \tilde{m}m_u$ and we assume identical radial trapping for both species in units of $\omega_{\perp} = 2\pi \times \nu_{\perp}$ Hz. This gives

$$a_{\text{pin}} = \frac{g_m^2}{2g_c} \frac{m_{\text{TG}}}{\hbar^2} = \frac{\tilde{a}_{12}^2 \nu_{\perp} \tilde{m}_{\text{TG}}}{\tilde{a}_{11}} \frac{2\pi \text{Hz} a_0 m_u}{\hbar} \approx 5.2354 \times \frac{\alpha}{10^9} \mu\text{m}^{-1} \quad (7.15)$$

for the characterizing quantity of the system a_{pin} , where we have defined the dimensionless parameter

$$\alpha := \frac{\tilde{a}_{12}^2 \nu_{\perp} \tilde{m}_{\text{TG}}}{\tilde{a}_{11}}. \quad (7.16)$$

In the physical system, the strength of the pinning is therefore enhanced by large interspecies scattering lengths \tilde{a}_{12} , strong radial confinement ν_{\perp} , large mass m_{TG} of the immersed component as well as small BEC intraspecies scattering lengths \tilde{a}_{11} . Using the bright solitonic wave function of the effective model for the calculation, this means that a single pinned impurity has an extent on the order of

$$\Delta x = \frac{\pi}{a_{\text{pin}} \sqrt{12}} \approx 1.7322 \times \frac{10^8}{\alpha} \mu\text{m}. \quad (7.17)$$

The size of the energy gap in the pinned state is on the order of $\Delta E \sim |E'_1|$ [3] which gives

$$\frac{\Delta E}{2\pi\hbar} = \frac{\hbar a_{\text{pin}}^2}{4\pi m_{\text{TG}}} \approx 1.3852 \times \frac{\alpha^2}{10^{13} \tilde{m}_{\text{TG}}} \text{Hz}. \quad (7.18)$$

Finally, a good estimate of the critical temperature is given by [3]

$$T_{\text{crit}} \approx \frac{\Delta E}{6k_{\text{B}}} \approx 1.1080 \times \frac{\alpha^2}{10^{15} \tilde{m}_{\text{TG}}} \text{nK}. \quad (7.19)$$

In Table 7.1 we calculate exemplary values using ^{87}Rb as the TG species and ^{41}K as the background BEC. The mixture is found to be miscible up to $a_{12} \approx 75 a_0$ but the system can also be studied at interspecies scattering lengths of e.g. $a_{12} \approx 163$

a_0 [249, 250]. Varying the radial confinement between 12.5 kHz as in the realization of the pinning transition in an optical lattice potential [230] and 70.7 kHz as in the first realization of a 1D gas in the Tonks-Girardeau regime [334], we find a range of resulting system parameters that seems to be favorable for experimental detection. In an intermediate regime, the spatial extent of the pinned impurities is even resolvable by optical means. However, for this mixture it is not clear how tuning the Rubidium intraspecies scattering length from the BEC value of $a_{22} \approx 100 a_0$ [249] to the TG value of $a_{22} \approx 261 a_0$ [230] affects the interspecies scattering length.

Another effect that needs to be taken into account is the reduction in intraspecies interaction strength for both components caused by the attractive effective interaction mediated via the immersion process. On the mean-field level and for balanced Bose-Bose mixtures this effect can be estimated to be [27, 335]

$$a_{ii}^{\text{eff}} = a_{ii} \left(1 - \frac{m_{\text{BEC}} m_{\text{TG}}}{4\mu^2} \frac{a_{12}^2}{a_{11} a_{22}} \right). \quad (7.20)$$

It is not clear if this effect is as pronounced in the heavily imbalanced mixture we are studying, but using the numbers for the $^{87}\text{Rb} - ^{41}\text{K}$ mixture shows that these mediated interactions can easily reduce the intraspecies interaction of the immersed component from the Tonks-Girardeau regime back to regular BEC levels and even lead to an effectively attractive intraspecies interaction, possibly resulting in a mediated collapse similar to Ref. [291].

For this reason, it might be better to use a Bose-Fermi mixture instead, with the fermionic component assuming the role of the TG gas. The atomic densities are identical according to the Bose-Fermi mapping theorem and since we are dealing with a density-type coupling, the resulting physics should also be the same. However, the signature of the self-pinning transition in the immersed components momentum distribution (cf. Fig. (3) in Publication [3]) will likely be lost due to the different momentum distributions in the bosonic and fermionic case.

The third row in Table 7.1 shows exemplary values for a mixture of fermionic ^{40}K and bosonic ^{87}Rb that can be realized in the lattice experiment of Prof. Tilman Esslinger at ETH Zurich [269]. The large and attractive interspecies scattering length $\tilde{a}_{12} \approx -189$ [336] is not only beneficial for observing a strongly pinned state but also allows studying the system in inhomogeneous trapping potentials as the immersed atoms are now attracted to the places of highest density in the trap center, instead of being repelled towards the trap edges. Rubidium is considered at the usual value of $\tilde{a}_{11} \approx 100.4$ [101] for the intraspecies scattering length. At ETH, the radial confinement can be increased up to $\nu_{\perp} \approx 50 \times 10^3$ [336], but already above the value of $\nu_{\perp} \approx 24 \times 10^3$ shown in Table 7.1 the same order of magnitude for the energy gap of $\Delta E/2\pi\hbar \approx 400$ Hz as in Ref. [230] for the pinning transition in a lattice can be achieved.

Overall, for both mixtures the rather low values of T_{crit} might be problematic to achieve, particularly in the fermionic case. Regarding the trapping potentials, a 3D homogeneous Bose-Einstein condensates in a box potential was first realized in Ref. [337] and particularly in one dimension, using digital micromirror devices, it is possible to create nearly arbitrary potential landscapes for neutral cold atoms [338], including the box potentials used in this chapter [339].

7.6 Conclusion & Outlook

I have identified and characterized a novel self-pinning phase transition of a Tonks-Girardeau gas immersed into a Bose-Einstein condensate from a superfluid state to a gapped Mott insulator state, without the need for an externally imposed lattice structure. I have developed an effective model that is able to accurately describe the system in the pinned phase over a wide range of parameters, both if the TG gas is at zero temperature and at finite temperature, where the pinned phase is unstable against thermal fluctuations. Finally, I have shown that a signature of the transition can be observed in the momentum distribution of the immersed component and that the required parameter regimes are within reach of experimentally available Bose-Bose and Bose-Fermi mixtures.

Regarding future work, the self-pinned state and its simple yet accurate description in the effective model opens up a plethora of new research directions, addressed in the following subsections. Obviously, since we have only considered equilibrium situations, it would be interesting to study the dynamics of the system, following e.g. ramps or quenches of both interspecies interaction and temperature, but also to study how the pinned TG atoms interact, mediated by the BEC, after for example one or several of them are given momentum kicks.

7.6.1 Phonons

Most importantly, the self-pinned state constitutes a periodic, crystal-like structure that simultaneously supports phonon-like excitations due to the non-rigid nature of the pinning lattice created in the BEC density. Phonons are a crucial feature of solid state physics. Neutral atoms in optical lattice potentials are commonly used as quantum simulators of such solid state systems, thanks to their high degree of controllability, their accessible length and time scales as well as their purity [22–25]. But since optical lattice potentials are infinitely stiff, it was not possible to also include collective phonon-like excitations in such quantum simulations until now. Only last year, a realization of an optical lattice with ‘sound’, i.e. phonons, was reported for a BEC coupled to an optical cavity in Ref. [26]. The self-pinned state adds a new possibility for studying phonon-like excitations in condensed matter simulators.

7.6.2 Symmetry Breaking & Supersolidity

Then, there are open questions in regard to the symmetry breaking mechanism of the transition and also the question of supersolidity [340, 341] in the system. In the publication, the self-pinning transition was seeded by the Friedel oscillations seen in the TG gases density in a box for $g_m = 0$ [342]. In the thermodynamic limit $N \rightarrow \infty$, while fixing the density $N/L \equiv \text{const.}$, these oscillations disappear, but still the system should be self-pinned as it allows the system to lower its energy. Similarly, if the Tonks-Girardeau gas is studied on a 1D ring with periodic boundary conditions, the resulting density in the non-interacting case is perfectly flat, even for finite N , but the same energy argument holds. Therefore, it seems that there should be a continuous symmetry being broken by the transition. Namely, the one with respect to the relative phase of

the pinned state on the ring, while the atomic distribution should be equidistant, like the one studied in the paper, for any relative phase from a simple entropy point of view.

In the publication, we have studied the system in a heavily imbalanced regime $N_c \gg N$ where the density modulation imprinted onto the BEC in the pinned state is only on the order of a few percent of its homogeneous background and where the TG gas atoms can be regarded as individual impurities, as the Thomas-Fermi approximation used for our effective model works particularly well in that case. Therefore, while we have a superfluid BEC with a crystal-like density modulation, the effect is probably too small in order to rightfully call it a supersolid state. Nonetheless, this does not exclude the possibility of observing a true supersolid state in other parameter regimes of our system, similar to the ones predicted for Bose-Fermi mixtures [321].

In fact, the self-pinned state is reminiscent of the supersolid states observed in one-dimensional dipolar BECs [343, 344] and the roton-like instability observed by Miyakawa et al. in the spectral function of a 1D Bose-Fermi mixture [322] might already hint towards the Higgs- and Goldstone-like nature of excitations in the system. Such collective oscillations of the density modulation amplitude and the phase of the crystal structure respectively, e.g. relative to its position on a ring, are a necessary condition for the existence of a supersolid, as has been shown both theoretically [345–348] in connection with aforementioned dipolar BECs and also experimentally [349–352].

A helpful tool for answering these questions might be the stochastic projected Gross-Pitaevskii equation (SPGPE) mentioned already in the outlook of Chapter 4 as a way of introducing a natural symmetry-breaking mechanism. Furthermore, the ‘mean-field Tonks-Girardeau’ model introduced by Kolomeisky et al. in Ref. [353] might be useful for studying larger system sizes beyond numerical tractability. It does not reproduce the right coherence and energy of the system, but gives the correct density, which is the quantity we need for the coupling term. It seems that the $|\phi|^4$ term appearing in this model, when incorporated into our effective nonlinear model for the pinned state, leads to a quantum droplet type equation just with one order of magnitude higher in ϕ compared to the $|\phi|^3$ appearing in the Lee-Huang-Yuang correction [282, 354]. This might explain the self-stabilizing nature of the pinned state. Furthermore, very recently Settino and coworkers presented a method for the exact calculation of the Tonks-Girardeau gases spectral function in Ref. [355]. Observing a roton minimum-like structure (see Fig. 1.2) in the spectral function, particularly around a wave vector $k \approx 2k_F$, might provide evidence both for the Peierls nature of the transition and for the question of supersolidity [356].

7.6.3 Quantum Magnetism & FFLO Superconductor

Going beyond the setup presented here, by adding a second immersed component, for example with the opposite sign of the coupling strength g_m as illustrated in Fig. 7.2, it might be possible to study another important topic in quantum simulation, which is the realization of quantum magnetism with cold atoms. First experiments were successful using Fermi gases [357], ion chains [358, 359] and Bose gases in tilted optical lattices [360]. By shaking the lattice potential, it is possible to create artificial gauge fields that have the same effect on the neutral atoms as an external magnetic field has on

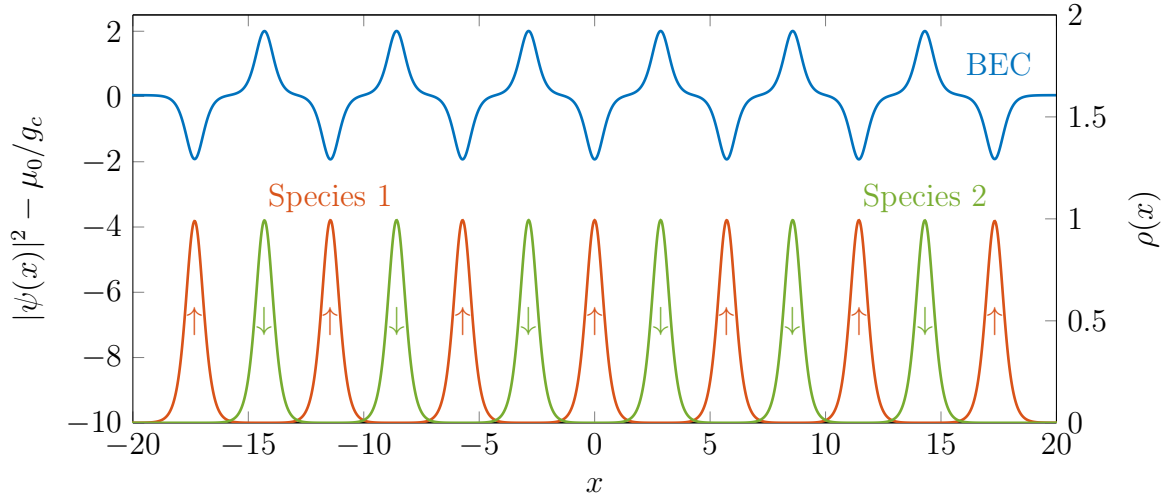


Figure 7.2: A possible realization of quantum magnetism akin to an antiferromagnetic spin chain by immersing a second TG gas into the BEC. An alternating pattern made from atoms of both immersed species emerges. In total we have $N_{\uparrow} = 7$ atoms of species 1 and $N_{\downarrow} = 6$ atoms of species 2. They are interacting with the BEC with equal but opposite coupling strengths $g_m^{\uparrow} = 2$ and $g_m^{\downarrow} = -2$. The only interaction between TG species is the one mediated via the BEC. Other parameters are $\mu_0 = 200$ and $g_c = 1$.

charged particles [361]. More recent proposals include the realization of a variety of spin models such as the XYZ model with bosons carrying orbital angular momentum [362]. Furthermore, there have also been proposals showing that strongly-interacting multicomponent gases in 1D constitute a spin-chain model that allows one to realize quantum magnetism without a lattice potential [363–365], similar to our case, and this has already been used to experimentally observe a small antiferromagnetic Heisenberg chain [366].

Having a second immersed component might also allow studying a peculiar superconducting phase known in condensed matter physics as FFLO or Fulde-Ferrell-Larkin-Ovchinnikov state, see e.g. Ref. [367] for a review. In the Bardeen-Cooper-Schrieffer theory of superconductivity, the phenomenon is explained by the formation of Cooper pairs of opposite spin and momentum, whose total momentum vanishes, resulting in a homogeneous spin density. In 1964, Fulde and Ferrell [368] as well as Larkin and Ovchinnikov [369] pointed out that in the presence of a magnetic field also superconducting states made of pairs with non-vanishing total quasi-momentum \mathbf{q} are possible. These FFLO states are characterized by a modulation of the spin density $\sim \cos(\mathbf{q} \cdot \mathbf{r})$. After a decades-long search by many research groups, Kinjo et al. reported the first measurement of a spin density modulation in strontium ruthenate as a direct evidence of the long-sought FFLO state in April 2022 [370].

Furthermore, Singh and Orso already showed in Ref. [371] how immersing spin-imbalanced fermions in the FFLO state into a bosonic system enhances the visibility of the FFLO state while inducing density modulations in the bosonic background, similar to our case.

Chapter 8

Fermionization of a One-Dimensional Bose Gas Immersed into a BEC

In this chapter I study the self-pinning transition away from the Tonks-Girardeau limit for finite intraspecies repulsion. The results will be available as an arXiv preprint shortly and it is planned to submit it for publication to SciPost Physics.

8.1 Introduction

The phase transitions introduced in this thesis so far have been continuous or second-order transitions. First-order or discontinuous transitions are a lot less common in cold atomic systems. Such transitions are characterized by metastable states in which a system can remain even after crossing the transition [372] and there is a growing interest in the form of proposals for cold atom quantum simulators of the early universe [373, 374], which might be able to investigate the ‘fate of the false vacuum’ [375], i.e. the decay from a metastable state to the true ground state. Metastable states also give rise to hysteresis and these effects associated with discontinuous phase transitions have already been observed in cold atom experiments, for example for an ultracold atomic gas in a double-well potential [376], in spinor BECs [377] and in a driven 1D optical lattice [378].

Similar to the one-dimensional Bose-Fermi mixtures introduced in the previous chapter, 1D Bose-Bose mixtures have also seen considerable interest, in particular over the past twenty years, and detailed reviews can be found in Refs. [87, 284]. Associating a ‘pseudo-spin’ $\frac{1}{2}$ with such systems, representing the two components, it has been shown that they can support spin-waves [379, 380] and also develop a spontaneous population imbalance, an equivalent of ferromagnetism [381, 382], which is suppressed at finite temperatures [383]. Eisenberg and Lieb showed that in general the ground-state of such interacting bosons with spin is always fully polarized, i.e. ferromagnetic [384]. Furthermore, they can be used to demonstrate a hallmark effect in 1D electronic systems, which is the separation of single-particle spin and charge excitations into two distinct collective branches as a result of the dimensionality [385].

The Luttinger liquid approach predicts the same phenomena of collapse or pairing for attractive intercomponent interactions as in 1D Bose-Fermi mixtures, depending on

the density regime and intracomponent interactions [309, 386], while for repulsive intercomponent interactions the same miscibility criterion as in the 3D case (see Section 6.2) determines the regime of phase separation [284]. Furthermore, exact solutions have been found for a 1D Bose-Bose mixture on a ring with equal densities and identical intraspecies and interspecies interaction strengths [387] and similar to Bose-Fermi mixtures, a supersolid state was also predicted for weak interspecies but nearly hard-core intraspecies repulsion in a balanced, harmonically trapped Bose mixture with densities incommensurate with the additional lattice potential [388].

In the few-atom regime, a repulsive binary Bose mixture is characterized by six different limiting cases of either vanishing ('BEC limit') or infinite ('TG limit') interactions [389]. Next to a phase separated state and the different combinations of BEC and TG limit, there are also the 'composite fermionization' regime [390] ($g_{ii} \rightarrow 0$, $g_{ij} \rightarrow \infty$) and 'full fermionization' ($g_{ii}, g_{ij} \rightarrow \infty$), i.e. a single-component Fermi gas equivalent. Finally, more recent developments include the extension of the famous droplets in 3D Bose-Bose mixtures, stabilized purely by quantum fluctuations, to the one-dimensional case both at zero temperature [391, 392], in the presence of spin-orbit coupling [393], and at finite temperature [394]. There, the self-bound droplets are also predicted to have a bright solitonic shape, similar to the states found in our system [395]. Particularly, for imbalanced mixtures like the one studied in this chapter, similar structures in the form of composite 'bright-gray' solitons [396] or double domain-wall solitons [397] have been predicted.

In this chapter I first briefly introduce the model, which is identical to the previous chapter, but now studied away from the Tonks-Girardeau limit for finite intraspecies interactions $0 < g < \infty$. In this case the immersed component can persist in a superfluid state, separated from the pinned state by a first-order phase transition, and I expand the effective model to capture this behavior, while comparing it to the numerical results for the energy and density. I numerically map out the phase diagrams for $N = 2$ and $N = 3$ atoms in the immersed component as a function of their coherence and derive an analytical approximation to the phase transition line before concluding the chapter with an outlook to future work.

8.2 Model

Similar to the previous chapter, we consider a strongly imbalanced two-component quantum gas in a quasi-one-dimensional setting. The majority component is given by a Bose-Einstein condensate of N_c particles, described in the mean-field limit by a macroscopic wave function $\psi(x)$. The minority component immersed into the BEC consists of $N \ll N_c$ particles described by a full many-particle wave function $\Phi(\mathbf{x} = x_1, x_2, \dots, x_N)$. The system is studied at zero temperature and therefore we can describe all interactions by point-like pseudo-potentials that only depend on the interspecies and intraspecies scattering lengths. We model the interactions between the two components by a simple density coupling, which is valid when the interspecies

interaction is assumed to be weak. This leads to the coupled Schrödinger equations

$$i\dot{\psi}(x) = \left[-\frac{1}{2} \frac{\partial^2}{\partial x^2} + g_m |\Phi|^2 + g_c |\psi|^2 \right] \psi(x), \quad (8.1a)$$

$$i\dot{\Phi}(\mathbf{x}) = \left[\sum_{l=1}^N -\frac{1}{2} \frac{\partial^2}{\partial x_l^2} + g_m |\psi|^2 + g \sum_{k<l}^N \delta(|x_k - x_l|) \right] \Phi(\mathbf{x}), \quad (8.1b)$$

where for simplicity we have set \hbar and all masses equal to one. The main difference to Chapter 7 is the finite intraspecies repulsion $0 < g < \infty$, in contrast to the Tonks-Girardeau limit $g \rightarrow \infty$ considered there. As a result, the line density of the immersed component is now calculated by tracing out all but one atom from the full many-particle wave function

$$\rho(x) \equiv |\Phi(x)|^2 = \int dx_2 \dots dx_N |\Phi(x, x_2, \dots, x_N)|^2. \quad (8.2)$$

The intraspecies interaction strengths in the minority and majority component are labeled g and g_c respectively and g_m describes the interspecies coupling strength. The condensate is assumed to be in free space with an average density $n_c \equiv N_c/L_c = \mu_0/g_c$, whereas the immersed component is confined to a box potential of width L with $V(x) \equiv 0$ for $|x| \leq L/2$ and $V(x) \equiv \infty$ otherwise.

8.3 Superfluid State

While in the Tonks-Girardeau limit the system is pinned for arbitrarily weak interactions with the background BEC, for finite intraspecies interaction strengths g the immersed gas can also exist in a superfluid state. In this section we study how the system transitions from the superfluid to the pinned state as a function of g . In this case, numerically solving the coupled Eqs. (8.1) for more than a few atoms in the immersed component becomes challenging and we therefore restrict our consideration to the case of $N = 2$ and $N = 3$ immersed particles. Both the BEC wave function and the many-body wave function for the immersed component are evolved in imaginary time using the Fourier split-step method as described in Chapter 2. They need to be evolved in an alternating, self-consistent fashion until the ground state of the coupled system is reached within numerical accuracy.

In the limit of vanishing intraspecies interaction $g \rightarrow 0$, the situation is equivalent to having a single immersed atom in the pinned state but with the bright soliton comprised of N atoms. Therefore, we can describe the superfluid state in this case by

$$\rho_{\text{sf}}(x) = N \frac{a_{\text{sf}}}{2} \frac{1}{\cosh^2(a_{\text{sf}} x)}, \quad (8.3)$$

where the peak height a_{sf} is obtained by replacing $a_0 \rightarrow Na_0$ at all occurrences in Eq. (7.6) according to

$$a_{\text{sf}} = Na_0 \frac{\sqrt{1 + 2N^2\epsilon} - 1}{N^2\epsilon}. \quad (8.4)$$

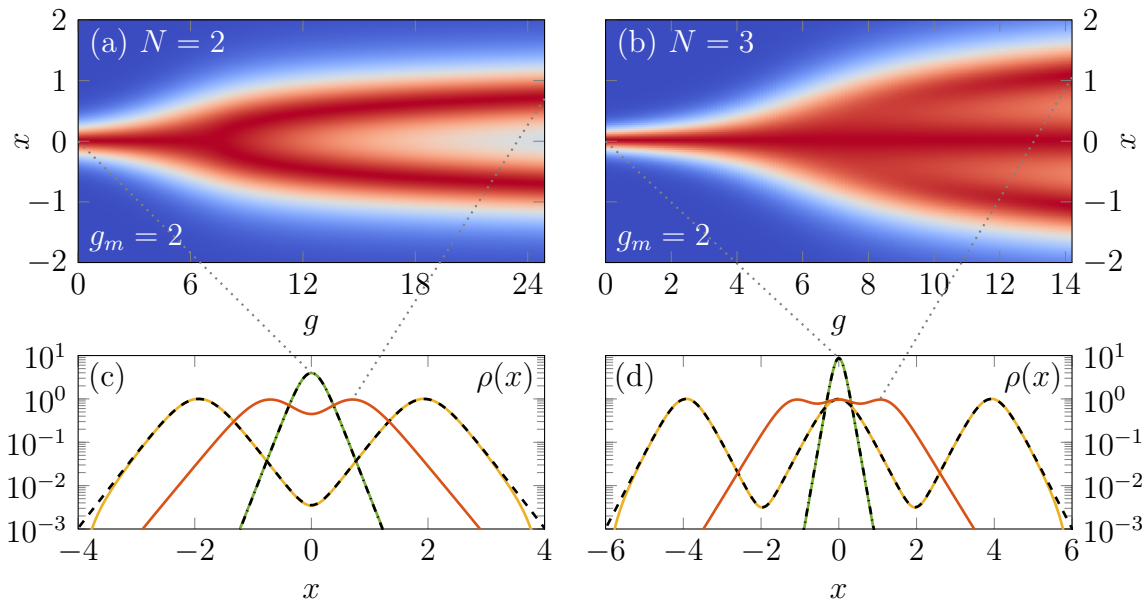


Figure 8.1: Renormalized minority component density $\rho(x)$ as a function of the intraspecies interaction strength g for a system of (a) $N = 2$ and (b) $N = 3$ particles at fixed interspecies interaction strength $g_m = 2$ and density $N/L = 1/4$. The corresponding line densities in the superfluid state at $g = 0$ (green line) and right before the transition (red lines) at $g^{\text{crit}} = 24.9$ and $g^{\text{crit}} = 14.2$ are shown to scale in (c) and (d) respectively. The yellow lines show the density in the pinned state for $g > g^{\text{crit}}$. The black dash-dotted and dashed lines show the analytical model according to Eqs. (8.3) and (7.8) respectively. Other parameters are $\mu_0 = 10^3$ ($N = 2$), $\mu_0 = \frac{2}{3} \times 10^3$ ($N = 3$) and $g_c = 1$.

Fig. 8.1 shows the minority component density at a fixed interspecies coupling $g_m = 2$, renormalized to its respective maximum at each point for clarity, for increasing intraspecies interaction g for both $N = 2$ (a) and $N = 3$ (b). Starting from line densities at $g = 0$ that are well described by Eq. (8.3), as can be seen in panels (c) and (d), the densities begin to split in separate branches according to the number of particles and start forming depletions caused by the intraspecies repulsion. As expected, this occurs at comparatively lower values of g for $N = 3$ particles than for $N = 2$ particles. The plots show the regime between $g = 0$ and $g^{\text{crit}} = 24.9$ ($N = 2$) and $g^{\text{crit}} = 14.2$ ($N = 3$) where the transition occurs and the pinned state becomes energetically favorable in both cases. Panels (c) and (d) also show the densities right before and after the transition. The logarithmic scale used in the plots nicely demonstrates the difference between the coherent superfluid state and the insulating pinned state.

In order to obtain an approximation to the many-body wave function for finite $g > 0$, we use perturbation theory to calculate the contribution of the intraspecies interaction to the total energy. We assume a separable wave function

$$\Phi(\mathbf{x}) = \sqrt{N} \prod_{n=1}^N \sqrt{\frac{a_{\text{sf}}}{2}} \frac{1}{\cosh(a_{\text{sf}} x_n)} \quad (8.5)$$

and calculate the expectation value of this mean-field wave function according to

$$\begin{aligned} V_{\text{intra}} &= g \sum_{k<l}^N \frac{\langle \Phi(\mathbf{x}) | \delta(|x_k - x_l|) | \Phi(\mathbf{x}) \rangle}{\langle \Phi(\mathbf{x}) | \Phi(\mathbf{x}) \rangle} = \frac{N}{2} (N-1) g \frac{a_{\text{sf}}^2}{4} \int dx \frac{1}{\cosh^4(a_{\text{sf}} x)} \\ &= N(N-1) g \frac{a_{\text{sf}}}{6}. \end{aligned} \quad (8.6)$$

The total system energy in the superfluid state then reads

$$E_{\text{sf}} = N \left[\frac{g_m^2}{30\tilde{\mu}g_c} N a_{\text{sf}}^3 + \frac{a_{\text{sf}}^2}{6} - \frac{g_m^2}{6g_c} N a_{\text{sf}} + (N-1) g \frac{a_{\text{sf}}}{6} \right] + \frac{\tilde{\mu}^2 L_c}{2g_c}, \quad (8.7)$$

where the bright soliton parameter a_{sf} minimizing the energy for finite $g > 0$ is now modified to

$$\begin{aligned} a_{\text{sf}} &= -\frac{5\tilde{\mu}}{3} \frac{g_c}{N g_m^2} + \sqrt{\frac{5\tilde{\mu}}{3} \left[1 - \frac{g_c g}{g_m^2} \left(1 - \frac{1}{N} \right) \right] + \frac{25\tilde{\mu}^2}{9} \frac{g_c^2}{N^2 g_m^4}} \\ &= N a_0 \frac{\sqrt{1 + 2N^2 \epsilon \left[1 - \frac{g_c g}{g_m^2} \left(1 - \frac{1}{N} \right) \right]} - 1}{N^2 \epsilon}, \end{aligned} \quad (8.8)$$

but using the same parameter $\epsilon = 6a_0^2/5\tilde{\mu}$ as before. This approximation only works, i.e. gives a valid inverse width $a_{\text{sf}} > 0$, for $g < g^* = \frac{N g_m^2}{(N-1)g_c}$.

Fig. 8.2 shows the energy per particle for increasing intraspecies interaction g at fixed interspecies coupling $g_m = 2$ (a) and $g_m = 3$ (b). For small values of g , the numerical values agree very well with the analytical model, both for $N = 2$ and $N = 3$, before starting to deviate and very slowly approaching the energy of the pinned state in which the energy is independent of g . As expected, the intraspecies repulsion in the bigger system of $N = 3$ is comparatively larger and leads to a lower value of g at which the system crosses the transition to the pinned state. The insets show a close-up of the phase transition point with the colored dotted lines indicating the energy of the then metastable superfluid state if g is increased beyond the transition point.

Interestingly, the matter-wave trapping potential created by the background BEC enables a first-order phase transition in which the immersed component actually reaches the asymptotic state predicted in the Tonks-Girardeau limit $g \rightarrow \infty$. This is in contrast to the fermionization process in static trapping potentials, where the system only asymptotically approaches the corresponding energy level from below, but never reaches it, as can be seen e.g. for the situation of two harmonically trapped atoms in Fig. 2.1 (a) in Chapter 2. This behavior is also reminiscent of the discontinuous nature of the 1D superfluid-supersolid phase transition in dipolar condensates in the low-density limit observed in numerical simulations [348] and recently confirmed experimentally [398]. In the thermodynamic limit however, the transition is predicted to be continuous in 1D systems and discontinuous in the 2D case [399].

The insets of Fig. 8.2 (a) show that the numerically determined energy of the pinned state is slightly larger than the analytical dashed line. This is due to the fact

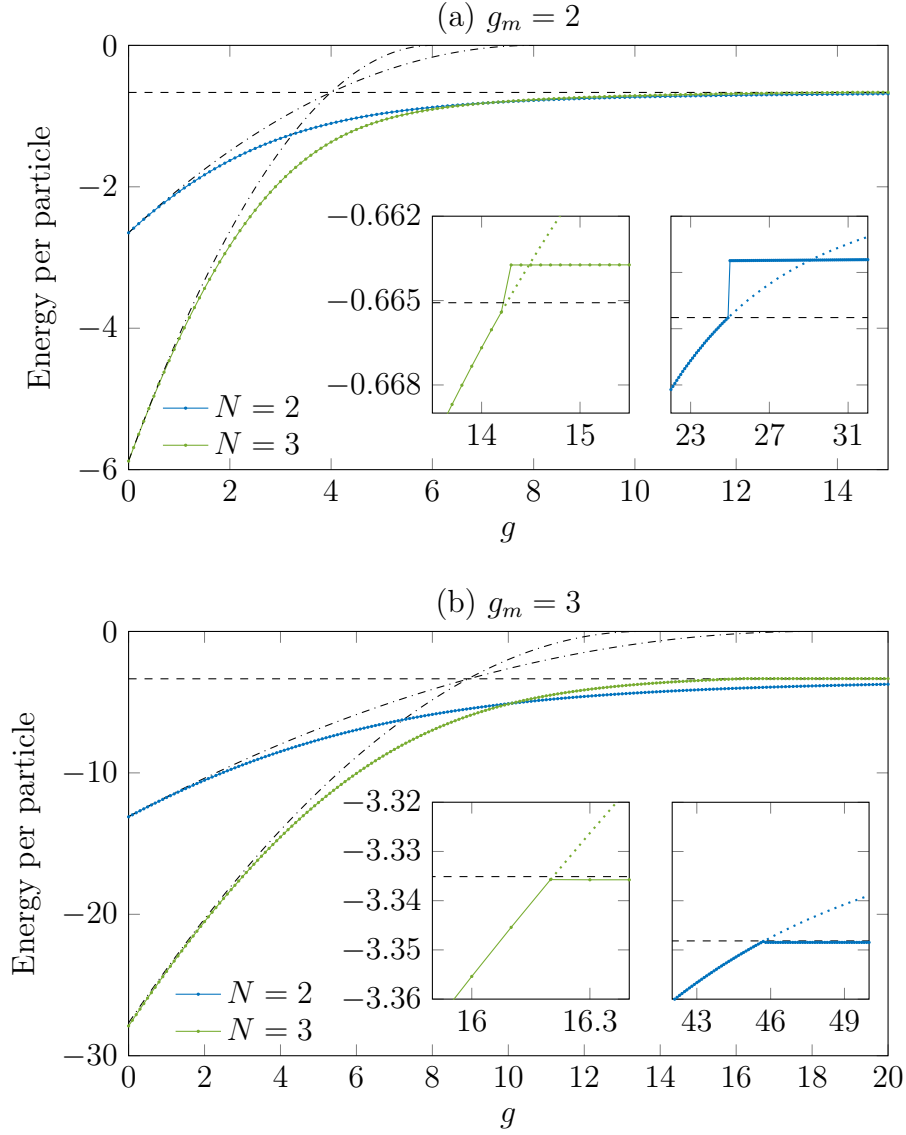


Figure 8.2: Energy per particle, adjusted for $E_{\text{BEC}} = \frac{\tilde{\mu}^2 L_c}{2g_c}$ as a function of the intraspecies interaction strength g for a system of $N = 2$ (blue line) and $N = 3$ (green line) particles at fixed interspecies interaction strength $g_m = 2$ (a) and $g_m = 3$ (b) and density $N/L = 1/4$. The dashed line shows the analytical value for the pinned state energy $E_{\text{pin}} = -0.6656$ (a) and $E_{\text{pin}} = -3.3482$ (b) for $N = 2$ while the dashed-dotted lines show the energy per particle calculated from Eq. (8.7). The inset shows a zoom of the phase transition point. The colored dotted lines indicate the energy of the metastable superfluid state if g is increased beyond the transition point. The difference in background density of the BEC of $\mu_0 = 10^3$ ($N = 2$) and $\mu_0 = \frac{2}{3} \times 10^3$ ($N = 3$) leads to the slight difference in E_{pin} visible in the insets. In both cases $g_c = 1$.

that we are numerically limited to studying a finite system and that for small values of g_m the resulting pinned states are also only weakly localized. The wave function of the immersed component is influenced by the box potential edges in that case, lifting the energy of the state in return. In contrast, for larger values of g_m like in panel (b), the immersed particles are localized stronger, therefore not experiencing an influence of the system boundaries anymore, and the numerical values lie slightly below the analytical dashed line as expected from using the closed expression in Eq. (7.6) compared to minimizing the complete energy functional.

In order to minimize these numerical finite size effects onto the results, we determine the phase transition point from the value of g for which the numerically obtained energies of the superfluid state intersect with the analytically determined value for the pinned state, i.e. $E_{\text{sf}}^{\text{num}} = E_{\text{pin}}^{\text{ana}}$. As can be seen in the insets of Fig. 8.2, this has essentially no effect for larger values of g_m , however it is necessary to obtain a clean and coherent phase transition line in the region of small g_m , where these finite size effects play a role as shown in the next section.

8.4 Phase Diagram

In order to distinguish the superfluid from the pinned phase and map out the phase diagram of the system, we calculate the coherence $C = (\max_n \lambda_n)/N$ of the immersed component. It characterizes the off-diagonal long-range order [55, 400, 401] and it is defined as the largest eigenvalue λ_n of the reduced single particle density matrix (RSPDM) divided by N , obtained from

$$\rho(x, x') = \int dx_2 \dots dx_N \Phi^*(x, x_2, \dots, x_N) \Phi(x', x_2, \dots, x_N) = \sum_n \lambda_n \varphi_n^*(x) \varphi_n(x'), \quad (8.9)$$

with the natural orbitals $\varphi_n(x)$. For the coherent superfluid state we have $C \rightarrow 1$, while in the pinned state we have $C \rightarrow 1/N$, as shown in Fig. 8.3 for fixed density $N/L = 1/4$ as a function of intraspecies repulsion g for fixed $g_m = 2$. One can see that for the larger system size the coherence drops off faster and the transition to the pinned state occurs at a smaller value of g due to the increased repulsion between the particles in the superfluid state. We adopt this slightly unconventional definition of additionally dividing by N for easier comparisons between different particle numbers. It is important to keep in mind that, as we have seen in Subsection 1.5.1, for the Tonks-Girardeau gas $\lambda_n \sim \sqrt{N}$ as $g \rightarrow \infty$. Therefore, with this definition even in what we call the superfluid state in the non-interacting case $g_m = 0$ we would have $C \rightarrow 1/\sqrt{N} \rightarrow 0$ in the thermodynamic limit, but for the finite systems studied here this is not a concern.

In Fig. 8.4 we show the full phase diagram in terms of the coherence for a system of $N = 2$ (a) and $N = 3$ (b) immersed particles for fixed density $N/L = 1/4$ as a function of both intraspecies interaction strength g and interspecies interaction strength g_m . In general, for fixed intraspecies interaction g the system transitions from the pinned insulating state to the coherent superfluid state if the interspecies interaction strength $|g_m|$ is increased until it can counteract the intrinsic repulsion of the immersed compo-

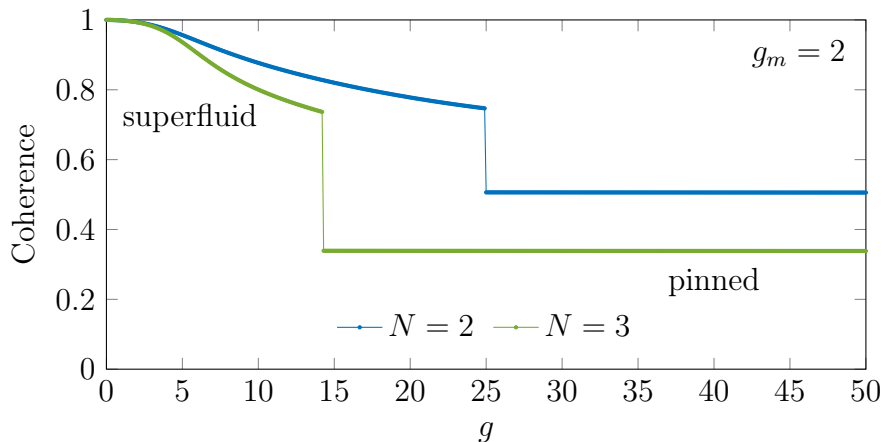


Figure 8.3: Coherence C as a function of the intraspecies interaction strength g for a system of $N = 2$ (blue line) and $N = 3$ (green line) particles at fixed interspecies interaction strength $g_m = 2$ and density $N/L = 1/4$. Other parameters are $\mu_0 = 10^3$ ($N = 2$), $\mu_0 = \frac{2}{3} \times 10^3$ ($N = 3$) and $g_c = 1$.

ment. Similarly, for fixed interspecies coupling the system transitions from superfluid to pinned if the intraspecies repulsion g is increased. This means that for the self-pinning transition the system behaves contrarily to the pinning transition in an external lattice potential, where for finite values of g the system is pinned for deep lattices but remains superfluid in shallow ones [229, 230].

For small values of $|g_m| \lesssim 1.5$ the phase diagrams both exhibit areas in the pinned region with $C > 1/N$ since the finite system size does not allow for the full separation of the particles in such weakly pinned states. In this region, the finite system size also affects the numerically obtained values of the energy in the pinned state as detailed in the previous section and shown in the insets of Fig. 8.2. Therefore, in order to obtain a clean and coherent phase transition line in this region, we have determined the critical lines in both phase diagrams by checking where the numerically obtained ground state energy in the superfluid state matches the analytical value of E_{pin} according to Eq. (7.7). The resulting deviation from the ‘true’ transition line is only marginal and quantitative in nature and should not be noticeable on the parameter scale shown in Fig. 8.4.

In general, the phase diagrams are symmetric with respect to the sign of the coupling parameter g_m , as was the case in the previous Chapter 7. This is a result of the homogeneous BEC density and is also reflected in the fact that our effective model only depends on g_m^2 . For an inhomogeneous background gas the phase diagrams are not symmetric in general, as only attractive couplings $g_m < 0$ might lead to a stable trapped state while repulsive couplings $g_m > 0$ commonly result in phase separation in that case.

In order to obtain an estimate for the phase transition line, we consider the limit $\tilde{\mu} \rightarrow \infty$ resp. $\epsilon \rightarrow 0$ in which we can neglect the energetic cost of deforming the BEC in Eqs. (7.7) and (8.7). In that case we have

$$a_{\text{pin}}(\epsilon \rightarrow 0) = a_0 \quad \text{and} \quad a_{\text{sf}}(\epsilon \rightarrow 0) = Na_0 - \frac{g}{2}(N-1) \quad (8.10)$$

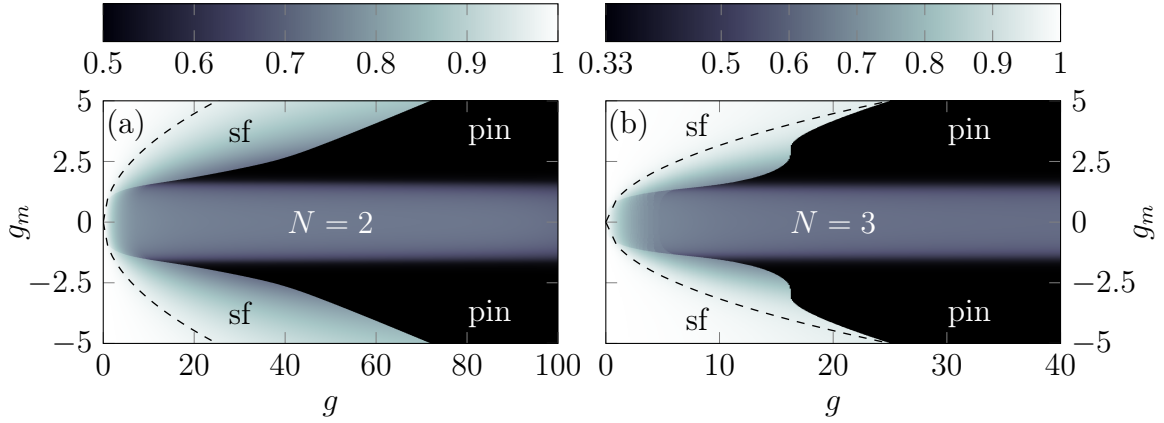


Figure 8.4: Phase diagram of the system for (a) $N = 2$ and (b) $N = 3$ as a function of intraspecies interaction g and interspecies interaction g_m for fixed density $N/L = 1/4$, exhibiting both a superfluid (sf) and pinned (pin) state of the immersed component. The colormap shows the value of the coherence C while the dashed line indicates $g_m^2 = g_c g$. The shaded area between $|g_m| \lesssim 1.5$ with $C > 1/N$ is a result of the finite system size (see text for details). Other parameters are $\mu_0 = 10^3$ ($N = 2$), $\mu_0 = \frac{2}{3} \times 10^3$ ($N = 3$) and $g_c = 1$.

and the energy of the pinned state reduces to $E_{\text{pin}}(\epsilon \rightarrow 0) = -Na_0^2/6$, while the energy of the superfluid state becomes

$$E_{\text{sf}}(\epsilon \rightarrow 0) = N \frac{a_{\text{sf}}^2}{6} - \frac{a_0}{3} \left[1 - \left(1 - \frac{1}{N} \right) \frac{g}{2a_0} \right] N^2 a_{\text{sf}}. \quad (8.11)$$

It is now easy to check that by choosing

$$g = 2a_0 = \frac{g_m^2}{g_c} \quad (8.12)$$

we further have that also $a_{\text{sf}}(\epsilon \rightarrow 0, g = 2a_0) = a_0$ and that at this point the energies of the superfluid and pinned state are identical, $E_{\text{sf}} = E_{\text{pin}}$, indicating the point where the phase transition occurs. Rewriting the above choice of g as

$$g_m^{\text{crit}} = \pm \sqrt{g_c g} \quad (8.13)$$

shows that the criterion coincides with the miscibility criterion for a 3D two-component BEC [27] and also with a stability criterion for a Bose-Bose mixture derived by Cazalilla and Ho in the Luttinger liquid framework [309]. Remarkably, Eq. (8.13) does not depend on the number of particles N and Fig. 8.2 shows that the intersection point of the analytic curves for E_{sf} and E_{pin} agrees very well with the predicted values of $g^{\text{crit}} = 4$ for $g_m = 2$ [see Panel (a)] and $g^{\text{crit}} = 9$ for $g_m = 3$ [see Panel (b)] with $g_c = 1$ in both cases. Even for the largest values of $|g_m| = 5$ and correspondingly the largest values of ϵ considered in this thesis, the actual intersection point for the model curves differs less than 5% from the analytical criterion, i.e. $g^{\text{crit}}(|g_m| = 5) \approx 24 < 25 = g_m^2$.

Eq. (8.13) is also shown as a dashed line in both phase diagrams in Fig. 8.4. In the $N = 2$ case it underestimates the observed numerical value of g^{crit} by a large amount, since the density of the immersed component [see Fig. 8.1 (a)] quickly starts to deviate from the ansatz we use to calculate the energy contribution from the intraspecies repulsion. For $N = 3$ the behavior is similar in the region of small g_m and small g . However, for $g \gtrsim 15$ a distinct shoulder appears in the phase transition line, drawing it closer to the analytical estimate. In this region, the larger interspecies coupling leads to a strong localization of the immersed component and the formation of the density modulation due to the intraspecies repulsion, visible in Fig. 8.1, is suppressed. In other words, the transition occurs while the line density is still well described by our bright solitonic ansatz.

We expect that in the thermodynamic limit $N \rightarrow \infty$ the phase transition line will converge to our analytical estimate in the region of small g_m . For larger g_m , the effect of $\epsilon > 0$, which we have neglected in the derivation, becomes relevant, leading to a transition from superfluid to pinned at weaker intraspecies repulsion than predicted. This is also in line with and even necessary for our observation in Ref. [3] that in the Tonks-Girardeau limit $g \rightarrow \infty$ only the pinned state exists, as the BEC is not able to compress the fermionized bosons for any value of the interaction strength g_m .

8.5 Conclusion & Outlook

I have studied how a small, initially superfluid, one-dimensional Bose gas immersed into a Bose-Einstein condensate fermionizes as a function of increasing intraspecies repulsion g and eventually reaches the insulating self-pinned state expected in the Tonks-Girardeau limit $g \rightarrow \infty$. In contrast to static trapping potentials, this asymptotic state is actually crossed and not just approached from below, leading to a first-order phase transition as a result of the matter-wave backaction. I have confirmed this behavior by numerically simulating the system for $N = 2$ and $N = 3$ immersed particles and calculating its densities, energy and coherence. I have extended the effective model presented in Chapter 7 to the superfluid state and used it to derive a phase transition line valid in the mean-field limit $N \rightarrow \infty$ and $\epsilon \rightarrow 0$, i.e. $N_c \rightarrow \infty$. Finally, I have mapped out the phase diagram as a function of interspecies and intraspecies couplings with extensive simulations for the aforementioned $N = 2$ and $N = 3$ cases. This work will be available as an arXiv preprint shortly and it is planned to submit it for publication to SciPost Physics.

Regarding future work, it would be interesting to probe the dynamics of the system by quenching or ramping either of intraspecies or interspecies interaction strengths across the phase transition lines. Furthermore, it would be beneficial to study the system for a larger number of immersed particles N in order to put the effective model to the test and also to extend the phase diagram to finite temperatures by studying the stability of the superfluid phase against thermal excitations, similar to the previous chapter. Already calculating the phase diagram for $N = 3$ particles with the Fourier split-step method using $N_{\text{grid}} = 512$ position grid points at the resolution in g and g_m presented in Fig. 8.4 (b) required on the order of 10^6 CPU hours, despite numerous optimizations. Larger systems therefore need to be studied by alternative techniques

such as world-line [402, 403] or diffusion [404, 405] Monte-Carlo methods or the density-matrix renormalization group (DMRG) [406] and particularly its continuum extension [407]. All of these techniques are also able to cover the finite temperature case and specifically the diffusion Monte-Carlo technique has already been used for studying 1D droplets in binary Bose mixtures [408, 409].

Conclusion

In this thesis, I have investigated how to control the properties of interacting quantum gases by tuning their interaction strengths. I have studied both the direct control of the volume of a single-species quantum gas via shortcuts to adiabaticity and the indirect control of superfluidity in a one-dimensional quantum gas by immersing it into a second component. The study of shortcuts also led to a separate finding in the field of quantum metrology.

My work has resulted in three papers published in peer-reviewed journals and one manuscript that is about to be submitted for publication. They are at the basis of Chapters 4, 5, 7 and 8 embedded in this thesis and I will briefly summarize them again in the following. For future directions pertinent to the different topics, the reader is referred to the respective outlook of each chapter.

Chapter 4: Feshbach engine in the Thomas-Fermi regime

I have exactly solved the dynamics of a Bose-Einstein condensate subject to a particular interaction ramp in the repulsive Thomas-Fermi regime via a scaling ansatz. This ramp constitutes a shortcut to adiabaticity for changing the condensate volume in a lossless fashion and I have shown how it enables to boost the performance of a Feshbach engine if used for the adiabatic strokes in its Otto-like cycle. Simulating the full system dynamics revealed a condensate collapse for short interaction ramps caused by a modulational instability and using a stability analysis I derived an accurate expression for the minimal ramp duration. This work has been published in *Phys. Rev. Research* **2**, 033335 (2020).

Chapter 5: Adiabatic critical quantum metrology cannot reach the Heisenberg limit even when shortcuts to adiabaticity are applied

I have derived a shortcut to adiabaticity for the quantum Rabi model in the Schrieffer-Wolff approximation and showed how it can be expressed in a local counterdiabatic form. My coworkers and I have used this shortcut as an example to demonstrate that in general no unitary transformation, including shortcuts to adiabaticity, can be used to reach the Heisenberg limit of precision in critical quantum metrology. This work has been published in *Quantum* **5**, 489 (2021).

Chapter 7: Self-Pinning Transition of a Tonks-Girardeau Gas in a Bose-Einstein Condensate

I have described a novel self-pinning phase transition in a one-dimensional two-component system, in which a strongly correlated Tonks-Girardeau gas immersed into a Bose-Einstein condensate forms a crystal-like Mott insulating state without an external lattice potential. I have accurately described this state with an effective model valid in a wide range of parameters and even if the immersed component has a finite temperature. I have derived an expression for the critical temperature beyond which thermal fluctuations destroy the pinned phase and confirmed its validity with a numerical calculation of the phase diagram. The transition can be observed in experimentally accessible observables as I have shown by calculating the momentum distribution of the immersed component. This work has been published in *Phys. Rev. Lett.* **128**, 053401 (2022) and was highlighted as an ‘Editor’s Suggestion’.

Chapter 8: Fermionization of a One-Dimensional Bose Gas Immersed into a BEC

I have extended the work on the self-pinning transition to the finite intraspecies coupling regime away from the Tonks-Girardeau limit. I have adapted the effective model to include the superfluid state that can persist in the immersed component if the interspecies coupling is able to overcome its intraspecies repulsion. I have shown that the immersed component fermionizes accompanied by a first-order phase transition from a superfluid to the insulating self-pinned state, in contrast to the asymptotic Tonks-Girardeau limit reached in static trapping potentials. I have numerically simulated this behavior for the tractable case of two and three immersed atoms and mapped out the phase diagram as a function of interspecies and intraspecies couplings in these cases. This work is planned to be submitted for publication to *SciPost Physics* and will be available as an arXiv preprint shortly.

Bibliography

- [1] T. Keller, T. Fogarty, J. Li, and Th. Busch, *Feshbach engine in the Thomas-Fermi regime*, Phys. Rev. Research **2**, 033335 (2020).
- [2] K. Gietka, F. Metz, T. Keller, and J. Li, *Adiabatic critical quantum metrology cannot reach the Heisenberg limit even when shortcuts to adiabaticity are applied*, Quantum **5**, 489 (2021).
- [3] T. Keller, T. Fogarty, and Th. Busch, *Self-Pinning Transition of a Tonks-Girardeau Gas in a Bose-Einstein Condensate*, Phys. Rev. Lett. **128**, 053401 (2022).
- [4] J. P. Dowling and G. J. Milburn, *Quantum technology: the second quantum revolution*, Phil. Trans. R. Soc. A. **361**, 1655 (2003).
- [5] M. Allen, *Physicists release ‘quantum manifesto’ for Europe*, Phys. World **29**, 10 (2016).
- [6] A. Celi, A. Sanpera, V. Ahufinger, and M. Lewenstein, *Quantum optics and frontiers of physics: the third quantum revolution*, Phys. Scr. **92**, 013003 (2016).
- [7] A. Acín, I. Bloch, H. Buhrman, T. Calarco, C. Eichler, J. Eisert, D. Esteve, N. Gisin, S. J. Glaser, F. Jelezko, S. Kuhr, M. Lewenstein, M. F. Riedel, P. O. Schmidt, R. Thew, A. Wallraff, I. Walmsley, and F. K. Wilhelm, *The quantum technologies roadmap: a European community view*, New J. Phys. **20**, 080201 (2018).
- [8] F. Binder, L. A. Correa, C. Gogolin, J. Anders, and G. Adesso, *Thermodynamics in the quantum regime: Fundamental Aspects and New Directions*, Springer (2019).
- [9] P. Steeneken, K. Le Phan, M. Goossens, G. Koops, G. Brom, C. Van der Avoort, and J. Van Beek, *Piezoresistive heat engine and refrigerator*, Nat. Phys. **7**, 354 (2011).
- [10] V. Blickle and C. Bechinger, *Realization of a micrometre-sized stochastic heat engine*, Nat. Phys. **8**, 143 (2012).
- [11] J. Roßnagel, S. T. Dawkins, K. N. Tolazzi, O. Abah, E. Lutz, F. Schmidt-Kaler, and K. Singer, *A single-atom heat engine*, Science **352**, 325 (2016).

- [12] O. Abah, J. Rosnagel, G. Jacob, S. Deffner, F. Schmidt-Kaler, K. Singer, and E. Lutz, *Single-ion heat engine at maximum power*, Phys. Rev. Lett. **109**, 203006 (2012).
- [13] J. P. S. Peterson, T. B. Batalhão, M. Herrera, A. M. Souza, R. S. Sarthour, I. S. Oliveira, and R. M. Serra, *Experimental Characterization of a Spin Quantum Heat Engine*, Phys. Rev. Lett. **123**, 240601 (2019).
- [14] Q. Bouton, J. Nettersheim, S. Burgardt, D. Adam, E. Lutz, and A. Widera, *A quantum heat engine driven by atomic collisions*, Nat. Commun. **12**, 2063 (2021).
- [15] D. Guéry-Odelin, A. Ruschhaupt, A. Kiely, E. Torrontegui, S. Martínez-Garaot, and J. G. Muga, *Shortcuts to adiabaticity: Concepts, methods, and applications*, Rev. Mod. Phys. **91**, 045001 (2019).
- [16] M. R. Lam, N. Peter, T. Groh, W. Alt, C. Robens, D. Meschede, A. Negretti, S. Montangero, T. Calarco, and A. Alberti, *Demonstration of Quantum Brachistochrones between Distant States of an Atom*, Phys. Rev. X **11**, 011035 (2021).
- [17] S. Sachdev, *Quantum Phase Transitions*, Cambridge University Press, Cambridge, England, 2nd edition (2011).
- [18] M. H. Anderson, J. R. Ensher, M. R. Matthews, C. E. Wieman, and E. A. Cornell, *Observation of Bose-Einstein condensation in a dilute atomic vapor*, Science **269**, 198 (1995).
- [19] K. B. Davis, M.-O. Mewes, M. R. Andrews, N. Van Druten, D. Durfee, D. Kurn, and W. Ketterle, *Bose-Einstein condensation in a gas of sodium atoms*, Phys. Rev. Lett. **75**, 3969 (1995).
- [20] H. E. Stanley, *Phase transitions and critical phenomena*, Clarendon Press, Oxford (1971).
- [21] M. Greiner, O. Mandel, T. Esslinger, T. W. Hänsch, and I. Bloch, *Quantum phase transition from a superfluid to a Mott insulator in a gas of ultracold atoms*, Nature **415**, 39–44 (2002).
- [22] D. Jaksch and P. Zoller, *The cold atom Hubbard toolbox*, Ann. Phys. (N. Y.) **315**, 52–79 (2005).
- [23] I. Bloch, J. Dalibard, and S. Nascimbène, *Quantum simulations with ultracold quantum gases*, Nat. Phys. **8**, 267–276 (2012).
- [24] I. M. Georgescu, S. Ashhab, and F. Nori, *Quantum simulation*, Rev. Mod. Phys. **86**, 153–185 (2014).
- [25] C. Gross and I. Bloch, *Quantum simulations with ultracold atoms in optical lattices*, Science **357**, 995–1001 (2017).
- [26] Y. Guo, R. M. Kroeze, B. P. Marsh, S. Gopalakrishnan, J. Keeling, and B. L. Lev, *An optical lattice with sound*, Nature **599**, 211–215 (2021).

-
- [27] C. J. Pethick and H. Smith, *Bose–Einstein Condensation in Dilute Gases*, Cambridge University Press, Cambridge, England (2008).
- [28] C. Cohen-Tannoudji and D. Guéry-Odelin, *Advances in atomic physics: an overview*, World Scientific (2011).
- [29] I. Bloch, J. Dalibard, and W. Zwerger, *Many-body physics with ultracold gases*, Rev. Mod. Phys. **80**, 885–964 (2008).
- [30] D. J. Griffiths and D. F. Schroeter, *Introduction to quantum mechanics*, Cambridge University Press (2018).
- [31] J. Walraven, *Elastic collisions in ultracold atomic gases*, unpublished lecture notes (2019).
- [32] J. D. Jackson, *Classical Electrodynamics*, Wiley (1999).
- [33] K. Huang, *Statistical Mechanics*, Wiley (1987).
- [34] H. Feshbach, *Unified theory of nuclear reactions*, Ann. Phys. (N. Y.) **5**, 357 (1958).
- [35] S. Inouye, M. R. Andrews, J. Stenger, H. J. Miesner, D. M. Stamper-Kurn, and W. Ketterle, *Observation of Feshbach resonances in a Bose–Einstein condensate*, Nature **392**, 151–154 (1998).
- [36] P. Courteille, R. Freeland, D. Heinzen, F. Van Abeelen, and B. Verhaar, *Observation of a Feshbach resonance in cold atom scattering*, Phys. Rev. Lett. **81**, 69 (1998).
- [37] C. Chin, R. Grimm, P. Julienne, and E. Tiesinga, *Feshbach resonances in ultracold gases*, Rev. Mod. Phys. **82**, 1225 (2010).
- [38] M. Olshanii, *Atomic scattering in the presence of an external confinement and a gas of impenetrable bosons*, Phys. Rev. Lett. **81**, 938 (1998).
- [39] L. Pitaevskii and S. Stringari, *Bose–Einstein condensation and superfluidity*, Oxford University Press (2016).
- [40] F. Dalfovo, S. Giorgini, L. P. Pitaevskii, and S. Stringari, *Theory of Bose–Einstein condensation in trapped gases*, Rev. Mod. Phys. **71**, 463 (1999).
- [41] E. P. Gross, *Structure of a quantized vortex in boson systems*, Il Nuovo Cimento **20**, 454 (1961).
- [42] L. Pitaevskii, *Vortex lines in an imperfect Bose gas*, Sov. Phys. JETP **13**, 451 (1961).
- [43] M. J. Davis and P. B. Blakie, *Critical Temperature of a Trapped Bose Gas: Comparison of Theory and Experiment*, Phys. Rev. Lett. **96**, 060404 (2006).

- [44] G. Baym and C. J. Pethick, *Ground-State Properties of Magnetically Trapped Bose-Condensed Rubidium Gas*, Phys. Rev. Lett. **76**, 6–9 (1996).
- [45] F. Dalfovo, L. Pitaevskii, and S. Stringari, *Order parameter at the boundary of a trapped Bose gas*, Phys. Rev. A **54**, 4213–4217 (1996).
- [46] L. J. O’Riordan, A. C. White, and Th. Busch, *Moiré superlattice structures in kicked Bose-Einstein condensates*, Phys. Rev. A **93**, 023609 (2016).
- [47] C. N. Weiler, T. W. Neely, D. R. Scherer, A. S. Bradley, M. J. Davis, and B. P. Anderson, *Spontaneous vortices in the formation of Bose-Einstein condensates*, Nature **455**, 948–951 (2008).
- [48] N. Bogoliubov, *On the theory of superfluidity*, J. Phys **11**, 23 (1947).
- [49] R. B. Diener, Q. Zhou, H. Zhai, and T.-L. Ho, *Criterion for Bosonic Superfluidity in an Optical Lattice*, Phys. Rev. Lett. **98**, 180404 (2007).
- [50] C. N. Yang, *Concept of off-diagonal long-range order and the quantum phases of liquid He and of superconductors*, Rev. Mod. Phys. **34**, 694 (1962).
- [51] O. Penrose and L. Onsager, *Bose-Einstein condensation and liquid helium*, Phys. Rev. **104**, 576 (1956).
- [52] M. Girardeau, E. M. Wright, and J. Triscari, *Ground-state properties of a one-dimensional system of hard-core bosons in a harmonic trap*, Phys. Rev. A **63**, 033601 (2001).
- [53] E. J. Mueller, T.-L. Ho, M. Ueda, and G. Baym, *Fragmentation of Bose-Einstein condensates*, Phys. Rev. A **74**, 033612 (2006).
- [54] A. Lenard, *Momentum distribution in the ground state of the one-dimensional system of impenetrable bosons*, J. Math. Phys. **5**, 930–943 (1964).
- [55] A. Colcelli, J. Viti, G. Mussardo, and A. Trombettoni, *Universal off-diagonal long-range-order behavior for a trapped Tonks-Girardeau gas*, Phys. Rev. A **98**, 063633 (2018).
- [56] P. Nozières. *Some Comments on Bose-Einstein Condensation*. In A. Griffin, D. W. Snoke, and S. Stringari, editors, *Bose-Einstein Condensation*, page 15–30. Cambridge University Press, (1995).
- [57] M. Imada, A. Fujimori, and Y. Tokura, *Metal-insulator transitions*, Rev. Mod. Phys. **70**, 1039–1263 (1998).
- [58] K. Byczuk, W. Hofstetter, and D. Vollhardt, *Mott-Hubbard Transition versus Anderson Localization in Correlated Electron Systems with Disorder*, Phys. Rev. Lett. **94**, 056404 (2005).
- [59] A. E. Antipov, Y. Javanmard, P. Ribeiro, and S. Kirchner, *Interaction-Tuned Anderson versus Mott Localization*, Phys. Rev. Lett. **117**, 146601 (2016).

-
- [60] T. Giamarchi, *Quantum physics in one dimension*, Clarendon Press (2003).
- [61] N. F. Mott, *The basis of the electron theory of metals, with special reference to the transition metals*, Proc. Phys. Soc. A **62**, 416 (1949).
- [62] N. F. Mott, *Metal-insulator transitions*, CRC Press (2004).
- [63] M. P. A. Fisher, P. B. Weichman, G. Grinstein, and D. S. Fisher, *Boson localization and the superfluid-insulator transition*, Phys. Rev. B **40**, 546–570 (1989).
- [64] P. W. Anderson, *Absence of diffusion in certain random lattices*, Phys. Rev. **109**, 1492 (1958).
- [65] R. E. Peierls, *Quantum theory of solids*, Oxford University Press (1955).
- [66] G. Grüner, *The dynamics of charge-density waves*, Rev. Mod. Phys. **60**, 1129–1181 (1988).
- [67] E. H. Lieb and D. C. Mattis, *Mathematical physics in one dimension: exactly soluble models of interacting particles*, Academic Press (2013).
- [68] B. Paredes, A. Widera, V. Murg, O. Mandel, S. Fölling, I. Cirac, G. V. Shlyapnikov, T. W. Hänsch, and I. Bloch, *Tonks–Girardeau gas of ultracold atoms in an optical lattice*, Nature **429**, 277–281 (2004).
- [69] T. Kinoshita, T. Wenger, and D. S. Weiss, *Local pair correlations in one-dimensional Bose gases*, Phys. Rev. Lett. **95**, 190406 (2005).
- [70] T. Kinoshita, T. Wenger, and D. S. Weiss, *A quantum Newton’s cradle*, Nature **440**, 900 (2006).
- [71] N. D. Mermin and H. Wagner, *Absence of Ferromagnetism or Antiferromagnetism in One- or Two-Dimensional Isotropic Heisenberg Models*, Phys. Rev. Lett. **17**, 1133–1136 (1966).
- [72] P. C. Hohenberg, *Existence of Long-Range Order in One and Two Dimensions*, Phys. Rev. **158**, 383–386 (1967).
- [73] V. Berezinskii, *Destruction of long-range order in one-dimensional and two-dimensional systems possessing a continuous symmetry group. II. Quantum systems*, Sov. Phys. JETP **34**, 610–616 (1972).
- [74] J. M. Kosterlitz and D. J. Thouless, *Ordering, metastability and phase transitions in two-dimensional systems*, J. Phys. C: Solid State Phys. **6**, 1181 (1973).
- [75] P. M. Chaikin, T. C. Lubensky, and T. A. Witten, *Principles of condensed matter physics*, Cambridge University Press (1995).
- [76] Z. Hadzibabic, P. Krüger, M. Cheneau, B. Battelier, and J. Dalibard, *Berezinskii–Kosterlitz–Thouless crossover in a trapped atomic gas*, Nature **441**, 1118–1121 (2006).

- [77] D. S. Fisher and P. C. Hohenberg, *Dilute Bose gas in two dimensions*, Phys. Rev. B **37**, 4936–4943 (1988).
- [78] D. S. Petrov, M. Holzmann, and G. V. Shlyapnikov, *Bose-Einstein Condensation in Quasi-2D Trapped Gases*, Phys. Rev. Lett. **84**, 2551–2555 (2000).
- [79] T. P. Simula and P. B. Blakie, *Thermal Activation of Vortex-Antivortex Pairs in Quasi-Two-Dimensional Bose-Einstein Condensates*, Phys. Rev. Lett. **96**, 020404 (2006).
- [80] E. H. Lieb and W. Liniger, *Exact Analysis of an Interacting Bose Gas. I. The General Solution and the Ground State*, Phys. Rev. **130**, 1605–1616 (1963).
- [81] E. H. Lieb, *Exact Analysis of an Interacting Bose Gas. II. The Excitation Spectrum*, Phys. Rev. **130**, 1616–1624 (1963).
- [82] M. Girardeau, *Relationship between systems of impenetrable bosons and fermions in one dimension*, J. Math. Phys. (N.Y.) **1**, 516–523 (1960).
- [83] A. Minguzzi, P. Vignolo, and M. Tosi, *High-momentum tail in the Tonks gas under harmonic confinement*, Phys. Lett. A **294**, 222–226 (2002).
- [84] M. Olshanii and V. Dunjko, *Short-distance correlation properties of the Lieb-Liniger system and momentum distributions of trapped one-dimensional atomic gases*, Phys. Rev. Lett. **91**, 090401 (2003).
- [85] W. Xu and M. Rigol, *Universal scaling of density and momentum distributions in Lieb-Liniger gases*, Phys. Rev. A **92**, 063623 (2015).
- [86] G. Zürn, F. Serwane, T. Lompe, A. Wenz, M. G. Ries, J. E. Bohn, and S. Jochim, *Fermionization of two distinguishable fermions*, Phys. Rev. Lett. **108**, 075303 (2012).
- [87] M. A. Cazalilla, R. Citro, T. Giamarchi, E. Orignac, and M. Rigol, *One dimensional bosons: From condensed matter systems to ultracold gases*, Rev. Mod. Phys. **83**, 1405–1466 (2011).
- [88] J. C. Butcher, *Numerical methods for ordinary differential equations*, John Wiley & Sons (2016).
- [89] J. Crank and P. Nicolson. *A practical method for numerical evaluation of solutions of partial differential equations of the heat-conduction type*. In *Mathematical Proceedings of the Cambridge Philosophical Society*, volume 43, pages 50–67. Cambridge University Press, (1947).
- [90] J. Weideman and B. Herbst, *Split-step methods for the solution of the nonlinear Schrödinger equation*, SIAM Journal on Numerical Analysis **23**, 485–507 (1986).
- [91] W. Bao, D. Jaksch, and P. A. Markowich, *Numerical solution of the Gross-Pitaevskii equation for Bose-Einstein condensation*, J. Comput. Phys. **187**, 318–342 (2003).

-
- [92] H. Wang, *Numerical studies on the split-step finite difference method for nonlinear Schrödinger equations*, Appl. Math. Comput. **170**, 17–35 (2005).
- [93] J. Javanainen and J. Ruostekoski, *Symbolic calculation in development of algorithms: split-step methods for the Gross–Pitaevskii equation*, J. Phys. A: Math. Gen. **39**, L179 (2006).
- [94] C. Lubich, *On splitting methods for Schrödinger-Poisson and cubic nonlinear Schrödinger equations*, Math. Comput. **77**, 2141–2153 (2008).
- [95] X. Antoine, W. Bao, and C. Besse, *Computational methods for the dynamics of the nonlinear Schrödinger/Gross–Pitaevskii equations*, Comput. Phys. Commun. **184**, 2621–2633 (2013).
- [96] G. P. Agrawal. *Nonlinear fiber optics*. In *Nonlinear Science at the Dawn of the 21st Century*, pages 195–211. Springer, (2000).
- [97] B. C. Hall et al., *Lie groups, Lie algebras, and representations: an elementary introduction*, Springer (2003).
- [98] G. Strang, *On the construction and comparison of difference schemes*, SIAM J. Numer. Anal. **5**, 506–517 (1968).
- [99] R. A. Horn and C. R. Johnson, *Matrix analysis*, Cambridge university press (2012).
- [100] W. H. Press, S. A. Teukolsky, W. T. Vetterling, and B. P. Flannery, *Numerical recipes 3rd edition: The art of scientific computing*, Cambridge University Press (2007).
- [101] M. Egorov, B. Opanchuk, P. Drummond, B. V. Hall, P. Hannaford, and A. I. Sidorov, *Measurement of s -wave scattering lengths in a two-component Bose-Einstein condensate*, Phys. Rev. A **87**, 053614 (2013).
- [102] P. Duhamel and M. Vetterli, *Fast fourier transforms: A tutorial review and a state of the art*, Signal Process. **19**, 259–299 (1990).
- [103] G. C. Wick, *Properties of Bethe-Salpeter Wave Functions*, Phys. Rev. **96**, 1124–1134 (1954).
- [104] J. W. Cooley and J. W. Tukey, *An algorithm for the machine calculation of complex Fourier series*, Math. Comput. **19**, 297–301 (1965).
- [105] J. Schloss and L. J. O’Riordan, *GPUE: Graphics Processing Unit Gross–Pitaevskii Equation solver*, J. Open Source Softw. **3**, 1037 (2018).
- [106] J. Schloss et al. *Massively parallel split-step Fourier techniques for simulating quantum systems on graphics processing units*. PhD thesis, OIST, (2019).
- [107] D. Raventós, T. Graß, M. Lewenstein, and B. Juliá-Díaz, *Cold bosons in optical lattices: a tutorial for exact diagonalization*, J. Phys. B **50**, 113001 (2017).

- [108] T. Haugset and H. Haugerud, *Exact diagonalization of the Hamiltonian for trapped interacting bosons in lower dimensions*, Phys. Rev. A **57**, 3809–3817 (1998).
- [109] F. Deuretzbacher, K. Bongs, K. Sengstock, and D. Pfannkuche, *Evolution from a Bose-Einstein condensate to a Tonks-Girardeau gas: An exact diagonalization study*, Phys. Rev. A **75**, 013614 (2007).
- [110] B. Fornberg, *Generation of finite difference formulas on arbitrarily spaced grids*, Math. Comput. **51**, 699–706 (1988).
- [111] F. J. Vesely, *Computational Physics*, Springer (1994).
- [112] Th. Busch, B.-G. Englert, K. Rzazewski, and M. Wilkens, *Two cold atoms in a harmonic trap*, Found. Phys. **28**, 549 (1998).
- [113] M. Abramowitz and I. A. Stegun, *Handbook of mathematical functions: with formulas, graphs, and mathematical tables*, Courier Corporation (1965).
- [114] T. Ernst, D. W. Hallwood, J. Gulliksen, H.-D. Meyer, and J. Brand, *Simulating strongly correlated multiparticle systems in a truncated Hilbert space*, Phys. Rev. A **84**, 023623 (2011).
- [115] L. Rammelmüller, D. Huber, and A. G. Volosniev, *A modular implementation of an effective interaction approach for harmonically trapped fermions in 1D*, arXiv e-prints, arXiv:2202.04603 (2022).
- [116] M. Born and V. Fock, *Beweis des Adiabatensatzes*, Zeitschrift für Physik **51**, 165 (1928).
- [117] X. Chen, A. Ruschhaupt, S. Schmidt, A. Del Campo, D. Guéry-Odelin, and J. G. Muga, *Fast optimal frictionless atom cooling in harmonic traps: Shortcut to adiabaticity*, Phys. Rev. Lett. **104**, 063002 (2010).
- [118] M. Demirplak and S. A. Rice, *Adiabatic Population Transfer with Control Fields*, J. Phys. Chem. A **107**, 9937–9945 (2003).
- [119] M. V. Berry, *Transitionless quantum driving*, J. Phys. A Math. Theor. **42**, 365303 (2009).
- [120] D. E. Kirk, *Optimal control theory: an introduction*, Courier Corporation (2004).
- [121] E. Torrontegui, S. Ibáñez, S. Martínez-Garaot, M. Modugno, A. del Campo, D. Guéry-Odelin, A. Ruschhaupt, X. Chen, and J. G. Muga. *Shortcuts to adiabaticity*. In *Advances in atomic, molecular, and optical physics*, volume 62, page 117. Elsevier, (2013).
- [122] T. Wang, Z. Zhang, L. Xiang, Z. Jia, P. Duan, W. Cai, Z. Gong, Z. Zong, M. Wu, J. Wu, L. Sun, Y. Yin, and G. Guo, *The experimental realization of high-fidelity ‘shortcut-to-adiabaticity’ quantum gates in a superconducting Xmon qubit*, New J. Phys. **20**, 065003 (2018).

-
- [123] P. Kaufmann, T. F. Gloger, D. Kaufmann, M. Johanning, and C. Wunderlich, *High-Fidelity Preservation of Quantum Information During Trapped-Ion Transport*, Phys. Rev. Lett. **120**, 010501 (2018).
- [124] A. Couvert, T. Kawalec, G. Reinaudi, and D. Guéry-Odelin, *Optimal transport of ultracold atoms in the non-adiabatic regime*, EPL **83**, 13001 (2008).
- [125] G. Ness, C. Shkedrov, Y. Florshaim, and Y. Sagi, *Realistic shortcuts to adiabaticity in optical transfer*, New J. Phys. **20**, 095002 (2018).
- [126] J.-F. Schaff, X.-L. Song, P. Capuzzi, P. Vignolo, and G. Labeyrie, *Shortcut to adiabaticity for an interacting Bose-Einstein condensate*, EPL **93**, 23001 (2011).
- [127] W. Rohringer, D. Fischer, F. Steiner, I. E. Mazets, J. Schmiedmayer, and M. Trupke, *Non-equilibrium scale invariance and shortcuts to adiabaticity in a one-dimensional Bose gas*, Sci. Rep. **5**, 9820 (2015).
- [128] H. R. Lewis Jr and W. Riesenfeld, *An exact quantum theory of the time-dependent harmonic oscillator and of a charged particle in a time-dependent electromagnetic field*, J. Math. Phys. **10**, 1458 (1969).
- [129] S. Deffner, C. Jarzynski, and A. del Campo, *Classical and quantum shortcuts to adiabaticity for scale-invariant driving*, Phys. Rev. X **4**, 021013 (2014).
- [130] L. Mandelstam and I. Tamm. *The uncertainty relation between energy and time in non-relativistic quantum mechanics*. In *Selected Papers*, page 115. Springer, (1991).
- [131] N. Margolus and L. B. Levitin, *The maximum speed of dynamical evolution*, Physica D **120**, 188 (1998).
- [132] J. Li, T. Fogarty, S. Campbell, X. Chen, and Th. Busch, *An efficient nonlinear Feshbach engine*, New J. Phys. **20**, 015005 (2018).
- [133] S. Deffner and S. Campbell, *Quantum speed limits: from Heisenberg's uncertainty principle to optimal quantum control*, J. Phys. A Math. Theor. **50**, 453001 (2017).
- [134] S. Campbell and S. Deffner, *Trade-off between speed and cost in shortcuts to adiabaticity*, Phys. Rev. Lett. **118**, 100601 (2017).
- [135] A. del Campo, *Shortcuts to adiabaticity by counterdiabatic driving*, Phys. Rev. Lett. **111**, 100502 (2013).
- [136] P. Francesco, P. Mathieu, and D. Sénéchal, *Conformal field theory*, Springer Science & Business Media (2012).
- [137] D. Sels and A. Polkovnikov, *Minimizing irreversible losses in quantum systems by local counterdiabatic driving*, PNAS **114**, E3909–E3916 (2017).

- [138] K. Perlin. *Improving Noise*. In *Proceedings of the 29th Annual Conference on Computer Graphics and Interactive Techniques*, SIGGRAPH '02, pages 681–682, New York, NY, USA, (2002). Association for Computing Machinery.
- [139] Y. Castin and R. Dum, *Bose-Einstein condensates in time dependent traps*, Phys. Rev. Lett. **77**, 5315 (1996).
- [140] Y. Kagan, E. Surkov, and G. Shlyapnikov, *Evolution of a Bose-condensed gas under variations of the confining potential*, Phys. Rev. A **54**, R1753 (1996).
- [141] L. Carr and J. Brand. *Multidimensional Solitons: Theory*. In *Emergent Nonlinear Phenomena in Bose-Einstein Condensates*, page 133. Springer, (2008).
- [142] H. Saito and M. Ueda, *Dynamically stabilized bright solitons in a two-dimensional Bose-Einstein condensate*, Phys. Rev. Lett. **90**, 040403 (2003).
- [143] M. Desaix, D. Anderson, and M. Lisak, *Variational approach to collapse of optical pulses*, JOSA B **8**, 2082 (1991).
- [144] J. Li, K. Sun, and X. Chen, *Shortcut to adiabatic control of soliton matter waves by tunable interaction*, Sci. Rep. **6**, 38258 (2016).
- [145] V. M. Perez-Garcia, H. Michinel, J. Cirac, M. Lewenstein, and P. Zoller, *Low energy excitations of a Bose-Einstein condensate: A time-dependent variational analysis*, Phys. Rev. Lett. **77**, 5320 (1996).
- [146] E. Pinney, *The nonlinear differential equation $y'' + p(x)y + cy^{-3} = 0$* , Proc. Am. Math. Soc. **1**, 681 (1950).
- [147] J. Muga, X. Chen, A. Ruschhaupt, and D. Guéry-Odelin, *Frictionless dynamics of Bose-Einstein condensates under fast trap variations*, J. Phys. B **42**, 241001 (2009).
- [148] D. Stefanatos and J.-S. Li, *Frictionless decompression in minimum time of Bose-Einstein condensates in the Thomas-Fermi regime*, Phys. Rev. A **86**, 063602 (2012).
- [149] Z. Ozcakmakli and C. Yuce, *Shortcuts to adiabaticity for growing condensates*, Phys. Scr. **86**, 055001 (2012).
- [150] N. L. S. Carnot, *Réflexions sur la puissance motrice du feu et sur les machines propres à développer cette puissance.*, Bachelier (Paris) (1824).
- [151] H. Scovil and E. Schulz-DuBois, *Three-level masers as heat engines*, Phys. Rev. Lett. **2**, 262 (1959).
- [152] D. V. Schroeder, *An introduction to thermal physics*, Pearson (1999).
- [153] B. Gardas and S. Deffner, *Thermodynamic universality of quantum Carnot engines*, Phys. Rev. E **92**, 042126 (2015).

-
- [154] M. O. Scully, M. S. Zubairy, G. S. Agarwal, and H. Walther, *Extracting work from a single heat bath via vanishing quantum coherence*, Science **299**, 862 (2003).
- [155] R. Dillenschneider and E. Lutz, *Energetics of quantum correlations*, EPL **88**, 50003 (2009).
- [156] C. Elouard, D. Herrera-Martí, B. Huard, and A. Auffèves, *Extracting work from quantum measurement in Maxwell's demon engines*, Phys. Rev. Lett. **118**, 260603 (2017).
- [157] X. L. Huang, T. Wang, and X. X. Yi, *Effects of reservoir squeezing on quantum systems and work extraction*, Phys. Rev. E **86**, 051105 (2012).
- [158] O. Abah and E. Lutz, *Efficiency of heat engines coupled to nonequilibrium reservoirs*, EPL **106**, 20001 (2014).
- [159] J. Roßnagel, O. Abah, F. Schmidt-Kaler, K. Singer, and E. Lutz, *Nanoscale heat engine beyond the Carnot limit*, Phys. Rev. Lett. **112**, 030602 (2014).
- [160] W. Niedenzu, D. Gelbwaser-Klimovsky, A. G. Kofman, and G. Kurizki, *On the operation of machines powered by quantum non-thermal baths*, New J. Phys. **18**, 083012 (2016).
- [161] W. Niedenzu, V. Mukherjee, A. Ghosh, A. G. Kofman, and G. Kurizki, *Quantum engine efficiency bound beyond the second law of thermodynamics*, Nat. Commun. **9**, 165 (2018).
- [162] M. Fox, *Quantum optics: an introduction*, Oxford University Press (2006).
- [163] J. Klaers, S. Faelt, A. Imamoglu, and E. Togan, *Squeezed thermal reservoirs as a resource for a nanomechanical engine beyond the carnot limit*, Phys. Rev. X **7**, 031044 (2017).
- [164] J. Klatzow, J. N. Becker, P. M. Ledingham, C. Weinzetl, K. T. Kaczmarek, D. J. Saunders, J. Nunn, I. A. Walmsley, R. Uzdin, and E. Poem, *Experimental demonstration of quantum effects in the operation of microscopic heat engines*, Phys. Rev. Lett. **122**, 110601 (2019).
- [165] S. W. Kim, T. Sagawa, S. De Liberato, and M. Ueda, *Quantum Szilard Engine*, Phys. Rev. Lett. **106**, 070401 (2011).
- [166] J. Jaramillo, M. Beau, and A. del Campo, *Quantum supremacy of many-particle thermal machines*, New J. Phys. **18**, 075019 (2016).
- [167] M. Beau, J. Jaramillo, and A. del Campo, *Scaling-up quantum heat engines efficiently via shortcuts to adiabaticity*, Entropy **18**, 168 (2016).
- [168] G. Watanabe, B. P. Venkatesh, P. Talkner, and A. del Campo, *Quantum performance of thermal machines over many cycles*, Phys. Rev. Lett. **118**, 050601 (2017).

- [169] C. Sulem and P.-L. Sulem, *The nonlinear Schrödinger equation: self-focusing and wave collapse*, Springer Science & Business Media (2007).
- [170] K. E. Strecker, G. B. Partridge, A. G. Truscott, and R. G. Hulet, *Formation and propagation of matter-wave soliton trains*, *Nature* **417**, 150 (2002).
- [171] S. L. Cornish, S. T. Thompson, and C. E. Wieman, *Formation of bright matter-wave solitons during the collapse of attractive Bose-Einstein condensates*, *Phys. Rev. Lett.* **96**, 170401 (2006).
- [172] P. Everitt, M. Sooriyabandara, M. Guasoni, P. Wigley, C. Wei, G. McDonald, K. Hardman, P. Manju, J. Close, C. Kuhn, et al., *Observation of a modulational instability in Bose-Einstein condensates*, *Phys. Rev. A* **96**, 041601 (2017).
- [173] L. Salasnich, A. Parola, and L. Reatto, *Modulational instability and complex dynamics of confined matter-wave solitons*, *Phys. Rev. Lett.* **91**, 080405 (2003).
- [174] L. Carr and J. Brand, *Spontaneous soliton formation and modulational instability in Bose-Einstein condensates*, *Phys. Rev. Lett.* **92**, 040401 (2004).
- [175] L. Carr and J. Brand, *Pulsed atomic soliton laser*, *Phys. Rev. A* **70**, 033607 (2004).
- [176] W. Greiner, L. Neise, and H. Stöcker, *Thermodynamics and statistical mechanics*, Springer Science & Business Media (2012).
- [177] J. Von Neumann, *Thermodynamik Quantenmechanischer Gesamtheiten*, *Nachrichten von der Gesellschaft der Wissenschaften zu Göttingen, Mathematisch-Physikalische Klasse* **1927**, 273 (1927).
- [178] F. Curzon and B. Ahlborn, *Efficiency of a Carnot engine at maximum power output*, *Am. J. Phys.* **43**, 22 (1975).
- [179] C. Van den Broeck, *Thermodynamic efficiency at maximum power*, *Phys. Rev. Lett.* **95**, 190602 (2005).
- [180] S. L. Cornish, N. R. Claussen, J. L. Roberts, E. A. Cornell, and C. E. Wieman, *Stable ^{85}Rb Bose-Einstein condensates with widely tunable interactions*, *Phys. Rev. Lett.* **85**, 1795 (2000).
- [181] S. E. Pollack, D. Dries, M. Junker, Y. Chen, T. Corcovilos, and R. Hulet, *Extreme tunability of interactions in a ^7Li Bose-Einstein Condensate*, *Phys. Rev. Lett.* **102**, 090402 (2009).
- [182] A. Cao, R. Sajjad, H. Mas, E. Q. Simmons, J. L. Tanlimco, E. Nolasco-Martinez, T. Shimasaki, H. Esat Kondakci, V. Galitski, and D. M. Weld, *Interaction-driven breakdown of dynamical localization in a kicked quantum gas*, *arXiv e-prints*, arXiv:2106.09698 (2021).
- [183] N. P. Proukakis and B. Jackson, *Finite-temperature models of Bose-Einstein condensation*, *J. Phys. B* **41**, 203002 (2008).

-
- [184] N. P. Proukakis, S. A. Gardiner, M. Davis, and M. Szymanska, *Quantum gases: finite temperature and non-equilibrium dynamics*, World Scientific (2013).
- [185] E. Zaremba, T. Nikuni, and A. Griffin, *Dynamics of Trapped Bose Gases at Finite Temperatures*, J. Low Temp. Phys. **116**, 277–345 (1999).
- [186] A. Griffin, T. Nikuni, and E. Zaremba, *Bose-condensed gases at finite temperatures*, Cambridge University Press (2009).
- [187] Z. Mehdi, J. J. Hope, S. S. Szigeti, and A. S. Bradley, *Mutual friction and diffusion of two-dimensional quantum vortices*, arXiv e-prints , arXiv:2205.04065 (2022).
- [188] C. W. Gardiner, J. R. Anglin, and T. I. A. Fudge, *The stochastic Gross-Pitaevskii equation*, J. Phys. B **35**, 1555–1582 (2002).
- [189] C. Gardiner and M. Davis, *The stochastic Gross-Pitaevskii equation: II*, J. Phys. B **36**, 4731 (2003).
- [190] P. B. Blakie, A. Bradley, M. Davis, R. Ballagh, and C. Gardiner, *Dynamics and statistical mechanics of ultra-cold Bose gases using c-field techniques*, Adv. Phys. **57**, 363–455 (2008).
- [191] S. J. Rooney. *Implementation and applications of the stochastic projected Gross-Pitaevskii equation*. PhD thesis, University of Otago, (2015).
- [192] S. Stellmer, B. Pasquiou, R. Grimm, and F. Schreck, *Laser Cooling to Quantum Degeneracy*, Phys. Rev. Lett. **110**, 263003 (2013).
- [193] C.-C. Chen, R. González Escudero, J. Minář, B. Pasquiou, S. Bennetts, and F. Schreck, *Continuous Bose-Einstein condensation*, Nature **606**, 683–687 (2022).
- [194] A. Levy, L. Diósi, and R. Kosloff, *Quantum flywheel*, Phys. Rev. A **93**, 052119 (2016).
- [195] D. von Lindenfels, O. Gräß, C. T. Schmiegelow, V. Kaushal, J. Schulz, M. T. Mitchison, J. Goold, F. Schmidt-Kaler, and U. G. Poschinger, *Spin Heat Engine Coupled to a Harmonic-Oscillator Flywheel*, Phys. Rev. Lett. **123**, 080602 (2019).
- [196] D. Hunger, S. Camerer, T. W. Hänsch, D. König, J. P. Kotthaus, J. Reichel, and P. Treutlein, *Resonant coupling of a Bose-Einstein condensate to a micromechanical oscillator*, Phys. Rev. Lett. **104**, 143002 (2010).
- [197] J. M. Obrecht, R. Wild, M. Antezza, L. Pitaevskii, S. Stringari, and E. A. Cornell, *Measurement of the temperature dependence of the Casimir-Polder force*, Phys. Rev. Lett. **98**, 063201 (2007).
- [198] N. L. Gullo, Th. Busch, G. Palma, and M. Paternostro, *Probing mechanical quantum coherence with an ultracold-atom meter*, Phys. Rev. A **84**, 063815 (2011).

- [199] C. Maschler, I. B. Mekhov, and H. Ritsch, *Ultracold atoms in optical lattices generated by quantized light fields*, Eur. Phys. J. D **46**, 545 (2008).
- [200] H. Ritsch, P. Domokos, F. Brennecke, and T. Esslinger, *Cold atoms in cavity-generated dynamical optical potentials*, Rev. Mod. Phys. **85**, 553 (2013).
- [201] M. Aspelmeyer, T. J. Kippenberg, and F. Marquardt, *Cavity optomechanics*, Rev. Mod. Phys. **86**, 1391 (2014).
- [202] H.-O. Georgii, *Stochastics: Introduction to Probability and Statistics*, De Gruyter (2012).
- [203] V. Giovannetti, S. Lloyd, and L. Maccone, *Quantum-Enhanced Measurements: Beating the Standard Quantum Limit*, Science **306**, 1330–1336 (2004).
- [204] V. Giovannetti, S. Lloyd, and L. Maccone, *Quantum Metrology*, Phys. Rev. Lett. **96**, 010401 (2006).
- [205] V. Giovannetti, S. Lloyd, and L. Maccone, *Advances in quantum metrology*, Nat. Photonics **5**, 222–229 (2011).
- [206] S. L. Braunstein and C. M. Caves, *Statistical distance and the geometry of quantum states*, Phys. Rev. Lett. **72**, 3439–3443 (1994).
- [207] P. Zanardi, P. Giorda, and M. Cozzini, *Information-Theoretic Differential Geometry of Quantum Phase Transitions*, Phys. Rev. Lett. **99**, 100603 (2007).
- [208] P. Zanardi, M. G. A. Paris, and L. Campos Venuti, *Quantum criticality as a resource for quantum estimation*, Phys. Rev. A **78**, 042105 (2008).
- [209] T. W. B. Kibble, *Topology of cosmic domains and strings*, J. Phys. A: Math. Gen. **9**, 1387–1398 (1976).
- [210] W. H. Zurek, *Cosmological experiments in superfluid helium?*, Nature **317**, 505–508 (1985).
- [211] W. H. Zurek, U. Dorner, and P. Zoller, *Dynamics of a Quantum Phase Transition*, Phys. Rev. Lett. **95**, 105701 (2005).
- [212] M. M. Rams, P. Sierant, O. Dutta, P. Horodecki, and J. Zakrzewski, *At the Limits of Criticality-Based Quantum Metrology: Apparent Super-Heisenberg Scaling Revisited*, Phys. Rev. X **8**, 021022 (2018).
- [213] O. Abah, R. Puebla, A. Kiely, G. D. Chiara, M. Paternostro, and S. Campbell, *Energetic cost of quantum control protocols*, New J. Phys. **21**, 103048 (2019).
- [214] Y.-H. Chen, W. Qin, X. Wang, A. Miranowicz, and F. Nori, *Shortcuts to Adiabaticity for the Quantum Rabi Model: Efficient Generation of Giant Entangled Cat States via Parametric Amplification*, Phys. Rev. Lett. **126**, 023602 (2021).

-
- [215] L. D. Landau, *Zur Theorie der Energieübertragung II*, Z. Sowjetunion **2**, 46–51 (1932).
- [216] C. Zener, *Non-adiabatic crossing of energy levels*, Proc. R. Soc. Lond. A **137**, 696–702 (1932).
- [217] Q. Xie, H. Zhong, M. T. Batchelor, and C. Lee, *The quantum Rabi model: solution and dynamics*, J. Phys. A Math. Theor. **50**, 113001 (2017).
- [218] S. Bravyi, D. P. DiVincenzo, and D. Loss, *Schrieffer–Wolff transformation for quantum many-body systems*, Ann. Phys. (N. Y.) **326**, 2793–2826 (2011).
- [219] M.-J. Hwang, R. Puebla, and M. B. Plenio, *Quantum Phase Transition and Universal Dynamics in the Rabi Model*, Phys. Rev. Lett. **115**, 180404 (2015).
- [220] R. Loudon, *The Quantum Theory of Light*, Oxford University Press (2000).
- [221] L. Garbe, M. Bina, A. Keller, M. G. Paris, and S. Felicetti, *Critical Quantum metrology with a finite-component quantum phase transition*, Phys. Rev. Lett. **124**, 120504 (2020).
- [222] T. Ilias, D. Yang, S. F. Huelga, and M. B. Plenio, *Criticality-Enhanced Quantum Sensing via Continuous Measurement*, PRX Quantum **3**, 010354 (2022).
- [223] L. Garbe, O. C. Abah, S. Felicetti, and R. Puebla, *Critical quantum metrology with fully-connected models: from Heisenberg to Kibble-Zurek scaling*, Quantum Sci. Technol. (2022).
- [224] F. Minganti, L. Garbe, A. Le Boité, and S. Felicetti, *Non-Gaussian superradiant transition via three-body ultrastrong coupling*, arXiv e-prints , arXiv:2204.03520 (2022).
- [225] T. Hatomura, A. Yoshinaga, Y. Matsuzaki, and M. Tatsuta, *Quantum metrology based on symmetry-protected adiabatic transformation: imperfection, finite time duration, and dephasing*, New J. Phys. **24**, 033005 (2022).
- [226] E. Aybar, A. Niezgodá, S. S. Mirkhalaf, M. W. Mitchell, D. Benedicto Orenes, and E. Witkowska, *Critical quantum thermometry and its feasibility in spin systems*, arXiv e-prints , arXiv:2204.02734 (2022).
- [227] K. Gietka, *Squeezing by critical speeding up: Applications in quantum metrology*, Phys. Rev. A **105**, 042620 (2022).
- [228] K. Gietka, L. Ruks, and Th. Busch, *Understanding and Improving Critical Metrology. Quenching Superradiant Light-Matter Systems Beyond the Critical Point*, Quantum **6**, 700 (2022).
- [229] H. Büchler, G. Blatter, and W. Zwerger, *Commensurate-incommensurate transition of cold atoms in an optical lattice*, Phys. Rev. Lett. **90**, 130401 (2003).

- [230] E. Haller, R. Hart, M. J. Mark, J. G. Danzl, L. Reichsöllner, M. Gustavsson, M. Dalmonte, G. Pupillo, and H.-C. Nägerl, *Pinning quantum phase transition for a Luttinger liquid of strongly interacting bosons*, *Nature* **466**, 597–600 (2010).
- [231] M. A. Cazalilla, *Bosonizing one-dimensional cold atomic gases*, *J. Phys. B* **37**, S1–S47 (2004).
- [232] S. Coleman, *Quantum sine-Gordon equation as the massive Thirring model*, *Phys. Rev. D* **11**, 2088–2097 (1975).
- [233] A. O. Gogolin, A. A. Nersisyan, and A. M. Tsvelik, *Bosonization and strongly correlated systems*, Cambridge University Press (2004).
- [234] D. Jaksch, C. Bruder, J. I. Cirac, C. W. Gardiner, and P. Zoller, *Cold Bosonic Atoms in Optical Lattices*, *Phys. Rev. Lett.* **81**, 3108–3111 (1998).
- [235] T. D. Kühner, S. R. White, and H. Monien, *One-dimensional Bose-Hubbard model with nearest-neighbor interaction*, *Phys. Rev. B* **61**, 12474–12489 (2000).
- [236] O. V. Lounasmaa, *Experimental principles and methods below 1K*, Academic Press Inc., Ltd., London (1974).
- [237] H. Zu, W. Dai, and A. de Waele, *Development of dilution refrigerators—A review*, *Cryogenics* **121**, 103390 (2022).
- [238] T.-L. Ho, *Spinor Bose Condensates in Optical Traps*, *Phys. Rev. Lett.* **81**, 742–745 (1998).
- [239] C. J. Myatt, E. A. Burt, R. W. Ghrist, E. A. Cornell, and C. E. Wieman, *Production of Two Overlapping Bose-Einstein Condensates by Sympathetic Cooling*, *Phys. Rev. Lett.* **78**, 586–589 (1997).
- [240] T.-L. Ho and V. B. Shenoy, *Binary Mixtures of Bose Condensates of Alkali Atoms*, *Phys. Rev. Lett.* **77**, 3276–3279 (1996).
- [241] Th. Busch, J. I. Cirac, V. M. Pérez-García, and P. Zoller, *Stability and collective excitations of a two-component Bose-Einstein condensed gas: A moment approach*, *Phys. Rev. A* **56**, 2978–2983 (1997).
- [242] D. S. Hall, M. R. Matthews, J. R. Ensher, C. E. Wieman, and E. A. Cornell, *Dynamics of Component Separation in a Binary Mixture of Bose-Einstein Condensates*, *Phys. Rev. Lett.* **81**, 1539–1542 (1998).
- [243] G. Thalhammer, G. Barontini, L. De Sarlo, J. Catani, F. Minardi, and M. Inguscio, *Double Species Bose-Einstein Condensate with Tunable Interspecies Interactions*, *Phys. Rev. Lett.* **100**, 210402 (2008).
- [244] S. B. Papp, J. M. Pino, and C. E. Wieman, *Tunable Miscibility in a Dual-Species Bose-Einstein Condensate*, *Phys. Rev. Lett.* **101**, 040402 (2008).

-
- [245] D. J. McCarron, H. W. Cho, D. L. Jenkin, M. P. Köppinger, and S. L. Cornish, *Dual-species Bose-Einstein condensate of ^{87}Rb and ^{133}Cs* , Phys. Rev. A **84**, 011603 (2011).
- [246] L. Wacker, N. B. Jørgensen, D. Birkmose, R. Horchani, W. Ertmer, C. Klempt, N. Winter, J. Sherson, and J. J. Arlt, *Tunable dual-species Bose-Einstein condensates of ^{39}K and ^{87}Rb* , Phys. Rev. A **92**, 053602 (2015).
- [247] F. Wang, X. Li, D. Xiong, and D. Wang, *A double species ^{23}Na and ^{87}Rb Bose-Einstein condensate with tunable miscibility via an interspecies Feshbach resonance*, J. Phys. B **49**, 015302 (2015).
- [248] T. A. Schulze, T. Hartmann, K. K. Voges, M. W. Gempel, E. Tiemann, A. Zen-esini, and S. Ospelkaus, *Feshbach spectroscopy and dual-species Bose-Einstein condensation of ^{23}Na – ^{39}K mixtures*, Phys. Rev. A **97**, 023623 (2018).
- [249] A. Burchianti, C. D’Errico, S. Rosi, A. Simoni, M. Modugno, C. Fort, and F. Minardi, *Dual-species Bose-Einstein condensate of ^{41}K and ^{87}Rb in a hybrid trap*, Phys. Rev. A **98**, 063616 (2018).
- [250] A. Burchianti, C. D’Errico, M. Prevedelli, L. Salasnich, F. Ancilotto, M. Modugno, F. Minardi, and C. Fort, *A dual-species Bose-Einstein condensate with attractive interspecies interactions*, Condens. Matter **5**, 21 (2020).
- [251] D. M. Stamper-Kurn, M. R. Andrews, A. P. Chikkatur, S. Inouye, H.-J. Miesner, J. Stenger, and W. Ketterle, *Optical Confinement of a Bose-Einstein Condensate*, Phys. Rev. Lett. **80**, 2027–2030 (1998).
- [252] H.-J. Miesner, D. M. Stamper-Kurn, J. Stenger, S. Inouye, A. P. Chikkatur, and W. Ketterle, *Observation of Metastable States in Spinor Bose-Einstein Condensates*, Phys. Rev. Lett. **82**, 2228–2231 (1999).
- [253] H. Pu, C. K. Law, S. Raghavan, J. H. Eberly, and N. P. Bigelow, *Spin-mixing dynamics of a spinor Bose-Einstein condensate*, Phys. Rev. A **60**, 1463–1470 (1999).
- [254] A. Görlitz, T. L. Gustavson, A. E. Leanhardt, R. Löw, A. P. Chikkatur, S. Gupta, S. Inouye, D. E. Pritchard, and W. Ketterle, *Sodium Bose-Einstein Condensates in the $F = 2$ State in a Large-Volume Optical Trap*, Phys. Rev. Lett. **90**, 090401 (2003).
- [255] H. Schmaljohann, M. Erhard, J. Kronjäger, M. Kottke, S. van Staa, L. Cacciapuoti, J. J. Arlt, K. Bongs, and K. Sengstock, *Dynamics of $F = 2$ Spinor Bose-Einstein Condensates*, Phys. Rev. Lett. **92**, 040402 (2004).
- [256] A. T. Black, E. Gomez, L. D. Turner, S. Jung, and P. D. Lett, *Spinor Dynamics in an Antiferromagnetic Spin-1 Condensate*, Phys. Rev. Lett. **99**, 070403 (2007).

- [257] B. Pasquiou, E. Maréchal, G. Bismut, P. Pedri, L. Vernac, O. Gorceix, and B. Laburthe-Tolra, *Spontaneous Demagnetization of a Dipolar Spinor Bose Gas in an Ultralow Magnetic Field*, Phys. Rev. Lett. **106**, 255303 (2011).
- [258] Y. Kawaguchi and M. Ueda, *Spinor Bose–Einstein condensates*, Phys. Rep. **520**, 253–381 (2012).
- [259] A. G. Truscott, K. E. Strecker, W. I. McAlexander, G. B. Partridge, and R. G. Hulet, *Observation of Fermi Pressure in a Gas of Trapped Atoms*, Science **291**, 2570–2572 (2001).
- [260] I. Ferrier-Barbut, M. Delehaye, S. Laurent, A. T. Grier, M. Pierce, B. S. Rem, F. Chevy, and C. Salomon, *A mixture of Bose and Fermi superfluids*, Science **345**, 1035–1038 (2014).
- [261] K. Mølmer, *Bose Condensates and Fermi Gases at Zero Temperature*, Phys. Rev. Lett. **80**, 1804–1807 (1998).
- [262] P. Anders, P. Werner, M. Troyer, M. Sigrist, and L. Pollet, *From the Cooper Problem to Canted Supersolids in Bose-Fermi Mixtures*, Phys. Rev. Lett. **109**, 206401 (2012).
- [263] C. Ufrecht, M. Meister, A. Roura, and W. P. Schleich, *Comprehensive classification for Bose–Fermi mixtures*, New J. Phys. **19**, 085001 (2017).
- [264] S. Röthel and A. Pelster, *Density and stability in ultracold dilute boson-fermion mixtures*, Eur. Phys. J. B **59**, 343–356 (2007).
- [265] G. Roati, F. Riboli, G. Modugno, and M. Inguscio, *Fermi-Bose Quantum Degenerate ^{40}K – ^{87}Rb Mixture with Attractive Interaction*, Phys. Rev. Lett. **89**, 150403 (2002).
- [266] J. Goldwin, S. Inouye, M. L. Olsen, B. Newman, B. D. DePaola, and D. S. Jin, *Measurement of the interaction strength in a Bose-Fermi mixture with ^{87}Rb and ^{40}K* , Phys. Rev. A **70**, 021601 (2004).
- [267] G. Modugno, G. Roati, F. Riboli, F. Ferlaino, R. J. Brecha, and M. Inguscio, *Collapse of a Degenerate Fermi Gas*, Science **297**, 2240–2243 (2002).
- [268] C. Ospelkaus, S. Ospelkaus, K. Sengstock, and K. Bongs, *Interaction-Driven Dynamics of ^{40}K – ^{87}Rb Fermion-Boson Gas Mixtures in the Large-Particle-Number Limit*, Phys. Rev. Lett. **96**, 020401 (2006).
- [269] K. Günter, T. Stöferle, H. Moritz, M. Köhl, and T. Esslinger, *Bose-Fermi Mixtures in a Three-Dimensional Optical Lattice*, Phys. Rev. Lett. **96**, 180402 (2006).
- [270] Z. Hadzibabic, C. A. Stan, K. Dieckmann, S. Gupta, M. W. Zwierlein, A. Görlitz, and W. Ketterle, *Two-Species Mixture of Quantum Degenerate Bose and Fermi Gases*, Phys. Rev. Lett. **88**, 160401 (2002).

-
- [271] B. J. DeSalvo, K. Patel, J. Johansen, and C. Chin, *Observation of a Degenerate Fermi Gas Trapped by a Bose-Einstein Condensate*, Phys. Rev. Lett. **119**, 233401 (2017).
- [272] C.-H. Wu, I. Santiago, J. W. Park, P. Ahmadi, and M. W. Zwierlein, *Strongly interacting isotopic Bose-Fermi mixture immersed in a Fermi sea*, Phys. Rev. A **84**, 011601 (2011).
- [273] M. K. Tey, S. Stellmer, R. Grimm, and F. Schreck, *Double-degenerate Bose-Fermi mixture of strontium*, Phys. Rev. A **82**, 011608 (2010).
- [274] T. Fukuhara, S. Sugawa, Y. Takasu, and Y. Takahashi, *All-optical formation of quantum degenerate mixtures*, Phys. Rev. A **79**, 021601 (2009).
- [275] V. D. Vaidya, J. Tiamsuphat, S. L. Rolston, and J. V. Porto, *Degenerate Bose-Fermi mixtures of rubidium and ytterbium*, Phys. Rev. A **92**, 043604 (2015).
- [276] M. Taglieber, A.-C. Voigt, T. Aoki, T. W. Hänsch, and K. Dieckmann, *Quantum Degenerate Two-Species Fermi-Fermi Mixture Coexisting with a Bose-Einstein Condensate*, Phys. Rev. Lett. **100**, 010401 (2008).
- [277] E. Wille, F. M. Spiegelhalter, G. Kerner, D. Naik, A. Trenkwalder, G. Hendl, F. Schreck, R. Grimm, T. G. Tiecke, J. T. M. Walraven, S. J. J. M. F. Kokkelmans, E. Tiesinga, and P. S. Julienne, *Exploring an Ultracold Fermi-Fermi Mixture: Interspecies Feshbach Resonances and Scattering Properties of ^6Li and ^{40}K* , Phys. Rev. Lett. **100**, 053201 (2008).
- [278] S. Giorgini, L. P. Pitaevskii, and S. Stringari, *Theory of ultracold atomic Fermi gases*, Rev. Mod. Phys. **80**, 1215–1274 (2008).
- [279] Y.-i. Shin, A. Schirotzek, C. H. Schunck, and W. Ketterle, *Realization of a Strongly Interacting Bose-Fermi Mixture from a Two-Component Fermi Gas*, Phys. Rev. Lett. **101**, 070404 (2008).
- [280] X. Cui and T.-L. Ho, *Phase Separation in Mixtures of Repulsive Fermi Gases Driven by Mass Difference*, Phys. Rev. Lett. **110**, 165302 (2013).
- [281] C. Cabrera, L. Tanzi, J. Sanz, B. Naylor, P. Thomas, P. Cheiney, and L. Tarruell, *Quantum liquid droplets in a mixture of Bose-Einstein condensates*, Science **359**, 301 (2018).
- [282] D. Petrov, *Quantum mechanical stabilization of a collapsing Bose-Bose mixture*, Phys. Rev. Lett. **115**, 155302 (2015).
- [283] A. White, T. Hennessy, and Th. Busch, *Emergence of classical rotation in superfluid Bose-Einstein condensates*, Phys. Rev. A **93**, 033601 (2016).
- [284] T. Sowiński and M. Á. García-March, *One-dimensional mixtures of several ultracold atoms: a review*, Rep. Prog. Phys. **82**, 104401 (2019).

-
- [285] K. Baumann, C. Guerlin, F. Brennecke, and T. Esslinger, *Dicke quantum phase transition with a superfluid gas in an optical cavity*, Nature **464**, 1301–1306 (2010).
- [286] S. Fernández-Vidal, G. De Chiara, J. Larson, and G. Morigi, *Quantum ground state of self-organized atomic crystals in optical resonators*, Phys. Rev. A **81**, 043407 (2010).
- [287] H. Habibian, A. Winter, S. Paganelli, H. Rieger, and G. Morigi, *Bose-glass phases of ultracold atoms due to cavity backaction*, Phys. Rev. Lett. **110**, 075304 (2013).
- [288] S. Schütz, S. B. Jäger, and G. Morigi, *Thermodynamics and dynamics of atomic self-organization in an optical cavity*, Phys. Rev. A **92**, 063808 (2015).
- [289] R. Mottl, F. Brennecke, K. Baumann, R. Landig, T. Donner, and T. Esslinger, *Roton-Type Mode Softening in a Quantum Gas with Cavity-Mediated Long-Range Interactions*, Science **336**, 1570–1573 (2012).
- [290] G. M. Bruun, *New interactions seen in an ultracold gas*, Nature **568**, 37–38 (2019).
- [291] B. J. DeSalvo, K. Patel, G. Cai, and C. Chin, *Observation of fermion-mediated interactions between bosonic atoms*, Nature **568**, 61–64 (2019).
- [292] J. J. Kinnunen and G. M. Bruun, *Induced interactions in a superfluid Bose-Fermi mixture*, Phys. Rev. A **91**, 041605 (2015).
- [293] H. P. Büchler and G. Blatter, *Supersolid versus Phase Separation in Atomic Bose-Fermi Mixtures*, Phys. Rev. Lett. **91**, 130404 (2003).
- [294] P. P. Orth, D. L. Bergman, and K. Le Hur, *Supersolidity of cold-atom Bose-Fermi mixtures in optical lattices*, Phys. Rev. A **80**, 023624 (2009).
- [295] I. Titvinidze, M. Snoek, and W. Hofstetter, *Supersolid Bose-Fermi Mixtures in Optical Lattices*, Phys. Rev. Lett. **100**, 100401 (2008).
- [296] V. Yukalov and M. Girardeau, *Fermi-Bose mapping for one-dimensional Bose gases*, Laser Phys. Lett. **2**, 375 (2005).
- [297] K. K. Das, *Bose-Fermi Mixtures in One Dimension*, Phys. Rev. Lett. **90**, 170403 (2003).
- [298] P. Sengupta and L. P. Pryadko, *Quantum degenerate Bose-Fermi mixtures on one-dimensional optical lattices*, Phys. Rev. B **75**, 132507 (2007).
- [299] A. Albus, F. Illuminati, and J. Eisert, *Mixtures of bosonic and fermionic atoms in optical lattices*, Phys. Rev. A **68**, 023606 (2003).
- [300] L. Pollet, M. Troyer, K. Van Houcke, and S. M. A. Rombouts, *Phase Diagram of Bose-Fermi Mixtures in One-Dimensional Optical Lattices*, Phys. Rev. Lett. **96**, 190402 (2006).

-
- [301] F. Hébert, F. Haudin, L. Pollet, and G. G. Batrouni, *Mott insulators and correlated superfluids in ultracold Bose-Fermi mixtures*, Phys. Rev. A **76**, 043619 (2007).
- [302] L. Pollet, C. Kollath, U. Schollwöck, and M. Troyer, *Mixture of bosonic and spin-polarized fermionic atoms in an optical lattice*, Phys. Rev. A **77**, 023608 (2008).
- [303] A. Zujev, A. Baldwin, R. T. Scalettar, V. G. Rousseau, P. J. H. Denteneer, and M. Rigol, *Superfluid and Mott-insulator phases of one-dimensional Bose-Fermi mixtures*, Phys. Rev. A **78**, 033619 (2008).
- [304] C. K. Lai and C. N. Yang, *Ground-State Energy of a Mixture of Fermions and Bosons in One Dimension with a Repulsive δ -Function Interaction*, Phys. Rev. A **3**, 393–399 (1971).
- [305] A. Imambekov and E. Demler, *Exactly solvable case of a one-dimensional Bose-Fermi mixture*, Phys. Rev. A **73**, 021602 (2006).
- [306] M. T. Batchelor, M. Bortz, X. W. Guan, and N. Oelkers, *Exact results for the one-dimensional mixed boson-fermion interacting gas*, Phys. Rev. A **72**, 061603 (2005).
- [307] B. Fang, P. Vignolo, M. Gattobigio, C. Miniatura, and A. Minguzzi, *Exact solution for the degenerate ground-state manifold of a strongly interacting one-dimensional Bose-Fermi mixture*, Phys. Rev. A **84**, 023626 (2011).
- [308] A. S. Dehkharghani, F. F. Bellotti, and N. T. Zinner, *Analytical and numerical studies of Bose-Fermi mixtures in a one-dimensional harmonic trap*, J. Phys. B **50**, 144002 (2017).
- [309] M. A. Cazalilla and A. F. Ho, *Instabilities in Binary Mixtures of One-Dimensional Quantum Degenerate Gases*, Phys. Rev. Lett. **91**, 150403 (2003).
- [310] L. Viverit and S. Giorgini, *Ground-state properties of a dilute Bose-Fermi mixture*, Phys. Rev. A **66**, 063604 (2002).
- [311] L. Mathey, D.-W. Wang, W. Hofstetter, M. D. Lukin, and E. Demler, *Luttinger Liquid of Polarons in One-Dimensional Boson-Fermion Mixtures*, Phys. Rev. Lett. **93**, 120404 (2004).
- [312] E. Burovski, G. Orso, and T. Jolicoeur, *Multiparticle Composites in Density-Imbalanced Quantum Fluids*, Phys. Rev. Lett. **103**, 215301 (2009).
- [313] M. Rizzi and A. Imambekov, *Pairing of one-dimensional Bose-Fermi mixtures with unequal masses*, Phys. Rev. A **77**, 023621 (2008).
- [314] T. Karpiuk, M. Brewczyk, S. Ospelkaus-Schwarzer, K. Bongs, M. Gajda, and K. Rzażewski, *Soliton Trains in Bose-Fermi Mixtures*, Phys. Rev. Lett. **93**, 100401 (2004).

- [315] T. Karpiuk, M. Brewczyk, and K. Rzażewski, *Bright solitons in Bose-Fermi mixtures*, Phys. Rev. A **73**, 053602 (2006).
- [316] S. K. Adhikari and L. Salasnich, *One-dimensional superfluid Bose-Fermi mixture: Mixing, demixing, and bright solitons*, Phys. Rev. A **76**, 023612 (2007).
- [317] F. Crépin, G. Zaránd, and P. Simon, *Disordered One-Dimensional Bose-Fermi Mixtures: The Bose-Fermi Glass*, Phys. Rev. Lett. **105**, 115301 (2010).
- [318] M. Tylutki, A. Recati, F. Dalfovo, and S. Stringari, *Dark-bright solitons in a superfluid Bose-Fermi mixture*, New J. Phys. **18**, 053014 (2016).
- [319] L. Mathey and D.-W. Wang, *Phase diagrams of one-dimensional Bose-Fermi mixtures of ultracold atoms*, Phys. Rev. A **75**, 013612 (2007).
- [320] L. Mathey, *Commensurate mixtures of ultracold atoms in one dimension*, Phys. Rev. B **75**, 144510 (2007).
- [321] F. Hébert, G. G. Batrouni, X. Roy, and V. G. Rousseau, *Supersolids in one-dimensional Bose-Fermi mixtures*, Phys. Rev. B **78**, 184505 (2008).
- [322] T. Miyakawa, H. Yabu, and T. Suzuki, *Peierls instability, periodic Bose-Einstein condensates, and density waves in quasi-one-dimensional boson-fermion mixtures of atomic gases*, Phys. Rev. A **70**, 013612 (2004).
- [323] M. Bruderer, W. Bao, and D. Jaksch, *Self-trapping of impurities in Bose-Einstein condensates: Strong attractive and repulsive coupling*, Europhys. Lett. **82**, 30004 (2008).
- [324] A. Blinova, M. Boshier, and E. Timmermans, *Two polaron flavors of the bose-einstein condensate impurity*, Phys. Rev. A **88**, 053610 (2013).
- [325] F. Grusdt, G. E. Astrakharchik, and E. Demler, *Bose polarons in ultracold atoms in one dimension: beyond the Fröhlich paradigm*, New J. Phys. **19**, 103035 (2017).
- [326] S. Mistakidis, G. Katsimiga, G. Koutentakis, Th. Busch, and P. Schmelcher, *Quench dynamics and orthogonality catastrophe of Bose polarons*, Phys. Rev. Lett. **122**, 183001 (2019).
- [327] M. Will, G. E. Astrakharchik, and M. Fleischhauer, *Polaron Interactions and Bipolarons in One-Dimensional Bose Gases in the Strong Coupling Regime*, Phys. Rev. Lett. **127**, 103401 (2021).
- [328] R. Schmidt and T. Enss, *Self-stabilized Bose polarons*, arXiv e-prints , arXiv:2102.13616 (2021).
- [329] P. G. Kevrekidis, D. J. Frantzeskakis, and R. Carretero-González, *Emergent Nonlinear Phenomena in Bose-Einstein Condensates: Theory and Experiment*, Springer Science & Business Media, New York (2007).

-
- [330] Y. Atas, D. Gangardt, I. Bouchoule, and K. Kheruntsyan, *Exact nonequilibrium dynamics of finite-temperature Tonks-Girardeau gases*, Phys. Rev. A **95**, 043622 (2017).
- [331] Y. Y. Atas, I. Bouchoule, D. M. Gangardt, and K. V. Kheruntsyan, *Collective many-body bounce in the breathing-mode oscillations of a Tonks-Girardeau gas*, Phys. Rev. A **96**, 041605(R) (2017).
- [332] O. I. Pâțu, *Nonequilibrium dynamics of the anyonic Tonks-Girardeau gas at finite temperature*, Phys. Rev. A **102**, 043303 (2020).
- [333] R. J. Baxter, *Exactly solved models in statistical mechanics*, Elsevier (2016).
- [334] T. Kinoshita, T. Wenger, and D. S. Weiss, *Observation of a one-dimensional Tonks-Girardeau gas*, Science **305**, 1125–1128 (2004).
- [335] P. Naidon, *Magnetic Feshbach resonances in ${}^7\text{Li}-{}^{133}\text{Cs}$ mixtures*, arXiv e-prints, arXiv:2001.05329 (2020).
- [336] K. Viebahn. Private Communication.
- [337] A. L. Gaunt, T. F. Schmidutz, I. Gotlibovych, R. P. Smith, and Z. Hadzibabic, *Bose-Einstein Condensation of Atoms in a Uniform Potential*, Phys. Rev. Lett. **110**, 200406 (2013).
- [338] M. Tajik, B. Rauer, T. Schweigler, F. Cataldini, J. ao Sabino, F. S. Møller, S.-C. Ji, I. E. Mazets, and J. Schmiedmayer, *Designing arbitrary one-dimensional potentials on an atom chip*, Opt. Express **27**, 33474–33487 (2019).
- [339] N. Navon, R. P. Smith, and Z. Hadzibabic, *Quantum gases in optical boxes*, Nature Physics **17**, 1334–1341 (2021).
- [340] G. V. Chester, *Speculations on Bose-Einstein Condensation and Quantum Crystals*, Phys. Rev. A **2**, 256–258 (1970).
- [341] A. J. Leggett, *Can a Solid Be "Superfluid"?*, Phys. Rev. Lett. **25**, 1543–1546 (1970).
- [342] J. Goold, M. Krych, Z. Idziaszek, T. Fogarty, and Th. Busch, *An eccentrically perturbed Tonks-Girardeau gas*, New J. Phys. **12**, 093041 (2010).
- [343] F. Böttcher, J.-N. Schmidt, M. Wenzel, J. Hertkorn, M. Guo, T. Langen, and T. Pfau, *Transient Supersolid Properties in an Array of Dipolar Quantum Droplets*, Phys. Rev. X **9**, 011051 (2019).
- [344] L. Chomaz, D. Petter, P. Ilzhöfer, G. Natale, A. Trautmann, C. Politi, G. Durastante, R. M. W. van Bijnen, A. Patscheider, M. Sohmen, M. J. Mark, and F. Ferlaino, *Long-Lived and Transient Supersolid Behaviors in Dipolar Quantum Gases*, Phys. Rev. X **9**, 021012 (2019).

- [345] S. M. Roccuzzo and F. Ancilotto, *Supersolid behavior of a dipolar Bose-Einstein condensate confined in a tube*, Phys. Rev. A **99**, 041601 (2019).
- [346] J. Hertkorn, F. Böttcher, M. Guo, J. N. Schmidt, T. Langen, H. P. Büchler, and T. Pfau, *Fate of the Amplitude Mode in a Trapped Dipolar Supersolid*, Phys. Rev. Lett. **123**, 193002 (2019).
- [347] F. Böttcher, J.-N. Schmidt, J. Hertkorn, K. S. H. Ng, S. D. Graham, M. Guo, T. Langen, and T. Pfau, *New states of matter with fine-tuned interactions: quantum droplets and dipolar supersolids*, Rep. Prog. Phys. **84**, 012403 (2020).
- [348] P. B. Blakie, D. Baillie, L. Chomaz, and F. Ferlaino, *Supersolidity in an elongated dipolar condensate*, Phys. Rev. Research **2**, 043318 (2020).
- [349] L. Chomaz, R. M. W. van Bijnen, D. Petter, G. Faraoni, S. Baier, J. H. Becher, M. J. Mark, F. Wächtler, L. Santos, and F. Ferlaino, *Observation of roton mode population in a dipolar quantum gas*, Nat. Phys. **14**, 442–446 (2018).
- [350] G. Natale, R. M. W. van Bijnen, A. Patscheider, D. Petter, M. J. Mark, L. Chomaz, and F. Ferlaino, *Excitation Spectrum of a Trapped Dipolar Supersolid and Its Experimental Evidence*, Phys. Rev. Lett. **123**, 050402 (2019).
- [351] M. Guo, F. Böttcher, J. Hertkorn, J.-N. Schmidt, M. Wenzel, H. P. Büchler, T. Langen, and T. Pfau, *The low-energy Goldstone mode in a trapped dipolar supersolid*, Nature **574**, 386–389 (2019).
- [352] J. Hertkorn, J.-N. Schmidt, F. Böttcher, M. Guo, M. Schmidt, K. S. H. Ng, S. D. Graham, H. P. Büchler, T. Langen, M. Zwierlein, and T. Pfau, *Density Fluctuations across the Superfluid-Supersolid Phase Transition in a Dipolar Quantum Gas*, Phys. Rev. X **11**, 011037 (2021).
- [353] E. B. Kolomeisky, T. J. Newman, J. P. Straley, and X. Qi, *Low-Dimensional Bose Liquids: Beyond the Gross-Pitaevskii Approximation*, Phys. Rev. Lett. **85**, 1146–1149 (2000).
- [354] T. D. Lee, K. Huang, and C. N. Yang, *Eigenvalues and Eigenfunctions of a Bose System of Hard Spheres and Its Low-Temperature Properties*, Phys. Rev. **106**, 1135–1145 (1957).
- [355] J. Settino, N. Lo Gullo, F. Plastina, and A. Minguzzi, *Exact Spectral Function of a Tonks-Girardeau Gas in a Lattice*, Phys. Rev. Lett. **126**, 065301 (2021).
- [356] P. B. Blakie, D. Baillie, and R. N. Bisset, *Roton spectroscopy in a harmonically trapped dipolar Bose-Einstein condensate*, Phys. Rev. A **86**, 021604 (2012).
- [357] G.-B. Jo, Y.-R. Lee, J.-H. Choi, C. A. Christensen, T. H. Kim, J. H. Thywissen, D. E. Pritchard, and W. Ketterle, *Itinerant Ferromagnetism in a Fermi Gas of Ultracold Atoms*, Science **325**, 1521–1524 (2009).

-
- [358] A. Friedenauer, H. Schmitz, J. T. Glueckert, D. Porras, and T. Schaetz, *Simulating a quantum magnet with trapped ions*, Nat. Phys. **4**, 757–761 (2008).
- [359] K. Kim, M. S. Chang, S. Korenblit, R. Islam, E. E. Edwards, J. K. Freericks, G. D. Lin, L. M. Duan, and C. Monroe, *Quantum simulation of frustrated Ising spins with trapped ions*, Nature **465**, 590–593 (2010).
- [360] J. Simon, W. S. Bakr, R. Ma, M. E. Tai, P. M. Preiss, and M. Greiner, *Quantum simulation of antiferromagnetic spin chains in an optical lattice*, Nature **472**, 307–312 (2011).
- [361] J. Struck, M. Weinberg, C. Ölschläger, P. Windpassinger, J. Simonet, K. Sengstock, R. Höppner, P. Hauke, A. Eckardt, M. Lewenstein, and L. Mathey, *Engineering Ising-XY spin-models in a triangular lattice using tunable artificial gauge fields*, Nat. Phys. **9**, 738–743 (2013).
- [362] G. Pelegrí, J. Mompert, V. Ahufinger, and A. J. Daley, *Quantum magnetism with ultracold bosons carrying orbital angular momentum*, Phys. Rev. A **100**, 023615 (2019).
- [363] F. Deuretzbacher, D. Becker, J. Bjerlin, S. M. Reimann, and L. Santos, *Quantum magnetism without lattices in strongly interacting one-dimensional spinor gases*, Phys. Rev. A **90**, 013611 (2014).
- [364] F. Deuretzbacher, D. Becker, J. Bjerlin, S. M. Reimann, and L. Santos, *Spin-chain model for strongly interacting one-dimensional Bose-Fermi mixtures*, Phys. Rev. A **95**, 043630 (2017).
- [365] R. E. Barfknecht, A. Foerster, and N. T. Zinner, *Dynamical realization of magnetic states in a strongly interacting Bose mixture*, Phys. Rev. A **95**, 023612 (2017).
- [366] S. Murmann, F. Deuretzbacher, G. Zürn, J. Bjerlin, S. M. Reimann, L. Santos, T. Lompe, and S. Jochim, *Antiferromagnetic Heisenberg Spin Chain of a Few Cold Atoms in a One-Dimensional Trap*, Phys. Rev. Lett. **115**, 215301 (2015).
- [367] R. Casalbuoni and G. Nardulli, *Inhomogeneous superconductivity in condensed matter and QCD*, Rev. Mod. Phys. **76**, 263–320 (2004).
- [368] P. Fulde and R. A. Ferrell, *Superconductivity in a Strong Spin-Exchange Field*, Phys. Rev. **135**, A550–A563 (1964).
- [369] A. Larkin and Y. N. Ovchinnikov, *Nonuniform state of superconductors*, Soviet Physics-JETP **20**, 762–762 (1965).
- [370] K. Kinjo, M. Manago, S. Kitagawa, Z. Q. Mao, S. Yonezawa, Y. Maeno, and K. Ishida, *Superconducting spin smecticity evidencing the Fulde-Ferrell-Larkin-Ovchinnikov state in Sr_2RuO_4* , Science **376**, 397–400 (2022).

- [371] M. Singh and G. Orso, *Enhanced visibility of the Fulde-Ferrell-Larkin-Ovchinnikov state in one-dimensional Bose-Fermi mixtures near the immiscibility point*, Phys. Rev. Research **2**, 023148 (2020).
- [372] K. Binder, *Theory of first-order phase transitions*, Rep. Prog. Phys. **50**, 783–859 (1987).
- [373] P. B. Blakie and F. Beyer, *Table-top cosmology with Bose-Einstein condensates*, Ann. Phys. (Berl.) **525**, A163–A164 (2013).
- [374] K. L. Ng, B. Opanchuk, M. Thenabadu, M. Reid, and P. D. Drummond, *Fate of the False Vacuum: Finite Temperature, Entropy, and Topological Phase in Quantum Simulations of the Early Universe*, PRX Quantum **2**, 010350 (2021).
- [375] S. Coleman, *Fate of the false vacuum: Semiclassical theory*, Phys. Rev. D **15**, 2929–2936 (1977).
- [376] A. Trenkwalder, G. Spagnolli, G. Semeghini, S. Coop, M. Landini, P. Castilho, L. Pezzè, G. Modugno, M. Inguscio, A. Smerzi, and M. Fattori, *Quantum phase transitions with parity-symmetry breaking and hysteresis*, Nat. Phys. **12**, 826–829 (2016).
- [377] L.-Y. Qiu, H.-Y. Liang, Y.-B. Yang, H.-X. Yang, T. Tian, Y. Xu, and L.-M. Duan, *Observation of generalized Kibble-Zurek mechanism across a first-order quantum phase transition in a spinor condensate*, Sci. Adv. **6**, eaba7292 (2020).
- [378] B. Song, S. Dutta, S. Bhave, J.-C. Yu, E. Carter, N. Cooper, and U. Schneider, *Realizing discontinuous quantum phase transitions in a strongly correlated driven optical lattice*, Nat. Phys. **18**, 259–264 (2022).
- [379] J. N. Fuchs, D. M. Gangardt, T. Keilmann, and G. V. Shlyapnikov, *Spin Waves in a One-Dimensional Spinor Bose Gas*, Phys. Rev. Lett. **95**, 150402 (2005).
- [380] M. B. Zvonarev, V. V. Cheianov, and T. Giamarchi, *Spin Dynamics in a One-Dimensional Ferromagnetic Bose Gas*, Phys. Rev. Lett. **99**, 240404 (2007).
- [381] X.-W. Guan, M. T. Batchelor, and M. Takahashi, *Ferromagnetic behavior in the strongly interacting two-component Bose gas*, Phys. Rev. A **76**, 043617 (2007).
- [382] S. Takayoshi, M. Sato, and S. Furukawa, *Spontaneous population imbalance in two-component Bose and Fermi gases*, Phys. Rev. A **81**, 053606 (2010).
- [383] J.-S. Caux, A. Klauser, and J. van den Brink, *Polarization suppression and non-monotonic local two-body correlations in the two-component Bose gas in one dimension*, Phys. Rev. A **80**, 061605 (2009).
- [384] E. Eisenberg and E. H. Lieb, *Polarization of Interacting Bosons with Spin*, Phys. Rev. Lett. **89**, 220403 (2002).
- [385] A. Kleine, C. Kollath, I. P. McCulloch, T. Giamarchi, and U. Schollwöck, *Spin-charge separation in two-component Bose gases*, Phys. Rev. A **77**, 013607 (2008).

-
- [386] E. Tempfli, S. Zöllner, and P. Schmelcher, *Binding between two-component bosons in one dimension*, New J. Phys. **11**, 073015 (2009).
- [387] Li, Y.-Q., Gu, S.-J., Ying, Z.-J., and Eckern, U., *Exact results of the ground state and excitation properties of a two-component interacting Bose system*, Europhys. Lett. **61**, 368–374 (2003).
- [388] L. Mathey, I. Danshita, and C. W. Clark, *Creating a supersolid in one-dimensional Bose mixtures*, Phys. Rev. A **79**, 011602 (2009).
- [389] M. A. García-March, B. Juliá-Díaz, G. E. Astrakharchik, Th. Busch, J. Boronat, and A. Polls, *Quantum correlations and spatial localization in one-dimensional ultracold bosonic mixtures*, New J. Phys. **16**, 103004 (2014).
- [390] S. Zöllner, H.-D. Meyer, and P. Schmelcher, *Composite fermionization of one-dimensional Bose-Bose mixtures*, Phys. Rev. A **78**, 013629 (2008).
- [391] G. E. Astrakharchik and B. A. Malomed, *Dynamics of one-dimensional quantum droplets*, Phys. Rev. A **98**, 013631 (2018).
- [392] T. Mithun, A. Maluckov, K. Kasamatsu, B. A. Malomed, and A. Khare, *Modulational Instability, Inter-Component Asymmetry, and Formation of Quantum Droplets in One-Dimensional Binary Bose Gases*, Symmetry **12** (2020).
- [393] A. Tononi, Y. Wang, and L. Salasnich, *Quantum solitons in spin-orbit-coupled Bose-Bose mixtures*, Phys. Rev. A **99**, 063618 (2019).
- [394] G. De Rosi, G. E. Astrakharchik, and P. Massignan, *Thermal instability, evaporation, and thermodynamics of one-dimensional liquids in weakly interacting Bose-Bose mixtures*, Phys. Rev. A **103**, 043316 (2021).
- [395] E. Chiquillo, *Equation of state of the one- and three-dimensional Bose-Bose gases*, Phys. Rev. A **97**, 063605 (2018).
- [396] P. G. Kevrekidis, H. E. Nistazakis, D. J. Frantzeskakis, B. A. Malomed, and R. Carretero-González, *Families of matter-waves in two-component Bose-Einstein condensates*, Eur. Phys. J. D **28**, 181–185 (2004).
- [397] A. Sartori and A. Recati, *Dynamics of highly unbalanced Bose-Bose mixtures: miscible vs. immiscible gases*, Eur. Phys. J. D **67**, 260 (2013).
- [398] G. Biagioni, N. Antolini, A. Alaña, M. Modugno, A. Fioretti, C. Gabbanini, L. Tanzi, and G. Modugno, *Dimensional Crossover in the Superfluid-Supersolid Quantum Phase Transition*, Phys. Rev. X **12**, 021019 (2022).
- [399] Z.-K. Lu, Y. Li, D. S. Petrov, and G. V. Shlyapnikov, *Stable Dilute Supersolid of Two-Dimensional Dipolar Bosons*, Phys. Rev. Lett. **115**, 075303 (2015).
- [400] P. Forrester, N. Frankel, T. Garoni, and N. Witte, *Finite one-dimensional impenetrable Bose systems: Occupation numbers*, Phys. Rev. A **67**, 043607 (2003).

-
- [401] T.-N. Xu, J. Li, Th. Busch, X. Chen, and T. Fogarty, *Effects of coherence on quantum speed limits and shortcuts to adiabaticity in many-particle systems*, Phys. Rev. Research **2**, 023125 (2020).
- [402] G. G. Batrouni, R. T. Scalettar, and G. T. Zimanyi, *Quantum critical phenomena in one-dimensional Bose systems*, Phys. Rev. Lett. **65**, 1765–1768 (1990).
- [403] G. G. Batrouni and R. T. Scalettar, *World-line quantum Monte Carlo algorithm for a one-dimensional Bose model*, Phys. Rev. B **46**, 9051–9062 (1992).
- [404] J. Boronat and J. Casulleras, *Monte Carlo analysis of an interatomic potential for He*, Phys. Rev. B **49**, 8920–8930 (1994).
- [405] I. Kosztin, B. Faber, and K. Schulten, *Introduction to the diffusion Monte Carlo method*, Am. J. Phys. **64**, 633–644 (1996).
- [406] U. Schollwöck, *The density-matrix renormalization group*, Rev. Mod. Phys. **77**, 259–315 (2005).
- [407] F. Verstraete and J. I. Cirac, *Continuous Matrix Product States for Quantum Fields*, Phys. Rev. Lett. **104**, 190405 (2010).
- [408] V. Cikojević, K. Dželalija, P. Stipanović, L. Vranješ Markić, and J. Boronat, *Ultradilute quantum liquid drops*, Phys. Rev. B **97**, 140502 (2018).
- [409] L. Parisi, G. E. Astrakharchik, and S. Giorgini, *Liquid State of One-Dimensional Bose Mixtures: A Quantum Monte Carlo Study*, Phys. Rev. Lett. **122**, 105302 (2019).